CERN LHCC 2000-037
LHCb TDR 3
6 September 2000

LHCb

RICH Technical Design Report

Printed at CERN
Geneva, 2000

This Technical Design Report is dedicated to Tom Ypsilantis. Tom conceived the Ring Imaging Cherenkov detectors for particle identification in LHCb and he made an inestimable contribution to the LHCb RICH project.

Tom would have wished to see these detectors in operation. He was totally dedicated to the project. He will be missed by the RICH group for his ideas, his guidance, his animation of group meetings, his criticism, always given kindly and constructively. For many he was a close friend, for all a respected colleague.

The LHCb Collaboration[1]

University of Rio de Janeiro, UFRJ, Rio de Janeiro, Brasil
S.Amato, D.Carvalho, P.Colrain, T.da Silva, J.R.T.de Mello, L.de Paula, M.Gandelman, J.Helder Lopes, B.Marechal, D.Moraes, E.Polycarpo

University of Clermont-Ferrand II, Clermond-Ferrand, France
Z.Ajaltouni, G.Bohner, V.Breton, R.Cornat, O.Deschamps, A.Falvard, J.Lecoq, P.Perret, C.Trouilleau, A.Ziad

CPPM Marseille, Aix University-Marseille II, Marseille, France
E.Aslanides, J.P.Cachemiche, R.Legac, O.Leroy, M.Menouni, R.Potheau, A.Tsaregorodtsev

University of Paris-Sud, LAL Orsay, Orsay, France
G.Barrand, C.Beigbeder-Beau, D.Breton, T.Caceres, O.Callot, Ph.Cros, B.D'Almagne, B.Delcourt, F.Fulda Quenzer, A.Hrisoho, B.Jean-Marie, J.Lefrancois, V.Tocut, K.Truong

Humboldt University, Berlin, Germany
T.Lohse

Technical University of Dresden, Dresden, Germany
R.Schwierz, B.Spaan

University of Freiburg, Freiburg, Germany
H.Fischer, J.Franz, F.H.Heinsius, K.Königsmann, H.Schmitt

Max-Planck-Institute for Nuclear Physics, Heidelberg, Germany
C.Bauer, D.Baumeister, N.Bulian, H.P.Fuchs, T.Glebe, W.Hofmann, K.T.Knöpfle, S.Löchner, M.Schmelling, B.Schwingenheuer, F.Sciacca, E.Sexauer, U.Trunk

Physics Institute, University of Heidelberg, Heidelberg, Germany
S.Bachmann, P.Bock, H.Deppe, H.B.Dries, F.Eisele, M.Feuerstack-Raible, S.Henneberger, P.Igo-Kemenes, Ch.Rummel, R.Rusnyak, U.Stange

Kirchhoff Institute for Physics, University of Heidelberg, Heidelberg, Germany
V.Lindenstruth, R.Richter, M.W.Schultz, A.Walsch

Frascati Laboratori Nazionali, Frascati, Italy
G.Bencivenni, C.Bloise, F.Bossi, P.Campana, G.Capon, P.DeSimone, C.Forti, M.Murtas, L.Passalacqua, V.Patera(1), L.Satta(1), A.Sciubba(1)
(1) Also at Dipartimento di Energetica, University of Rome, "La Sapienza"

University of Bologna and INFN, Bologna, Italy
M.Bargiotti, A.Bertin, M.Bruschi, M.Capponi, I.D'Antone, S.Castro,R.Dona, D.Galli, B.Giacobbe, U.Marconi, I.Massa, M.Piccinini, M.Poli, N.Semprini-Cesari, R.Spighi, V.Vagnoni, S.Vecchi, M.Villa, A.Vitale, A.Zoccoli

---

[1] This list includes additional colleagues who made particular contributions to the work presented in this TDR.

University of Cagliari and INFN, Cagliari, Italy
W.Bonivento, A.Cardini, M.Caria, A.Lai, D.Pinci, B.Saitta

University of Ferrara and INFN, Ferrara, Italy
V.Carassiti, A.Cotta Ramusino, P.Dalpiaz, A.Gianoli, M.Martini, F.Petrucci, M.Savrie

University of Florence and INFN, Florence, Italy
A.Bizzeti, M.Calvetti, E.Iacopini, M.Lenti, F.Martelli, G.Passaleva, M.Veltri

University of Genoa and INFN, Genoa, Italy
S.Cuneo, F.Fontanelli, V.Gracco, P.Musico, A.Petrolini, M.Sannino

University of Milano and INFN, Milano, Italy
M.Alemi, T.Bellunato, M.Calvi, C.Matteuzzi, P.Negri, M.Paganoni, V.Verzi

University of Rome, "La Sapienza" and INFN, Rome, Italy
G.Auriemma, V.Bocci, C.Bosio, G.Chiodi, D.Fidanza, A.Frenkel, K.Harrison, S.Mari, G.Martellotti, S.Martinez, G.Penso, R.Santacesaria, C.Satriano, A.Satta

University of Rome, "Tor Vergata" and INFN, Rome, Italy
G.Carboni, D.Domenici, R.Messi, L.Pacciani, L.Paoluzi, E.Santovetti

NIKHEF, The Netherlands
T.S.Bauer(4), M.Doets(1,2), Y.Gouz(1,5), V.Gromov(1), R.Hierck(1), L.Hommels(1), E.Jans(1), T.Ketel(2), S.Klous (2), B.Koene(1), M.Merk(1), M.Needham(1), H.Schuijlenburg(1), T.Sluijk(1), L.Wiggers(1), G.van Apeldoorn(3), N.van Bakel(1,2), J.van den Brand(1), R.van der Eijk(1), N.Zaitsev(3,6)
(1) Foundation of Fundamental Research of Matter in the Netherlands,
(2) Free University Amsterdam,
(3) University of Amsterdam,
(4) University of Utrecht,
(5) On leave from Protvino,
(6) On leave from Petersburg

Institute of High Energy Physics, Beijing, P.R.C.
C.Gao, C.Jiang, H.Sun, Z.Zhu

Research Centre of High Energy Physics, Tsinghua University, Beijing, P.R.C.
M.Bisset, J.P.Cheng, Y.G.Cui, Y.Gao, H.J.He, Y.P.Kuang, Y.J.Li, Y.Liao, Q.Lin, J.P.Ni, B.B.Shao, J.J.Su, Y.R.Tian, Q.Wang, Q.S.Yan

Institute for Nuclear Physics and University of Mining and Metalurgy, Krakow, Poland
E.Banas, J.Blocki, K.Galuszka, P.Jalocha, P.Kapusta, B.Kisielewski, W.Kucewicz, T.Lesiak, J.Michalowski, B.Muryn, Z.Natkaniec, W.Ostrowicz, G.Polok, E.Rulikowska-Zarebska, M.Stodulski, M.Witek, P.Zychowski

Soltan Institute for Nuclear Physics, Warsaw, Poland

M.Adamus, A.Chlopik, Z.Guzik, A.Nawrot, M.Szczekowski

Horia Hulubei-National Institute for Physics and Nuclear Engineering (IFIN-HH), Bucharest-Magurele, Romania
D.V.Anghel, C.Coca, D.Dumitru, G.Giolu, C.Magureanu, R.Petrescu, S.Popescu, T.Preda, A.M.Rosca, V.L.Rusu

Institute for Nuclear Research (INR), Moscow, Russia
V.Bolotov, S.Filippov, J.Gavrilov, E.Guschin, V.Kloubov, L.Kravchuk, S.Laptev, V.Laptev, V.Postoev, A.Sadovski, I.Semeniouk

Institute of Theoretical and Experimental Physics (ITEP), Moscow, Russia
S.Barsuk, I.Belyaev, A.Golutvin, O.Gouchtchine, V.Kiritchenko, G.Kostina, N.Levitski, A.Morozov, P.Pakhlov, D.Roussinov, V.Rusinov, S.Semenov, A.Soldatov, E.Tarkovski

P.N.Lebedev Physical Institute, Moscow, Russia
Yu.Alexandrov, V.Baskov, L.Gorbov, B.Govorkov, V.Kim, P.Netchaeva, V.Polianski, L.Shtarkov, A.Verdi, M.Zavertiaev

Institute for High Energy Physics (IHEP-Serpukhov),Protvino, Russia
I.V.Ajinenko, K.Beloous, V.Brekhovskikh, S.Denissov, R.I.Dzhelyadin, A.V.Dorokhov, A.Kobelev, A.K.Konoplyannikov, A.K.Likhoded, V.D.Matveev, V.Novikov, V.F.Obraztsov, A.P.Ostankov, V.I.Rykalin, V.K.Semenov, M.M.Shapkin, N.Smirnov, M.M.Soldatov, A.Sokolov, V.V.Talanov, O.P.Yushchenko

Petersburg Nuclear Physics Institute, Gatchina, St.Petersburg, Russia
B.Botchine, S.Guetz, A.Kashchuk, V.Lazarev, N.Saguidova, V.Souvorov, E.Spiridenkov, A.Vorobyov, An.Vorobyov

University of Barcelona, Barcelona, Spain
S.Botta Ferragut, L.Garrido Beltran, D.Gascon, R.Miquel, D.Peralta-Rodriguez, M.Rosello Canal(1), X.Vilasis Cardona(1)
(1) Departament d'Engineria Electronica La Salle, Universitat Ramon Llull, Barcelona

University of Santiago de Compostela, Santiago de Compostela, Spain
B.Adeva, P.Conde, F.Gomez, J.A.Hernando, A.Iglesias, A.Lopez-Aguera, A.Pazos, M.Plo, J.M.Rodriguez, J.J.Saborido, M.J.Tobar

University of Lausanne, Lausanne, Switzerland
P.Bartalini, A.Bay, C.Currat, O.Dormond, F.Dürrenmatt, Y.Ermoline, R.Frei, G.Gagliardi, J.P.Hertig, G.Haefeli, P.Koppenburg, J.P.Perroud, F.Ronga, O.Schneider, L.Studer, M.Tareb, M.T.Tran

University of Zürich , Zürich, Switzerland
R.Bernet, E.Holzschuh, P.Sievers, O.Steinkamp, U.Straumann, D.Wyler, M.Ziegler

Institute of Physics and Techniques, Kharkov, Ukraine
S.Maznichenko, O.Omelaenko, Yu.Ranyuk, M.V.Sosipatorow

Institute for Nuclear Research, Kiev, Ukraine
V.Aushev, V.Kiva, I.Kolomiets, Yu.Pavlenko, V.Pugatch, Yu.Vasiliev, V.Zerkin

University of Bristol, Bristol, U.K.
N.Brook, R.Head, F.Wilson

University of Cambridge, Cambridge, U.K.
V.Gibson, S.G.Katvars, C.R.Jones, C.Shepherd-Themistocleous, C.P.Ward, D.R.Ward, S.A.Wotton

Rutherford Appleton Laboratory, Chilton, U.K.
C.A.J.Brew, C.J.Densham, S.Easo, B.Franek, M.J.French, J.G.V.Guy, R.N.J.Halsall, J.A.Lidbury, J.V.Morris, A.Papanestis, G.N.Patrick, F.J.P.Soler, S.A.Temple

University of Edinburgh, Edinburgh, U.K.
S.Eisenhardt, A.Khan, F.Muheim, S.Playfer, A.Walker

University of Glasgow, Glasgow, U.K.
A.J.Flavell, A.Halley, V.O'Shea, F.J.P.Soler

University of Liverpool, Liverpool, U.K.
S.Biagi, T.Bowcock, R.Gamet, P.Hayman, M.McCubbin, C.Parkes, G.Patel, S.Walsh, V.Wright

Imperial College, London, U.K.
G.J.Barber, D.Clark, I.Clark, P.Dauncey, A.Duane, S.Greenwood, J.Hassard, R.Hill, M.J.John, D.R.Price, P.Savage, B.Simmons, L.Toudup, D.Websdale

University of Oxford, Oxford, U.K
M.Adinolfi, J.Bibby, M.J.Charles, N.Harnew, F.Harris, I.McArthur, J.Rademacker, N.J.Smale, S.Topp-Jorgensen, G.Wilkinson

CERN, Geneva, Switzerland
E.Albrecht, F.Anghinolfi, A.Augustinus, P.Binko, A.Braem, B.Bruder, J.Buytaert, M.Campbell, A.Cass, M.Cattaneo, P.Charpentier, P.Charra, E.Chesi, J.Christiansen, R.Chytracek, J.Closier, G.Corti, C.D'Ambrosio, C.David, H.Dijkstra, D.Dominguez, J.P.Dufey, L.Eklund, M.Ferro-Luzzi, F.Fiedler, W.Flegel, F.Formenti, R.Forty, M.Frank, I.Garcia Alfonso, C.Gaspar, G.Gracia Abril, T.Gys, F.Hahn, S.Haider, J.Harvey, B.Hay, H.J.Hilke, A.Jacholkowska(1), R.Jacobsson, P.Jarron, C.Joram, B.Jost, A.Kashchuk,(2), I.Korolko(3), D.Lacarrère, M.Laub, M.Letheren, J.F.Libby, D.Liko(4), R.Lindner, M.Losasso, P.Mato Vila, H.Müller, T.Nakada(5), N.Neufeld(4), J.Ocariz, D.Piedigrossi, S.Probst, F.Ranjard, W.Riegler, F.Rohner, T.Ruf, B.Schmidt, T.Schneider, A.Schöning, A.Schopper, J.Seguinot(6), W.Snoeys, W.Tejessy, F.Teubert, O.Ullaland, A.Valassi, E.van Herwijnen, P.Vazquez Regueiro, I.Videau(1), F.Vinci do Santos, G.von Holtey, P.Wicht, A.Wright, K.Wyllie, P.Wertelaers, T.Ypsilantis(7), M.Zuin
(1) on leave from LAL, Orsay
(2) on leave from PNPI, Gatchina
(3) on leave from ITEP, Moscow
(4) on leave from the Institute of High Energy Physics, Vienna

(5) also at University of Lausanne
(6) emeritus, College de France
(7) visitor from University of Bologna, deceased

Acknowledgments

The LHCb RICH group is greatly indebted to many people, at CERN and in the home institutes, who have participated at various stages to the design, testing and prototype activities presented in this report. In particular we acknowledge the contribution of L.Gatignon.

We would like to thank A.Mazzari, V.Brunner, M.Grygiel and in particular N.Grüb for their enthusiastic help in the preparation of this proposal and the related LHCb Notes.

Contents

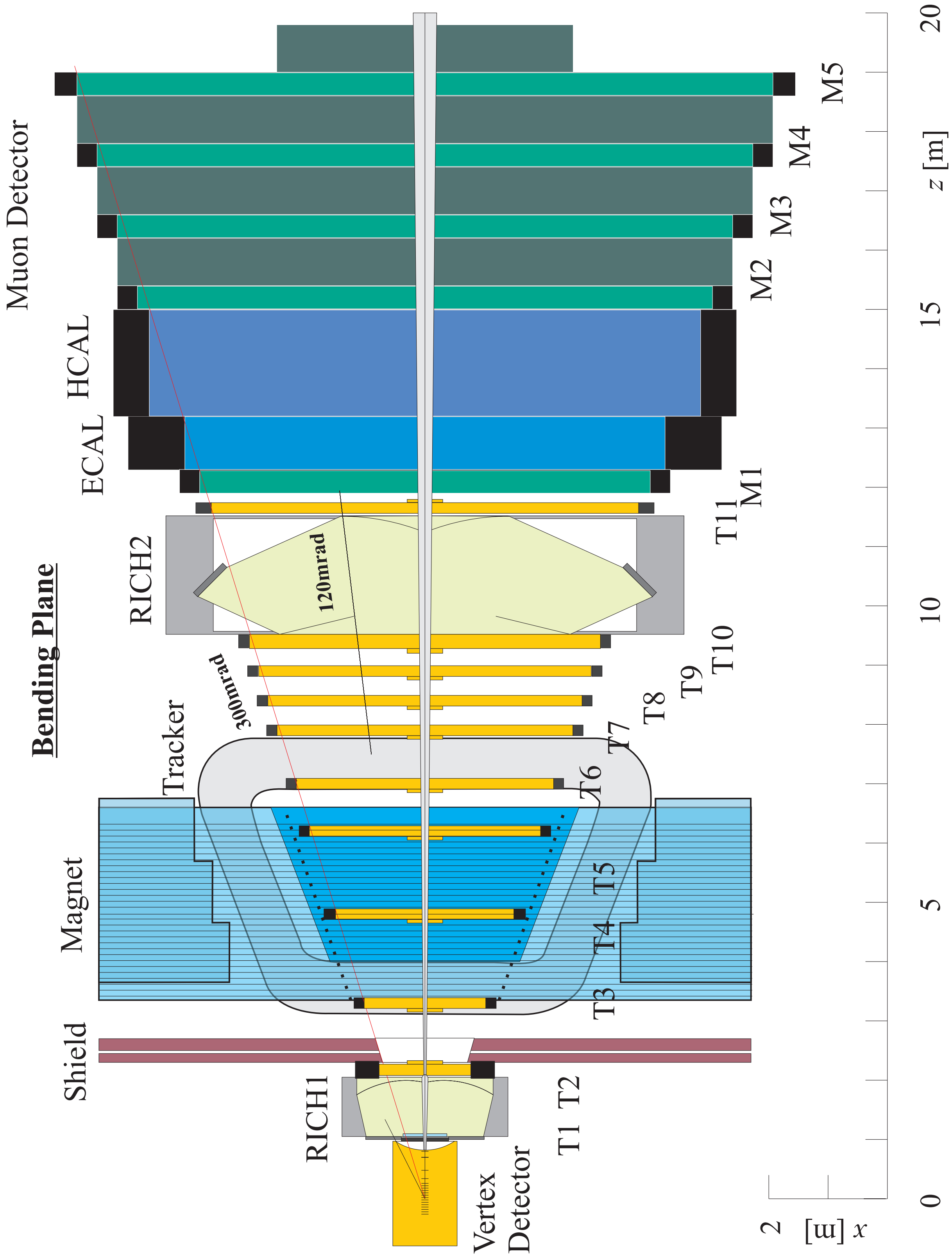

Figure 1: The LHCb spectrometer seen from above (cut in the bending plane), showing the location of the RICH detectors.

1 Introduction

Particle identification is a fundamental requirement of the LHCb experiment. The ability to distinguish between pions and kaons in a variety of final states is essential for the physics that the experiment is designed to study: meaningful CP-violation measurements are only possible in many important channels if hadron identification is available.

The particle identification is achieved using ring-imaging Cherenkov (RICH) detectors. Their placement within the LHCb spectrometer can be seen in Fig. 1, which shows the top view of the experiment. Details of the rest of the experiment can be found in [1, 2, 3].

In this introduction, the physics requirements are discussed, and an overview is given of the RICH detector system. A brief discussion of the evolution since the Technical Proposal is then given, before an outline of the rest of the document.

1.1 Physics requirements

An example of the importance of the RICH system is the measurement of the CP asymmetry of $\mathrm{B_d^0} \to \pi^+\pi^-$ decays. This requires the rejection of two-body backgrounds with the same topology: $\mathrm{B_d^0} \to \mathrm{K}^+\pi^-$, $\mathrm{B_s^0} \to \mathrm{K}^-\pi^+$ and $\mathrm{B_s^0} \to \mathrm{K^+K^-}$. This can be seen in Fig. 2, where the invariant-mass spectrum is shown for the expected mixture of B decays. Before particle identification is applied, the signal from $\mathrm{B_d^0} \to \pi^+\pi^-$ is dwarfed by the backgrounds.

Another benchmark channel of LHCb is $\mathrm{B_s^0} \to \mathrm{D_s^\mp K^\pm}$ and the charge conjugate states, which is used to extract the CP-angle γ from a time-dependent fit to the asymmetries. Here the background from $\mathrm{B_s^0} \to \mathrm{D_s^-}\pi^+$ decays is ~ 15 times more abundant, as can be seen in Fig. 3. This would overwhelm the signal if particle identification was not available.

Another method to access the angle γ is through channels such as $\mathrm{B^0} \to \mathrm{D^0K^{*0}} \to \mathrm{K}^-\pi^+\mathrm{K}^+\pi^-$ and $\mathrm{B^0} \to \overline{\mathrm{D}}{}^0\mathrm{K^{*0}} \to \pi^-\mathrm{K^+K^+}\pi^-$. Positive identification of particles is essential

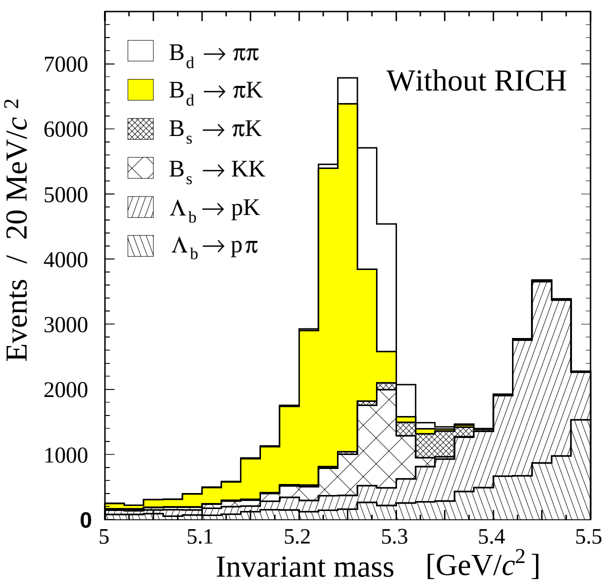

Figure 2: Mass spectrum of $\mathrm{B_d^0} \to \pi^+\pi^-$ candidates before any particle identification is applied.

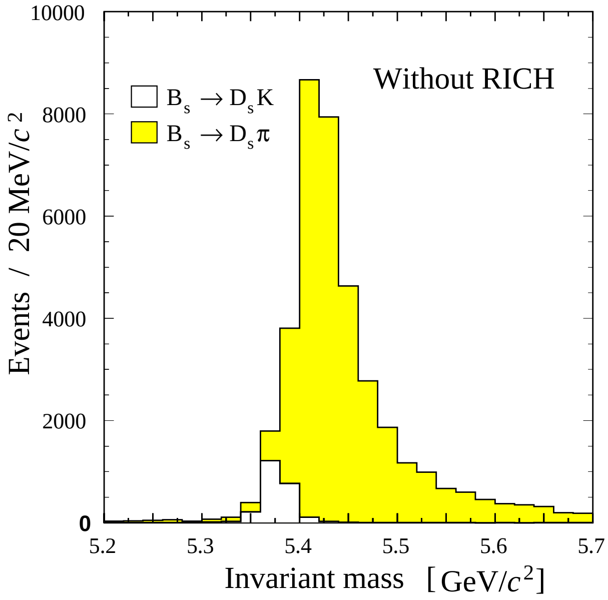

Figure 3: Mass spectrum of $\mathrm{B_s^0} \to \mathrm{D_sK}$ candidates before any particle identification is applied.

for the selection of such rare decays.

Identifying kaons from the accompanying b hadron decay in the event also provides a valuable flavour tag, and ensures that all events accepted by the LHCb trigger are potentially useful in the CP violation measurements. The flavour tag is achieved by identifying kaons from the b → c → s cascade decay, where the charge of the kaon depends on the charge of the initial b quark.

Finally, the particle-identification system can complement the calorimeters and muon system in the identification of electrons and muons. For high mass particles it can provide an improved momentum determination.

The particle identification should cover the full angular acceptance of the LHCb spectrometer, from 10 mrad to 300 mrad in the horizontal (x, z) projection and to 250 mrad in the vertical (y, z) projection. The upper limit in momentum required for π–K separation is determined by tracks from two-body B-decay channels, as shown in Fig. 4 (a); 90% have $p < 150\,\mathrm{GeV}/c$. The identification of tagging kaons and tracks from high multiplicity decays determines the requirement for the lower momentum limit. As shown in Fig. 4 (b), identification down to $1\,\mathrm{GeV}/c$ is desirable.

1.2 RICH system overview

The only feasible technique that can cover the required momentum range is the detection of ring images of Cherenkov light produced by the passage of charged particles through various radiators. To cover the full range, three radiators are required, with different refractive indices. Silica aerogel, with $n = 1.03$, is suitable for the lowest momentum tracks, whilst the intermediate region is well matched to gaseous C_4F_{10}. For the highest momentum tracks, gaseous CF_4 is used.

There is a strong correlation between the polar angle and momentum of tracks, as seen in Fig. 5: at wide angles, the momentum spectrum is softer. The RICH system is therefore divided into two detectors. An upstream detector (RICH 1) contains both the aerogel and C_4F_{10} radiators, covering the full outer acceptance of LHCb. To minimize the required photodetector area it is sited close to the interaction region, and upstream of the spectrometer dipole to catch particles that will be swept out of the acceptance by the magnet. A downstream detector (RICH 2) has a CF_4 radiator, to analyse the high-momentum

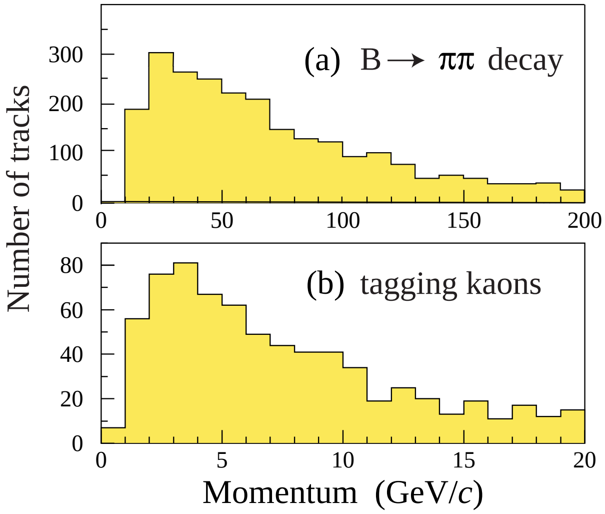

Figure 4: Momentum distributions for (a) the highest momentum pion from $B_d^0 \to \pi^+\pi^-$ decays, (b) tagging kaons.

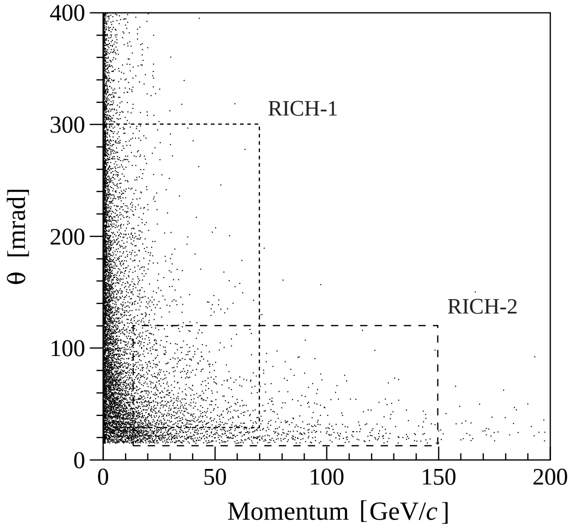

Figure 5: Polar angle θ versus momentum, for all tracks in simulated $B_d^0 \to \pi^+\pi^-$ events. The regions of interest for RICH 1 and RICH 2 are indicated by the dashed lines.

tracks which will traverse the magnet. Its coverage is limited to the region 120 mrad (horizontal)×100 mrad (vertical), where high momentum tracks are abundant. The inner acceptances are determined by the size of the beam-pipe, and correspond to 25 mrad at RICH 1 and 15 mrad at RICH 2.

Both detectors are located in low magnetic field regions so that the tracks do not curve appreciably whilst passing through the radiators (which would limit the resolution). Low magnetic field is also important for the operation of the photodetectors, which are hybrid photodiodes (HPD's) with pixel readout. A total image surface of about $2.6\,\mathrm{m}^2$ is required, with an effective detector granularity of about 2.5 mm × 2.5 mm.

1.3 Evolution since the Technical Proposal

A major effort since the LHCb Technical Proposal [1] has gone into the development of the RICH photodetector system, which must provide a large fraction of active area at an acceptable cost. The key development has been the choice of technology for these photodetectors. An internal LHCb review panel supplemented by external experts prepared the photodetector choice, and considered three options: the Pad HPD [4], the Pixel HPD [5], and the M64 Multianode Photomultiplier (MAPMT) [6].

The final choice between the three options was based on performance studies from a full simulation and pattern recognition of the proposed photodetectors, a consideration of the readout electronics for the three options, the mounting and requirements for integration into the RICH detectors, and finally on cost, risk and resource considerations. Performance indicators, including photon yields, Cherenkov angle precision, π–K separation, particle ID matrices (efficiencies and purities), backgrounds in two-body decay channels and kaon tagging, were compared for the three options. As a result of these extensive studies the Pixel HPD has been selected by the LHCb collaboration as the baseline photodetector. Milestones with rigorous performance criteria have been set for the Pixel HPD on the time-scale of one year. The details of the technical criteria and the schedule are discussed in Sections 5.1 and 6 respectively.

There is a parallel and well-focused activity to ensure that the MAPMT remains a viable back-up option to the Pixel HPD, consistent with the LHCb schedule. Extensive beam tests of a prototype RICH detector with a 3×3 MAPMT array have been made, and it has been demonstrated that the MAPMT option meets all the necessary performance criteria if the Pixel HPD fails to meet its milestones, although with an increased cost.

There have been other major areas of development in the RICH project since the Technical Proposal. The geometries and mechanical implementations of RICH 1 and RICH 2 have evolved, in particular the beam pipe sealing, and photodetector and mirror mounting. There has been considerable advancement in the RICH software: a full GEANT simulation has been performed, which includes realistic pattern recognition and reconstruction of tracks in the LHCb tracking chambers. In turn, this has resulted in more realistic RICH reconstruction, and hence better performance indicators of the RICH system. Future evolution of the software will take place within a C^{++} framework that has been established. Finally, as a result of the choice of Pixel HPD as photodetector, the electronics readout has evolved into a binary system both on- and off-detector.

1.4 Structure of this document

This Technical Design Report is intended to be a concise but self-contained description of the RICH system, comprising both the RICH 1 and RICH 2 detectors. Further details can be found in the many Technical Notes, which are referenced throughout.

In the following section, the detector specifications are given. This is followed by a description of the physics performance of the system, determined using simulated events. In

Section 4 an overview is given of the results obtained in the laboratory and test-beam using prototypes, which give confidence that the expected performance will be achieved. The technical design of the detectors is presented in Section 5. The issues of project organisation, including the schedule and cost, are discussed in Section 6, and finally details are given for the back-up photodetector in Appendix A.

2 Detector Specifications

The basic requirement of the LHCb RICH system is to provide particle identification over a wide momentum range, from 1–150 GeV/c.

In this section the principal features of the detectors are described and their main parameters are listed. Their optimization has been constrained by limits on the space available, on material in the spectrometer acceptance and on the overall cost, to which the photon detectors contribute about 50%.

Prototype tests have been undertaken which demonstrate that the parameters listed can be achieved. These are described in Section 4. The parameters have been used in simulation studies to evaluate the physics performance of the RICH system. The results from these studies are reported in Section 3.

2.1 Overall dimensions

The overall length of the LHCb detector is constrained by the space available in the cavern between the interaction point and the elements of the LHC machine.

RICH 1 is required to cover the full LHCb angular acceptance, so to reduce its physical size it is placed upstream of the spectrometer magnet. The longitudinal space available limits the length of RICH 1 to about 1 m, starting downstream of the vertex detector. The focusing of the Cherenkov light is accomplished using spherical mirrors. They are tilted, to bring the image out of the spectrometer acceptance, so that the material of the photodetectors does not degrade the tracking. The angular acceptance of 300 mrad (horizontal)×250 mrad (vertical), and the tilted optics, result in a RICH 1 vessel with dimensions approximately $2.4\times2.4\times1\,\mathrm{m}^3$. RICH 1 is shown schematically in Fig. 6. It has a 5 cm-thick aerogel radiator and a 85 cm-long C_4F_{10} gas radiator.

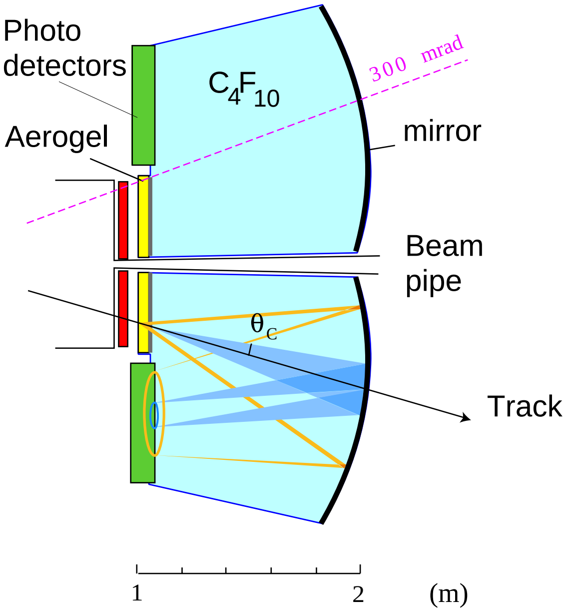

Figure 6: Schematic layout of the RICH 1 detector (seen from above). The focusing of Cherenkov light from a track passing through the detector is illustrated.

RICH 2 has a reduced angular acceptance of 120 mrad (horizontal) ×100 mrad (vertical), but is required to separate pions from kaons at energies above 100 GeV. This requires a gas of lower refactive index, resulting in a reduced yield of Cherenkov photons for a given radiator length. An overall length of about 2 m is allocated, immediately upstream of the final tracking station T11. The requirement that the photon detectors are situated outside of the full LHCb acceptance then defines the lateral dimensions of RICH 2, resulting in a vessel with dimensions approximately $7\times7\times2\,\mathrm{m}^3$. RICH 2 is shown schematically in Fig. 7. The CF_4 radiator has an approximate length of 170 cm. To shorten the overall length of the detector, the reflected image from the tilted spherical mirror is reflected again by a flat secondary mirror onto the detector planes.

2.2 Cherenkov angle precision

The resolution on the reconstructed Cherenkov angle has the following contributions:

1. *Emission point:* the tilting of the focusing mirror leads to a dependence of the image of a Cherenkov photon on its emission point on the track. In the reconstruction, all photons are treated as if

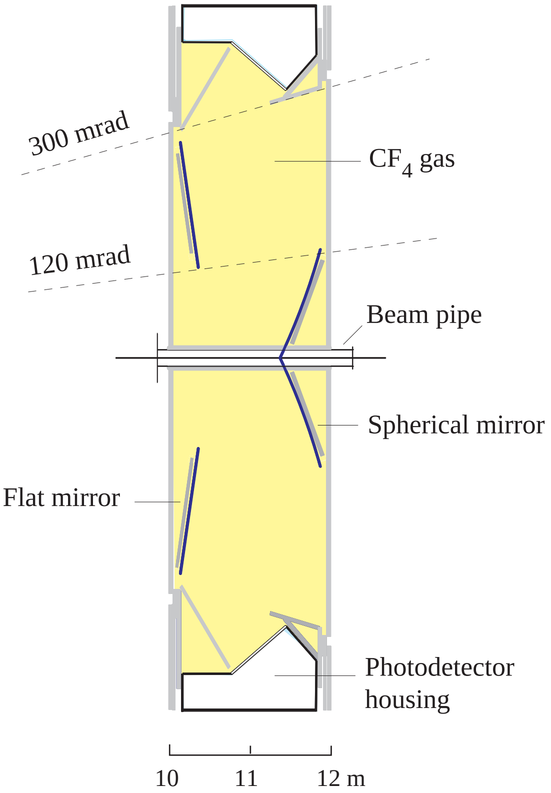

Figure 7: Schematic layout of the RICH 2 detector (seen from above).

emitted at the mid-point of the track through the radiator, leading to some smearing of the reconstructed angle.

2. *Chromatic:* the chromatic dispersion of the radiators leads to a dependence of the Cherenkov angle on the photon energy.
3. *Pixel:* due to the finite granularity of the detector.
4. *Tracking*: due to errors in the reconstructed track parameters.

These contributions are listed in Table 1 for each of the RICH radiators. The granularity of the photon detectors has been chosen as 2.5 mm×2.5 mm based on a comparison of the pixel contribution with the other terms. Reducing the pixel size would incur increased cost with little benefit to Cherenkov angle precision.

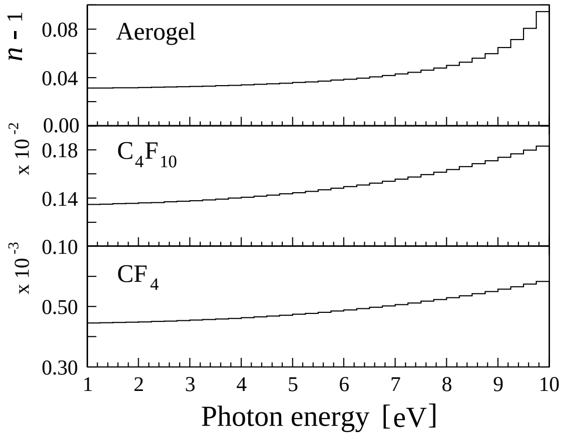

Figure 8: Refractive index of the radiator media as a function of the photon energy.

Table 1: Some characteristics of the radiator materials used in the RICH system as determined from the simulation (for visible light at STP); the lower part lists the contributions to the resolution (from emission-point, chromatic, pixel and tracking), the total resolution per photoelectron and the mean number of detected photoelectrons in the ring image.

Material		CF_4	C_4F_{10}	Aerogel
L	[cm]	167	85	5
n		1.0005	1.0014	1.03
θ_c^{max}	[mrad]	32	53	242
$p_{\mathrm{thresh}}(\pi)$	[GeV]	4.4	2.6	0.6
$p_{\mathrm{thresh}}(\mathrm{K})$	[GeV]	15.6	9.3	2.0
$\sigma_\theta^{\mathrm{emission}}$	[mrad]	0.31	0.74	0.60
$\sigma_\theta^{\mathrm{chromatic}}$	[mrad]	0.42	0.81	1.61
$\sigma_\theta^{\mathrm{pixel}}$	[mrad]	0.18	0.83	0.78
$\sigma_\theta^{\mathrm{track}}$	[mrad]	0.20	0.42	0.26
$\sigma_\theta^{\mathrm{total}}$	[mrad]	0.58	1.45	2.00
N_{pe}		18.4	32.7	6.6

2.3 Radiators

There are two radiators in RICH 1. A 5 cm-thick aerogel radiator with refractive index $n = 1.03$ provides positive kaon identification above $2\,\mathrm{GeV}/c$ and π−K separation up to about $10\,\mathrm{GeV}/c$. The useful wavelength range of the Cherenkov light from aerogel is limited by Rayleigh scattering. The transmission through a length L is proportional to e^{-CL/λ^4}, for wavelength λ, where C is the clarity coefficient. The value assumed in simulations

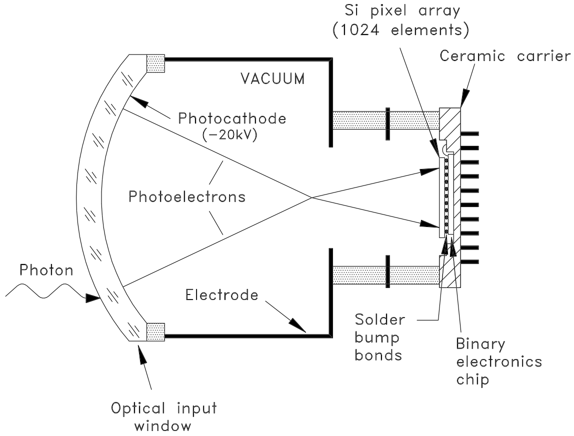

Figure 9: Schematic of the Pixel HPD, illustrating photoelectron trajectories.

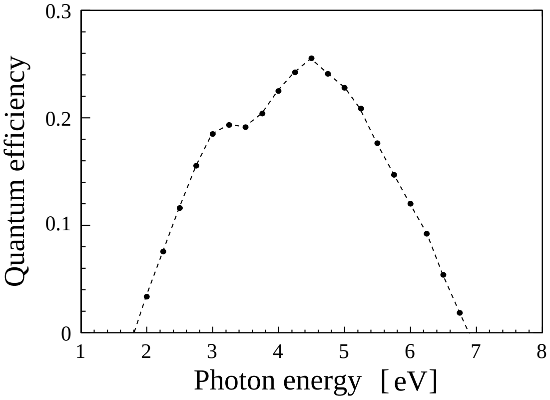

Figure 10: Quantum efficiency as a function of incident photon energy assumed for the photodetectors in the simulation, taken from measurements of HPD prototypes with a quartz window.

and performance studies is $C = 0.008\,\mu\text{m}^4/\text{cm}$, however an R&D effort is currently underway to reduce this to $C = 0.004\,\mu\text{m}^4/\text{cm}$, which would result in a higher fraction of unscattered Cherenkov photons. Alternatively, an increased aerogel radiator length could be used, with correspondingly higher photon yield. The second radiator in RICH 1 is C_4F_{10} gas at STP, which occupies an $L = 85\,\text{cm}$ path length between the aerogel and the spherical mirror. The refractive index is $n = 1.0014$ and it provides $\pi-\text{K}$ separation up to about $50\,\text{GeV}/c$.

RICH 2 contains CF_4 gas at STP, providing an $L = 167\,\text{cm}$ path length with refractive index $n = 1.0005$. Within the angular acceptance from 15 mrad to 120(100) mrad horizontally(vertically) $\pi-\text{K}$ separation is extended beyond $100\,\text{GeV}/c$.

The principal characteristics, including saturated ($\beta = 1$) Cherenkov angles and threshold momenta for pions and kaons are listed in Table 1, for each of the three radiators. The variation of refractive index as a function of the Cherenkov photon energy, which is the source of chromatic aberration in the Cherenkov system, is illustrated in Fig. 8.

2.4 Photon Detectors

The photodetectors are cylindrical pixellated HPD tubes with an overall diameter of 83 mm. They cover a total area of $2.6\,\text{m}^2$, 168 HPDs are used in RICH 1 and 262 in RICH 2. A schematic drawing of the HPD is shown in Fig. 9 and technical details are given in Section 5.1. Each HPD has 1024 pixels of size $0.5\,\text{mm}\times 0.5\,\text{mm}$ on the silicon diode sensor which, for an electrostatic image demagnification factor of five, corresponds to $2.5\,\text{mm}\times 2.5\,\text{mm}$ on the HPD photocathode. The nominal operating voltage is $-20\,\text{kV}$ at the photocathode. Two intermediate electrodes define the focusing properties and the demagnification factor, and the silicon sensor anode is at ground potential. Each tube is surrounded by a magnetic shield in the form of a Mu-metal cylinder of 140 mm length and 86 mm outer diameter, that extends 20 mm beyond the centre of the entrance window.

The HPD has a 7 mm thick, spherical quartz entrance window with an S20 (multialkali) photocathode deposited on its inner surface. The quantum efficiency as a function of the incident photon energy is shown in Fig. 10. The corresponding energy-integrated response is given by $q_{\text{int}} = 0.77\,\text{eV}$. The HPD is photosensitive over a 75 mm diameter, hence for hexagonal close packing (0.907 coverage) of HPD cylinders with 87 mm between centres the effective active area of the HPDs is a fraction

$\varepsilon_{\rm A} = 0.907 \times (75/87)^2 = 0.67$.

The expected number of detected photoelectrons from a saturated track passing through a Cherenkov radiator of length L is given by [7]:

$$N_{\rm pe} = \left(\frac{\alpha}{\hbar c}\right) L\, \varepsilon_A\, \eta \int Q \mathcal{R} \mathcal{T} \sin^2 \theta_{\rm c}\, dE_\gamma\ , \quad (1)$$

where the first factor is a constant with value 370 $\rm eV^{-1}cm^{-1}$, ε_A is the coverage of the photodetector active area and $\eta = 0.9$ is the HPD single photoelectron detection efficiency following conversion by the photocathode. The energy dependent terms in the integral are the HPD quantum efficiency Q, shown in Fig. 10, the mirror reflectivity $\mathcal{R}$ (0.9 in RICH 1, $(0.9)^2$ in RICH 2) and the transmission $\mathcal{T} = 0.92$ of a 5 mm thick quartz plate which seals the Cherenkov gas volume in front of the HPDs. The numbers of photoelectrons expected for each of the RICH radiators are listed in Table 1.

2.5 Readout electronics

The readout electronics chain must conform to the overall LHCb readout specifications [8]. Data from the RICH system are not used in the Level-0 nor Level-1 triggers.

A 1024 channel, $0.25\,\mu$m deep sub-micron, radiation tolerant, CMOS front end chip [9] is encapsulated inside each HPD. This chip accepts input data at 40 MHz and provides Level-0 discriminated (binary) signals with $4\,\mu$s latency from each hit pixel, in 32 parallel channels read out at 1 MHz into the on-detector Level-0 adapter module. Each Level-0 adapter module services two HPDs. It accepts data at 1 MHz and provides a second level of multiplexing (×16) so that the data can be read out through 880 optical links (4 per Level-0 module) into the off-detector Level-1 electronics situated at 100 m distance. The Level-1 electronics removes events rejected by the Level-1 trigger and derandomizes the data for transport to the DAQ and event building network.

2.6 Mirrors

The focusing of the Cherenkov light is accomplished using spherical mirrors in both detectors. They are tilted, to bring the image out of the spectrometer acceptance, so that the material of the photodetectors does not degrade the tracking. RICH 2 has a secondary flat mirror which reflects the image from the spherical mirror onto the photodetector plane.

The spherical mirrors of RICH 1 have a curvature radius of 1700 mm hence a focal length $f = 850$ mm. The total mirror surface is segmented into four quadrants each $900 \times 750\,\rm mm^2$ in area. Each of the quadrants is composed of 2×2 rectangular mirror segments of $450 \times 375\,\rm mm^2$. The axes of the mirror quadrants are tilted with respect to the beam axis by $\sim$ 286 mrad horizontally and $\sim$ 65 mrad vertically. The mirrors are made of polished 6 mm-thick glass coated by vacuum deposition with 900 nm of aluminium and overcoated with 200 nm of quartz. Each mirror can be individually adjusted to a common centre of curvature space point.

The RICH 2 system has two sets of mirrors, the primary spherical mirrors with a curvature radius of 8000 mm ($f = 4000$ mm) followed by a secondary array of flat mirrors. The spherical mirror array is made of 56 hexagonal mirror segments inscribed in a circle of 502 mm diameter whereas the 40 flat mirrors are squares of $437 \times 437\,\rm mm^2$. RICH 2 mirrors are made of the same glass, thickness and surface treatment as those of RICH 1. The hexagonal mirror segments are arranged into two arrays, each with a common centre of curvature and having axes tilted by ±450 mrad horizontally with respect to the beam axis. The flat mirror planes are tilted by 140 mrad with respect to the horizontal. The mounting of the hexagonal mirror segments allows adjustment to obtain a common mirror centre of curvature whereas the flat mirror may be adjusted to centre the image on the HPD detector plane.

The mean mirror reflectivity over the wavelength range of interest ($195\,\rm nm < \lambda < 700\,\rm nm$) is expected to be 0.9.

2.7 Alignment

The angular resolution of the RICH system depends critically on the alignment of its optical components. The precision in reconstruction of the Cherenkov photon angle is about 1 mrad in RICH 1 and about 0.5 mrad in RICH 2. To ensure these figures are not degraded by uncertainties in alignment the aim is to maintain alignment errors below 0.1 mrad. The alignment of the optical components will be achieved in stages. Firstly an accurate *in-situ* survey of all mirror and photodetector components will be performed to a level of < 0.5 mrad in RICH 1 and ~ 0.1 mrad in RICH 2. A laser system will be used to monitor the alignment parameters over time. Final parameters and precision will be extracted using reconstruction of large numbers of rings from $\beta = 1$ tracks in which the ring image is formed via reflection from an unambiguous combination of mirror segments.

2.8 Material budget

The material which is placed within the LHCb acceptance, due to the different components of the RICH system, is listed in Table 2. The total amounts to about 14% and 12% of a radiation length for RICH 1 and RICH 2 respectively.

2.9 Beam pipe access

A common requirement for all LHCb subdetectors is that provision has to be made for access to the LHC beam pipe, for maintenance procedures, and in particular for bake-out. Most LHCb detectors will be constructed in two halves, so that one side can be withdrawn, allowing access to the beam pipe. This solution is undesirable for the RICH detectors, as it would result in significant amounts of material to achieve the vessel seal close to the beam. Furthermore, in the case of RICH 1, tracks traversing the radiator on the right-hand side of the detector emit Cherenkov light which travels through and is detected at the left-hand side. This would result in significant light loss in the vertical window which is needed to separate a split RICH 1.

The access requirement is satisfied for RICH 2 by sealing the vessel with a cylindrical tube, coaxial with and separated by a radial distance of 3 cm from the LHC beam pipe. For RICH 1, this solution would result in unacceptable loss of angular acceptance. The seal of the RICH 1 gas vessel is therefore made direct to the beam pipe in such a way that any stresses are reduced to an acceptable level. Access to the beam pipe for bake-out will be via the RICH 1 vessel, from which the gas, mirrors and the seals would be removed.

Table 2: Contributions (expressed in fractions of a radiation length) to the material in RICH 1 and RICH 2, which fall within the LHCb acceptance.

Item	RICH 1	RICH 2
Entrance window	0.001	0.014
Aerogel	0.033	
Gas radiator	0.024	0.017
Mirror	0.046	0.046
Mirror support	0.030	0.033
Exit window	0.006	0.014
Total (X_0)	0.140	0.124

3 Physics Performance

The performance of the RICH system has been studied using simulated data. In this section the inputs to the simulation are described, and details are given concerning the reconstruction and pattern-recognition algorithms. The RICH performance is characterized, and the particle identification results are shown in various physics channels of interest. Further details can be found in [10].

3.1 Description of simulation

Proton-proton interactions at $\sqrt{s} = 14\,\mathrm{TeV}$ are simulated using the PYTHIA event generator, version 6.1 [11]. The parton distributions are taken from CTEQ4L. A multiple-interaction model is used, with varying impact parameter and running p_{T} cut-off, tuned to reproduce existing low-energy data [12]. A GEANT3-based program simulates the effect of the LHCb apparatus, and is used to reconstruct the events. It includes all secondary interaction processes, with thresholds of 1 MeV for electrons/photons and 10 MeV for hadrons. The results presented here are based on a sample of 150 000 events of signal and background decays.

The description of the RICH detectors follows as closely as possible the designs given in this report, including radiator volumes, mirrors, vessel walls and photodetector planes. Events were generated and the input and exit points of all charged particles traversing the radiators were recorded. Information was also recorded for any particle striking the photodetector plane.

The simulation of the Cherenkov process is then performed with custom-written LHCb code after the GEANT step. This enabled studies to be conveniently made with different sets of parameters. Taking the input and exit point of the traversing particle in each radiator, the path length is determined, and the corresponding number of Cherenkov photons calculated from Eq. 1.

The Cherenkov generation is performed over the photon energy intervals $1.75 < E_\gamma < 7\,\mathrm{eV}$ for the gases, and $1.75 < E_\gamma < 3.5\,\mathrm{eV}$ for aerogel, for which a plastic window cuts off the high energies. The variation of refractive index with photon energy is parametrized using the Sellmeir coefficient formalism, as indicated in Fig. 8. Photons are generated with this chromatic dependence and their emission point distributed uniformly along the particle trajectory. Each photon is traced through the counter until it reaches the detector plane, or leaves the acceptance. The following sources of photon loss are considered:

1. *Mirror reflectivity:* 90% is assumed, independent of wavelength in the region of interest, following measurements made of prototype mirrors;
2. *Quartz window:* foreseen to isolate the photodetectors from the radiator gas, an 8% loss is included;
3. *Rayleigh scattering:* in the aerogel, where a clarity coefficient of $C = 0.008\,\mu\mathrm{m}^4/\mathrm{cm}$ is assumed (see Section 2.3);
4. *Detection efficiency:* of photoelectrons in the HPD, discussed below, 90% is assumed.

The photocathode efficiency is included in the counter simulation at the earliest level of generation, to save computer time.

3.1.1 Photodetector simulation

The photons incident on the photodetector plane are input to an HPD simulation. Within this simulation the HPDs are tiled on the photodetector plane as specified in the engineering design studies, forming a hexagonal close-packed arrangement with 87 mm between tube centres along the local vertical axis, and staggered in the orthogonal coordinate. The shadowing effect of the Mu-metal shields is not implemented, but will be minimized by the foreseen “pointing” layout of the HPDs. A diameter of 75 mm around each tube centre is considered to be sensitive.

The electron optics of the tubes is not modelled in detail. A simple Gaussian smearing of 230 μm is applied to each impact point prior to pixellisation, to account for the point spread function in the optics, mapped back to the photocathode window. An effective square pixel size of 2.4 mm is assumed at the window.

A photoelectron striking a pixel has the possibility to deposit only a fraction of its energy, and then to backscatter. This is modelled and convoluted with a detector response to give a pulse height in the struck pixel. Each pixel may receive hits from more than one photoelectron. A threshold is applied, above which all signal is counted as a single hit in order to simulate the binary electronics. The parameters are adjusted to give the expected single photoelectron detection efficiency of 90%. The simulation supports the possibility of tracking the backscattered photoelectrons onto other pixels, however the probability of secondary hits is found to be negligible compared to backgrounds from genuine tracks.

Information is retained within the simulation on the incident particles and radiator process which gave rise to each hit pixel. This information has been exploited to study, for instance, the Cherenkov angle resolutions and the contribution of secondary tracks.

3.1.2 Simulated backgrounds

The RICH detector simulation produces radiation not only from those primary tracks which pass through the whole radiator length, but from all background sources which appear in the GEANT simulation. These include:

1. *Traversing particles:* HPDs may react not only to incident photons, but also to charged particles passing through the detector, radiating Cherenkov light in the tube window. Within the simulation these particles may arise in both RICH 1 and RICH 2 from wide-angle tracks, and in RICH 1 alone from soft tracks bent backwards in the magnetic field. The incident positions of these tracks are recorded and the HPD response then simulated with a set of parameterized distributions which vary as a function of incident angle. The parameterization was calibrated by comparing data taken in test beams with photodetectors exposed to charged particles, against detailed stand-alone simulations of single tubes.

2. *Scattered photons:* The Rayleigh-scattered photons from the aerogel, discussed above, provide a diffuse background in RICH 1.

3. *Backward-going tracks:* Secondaries which emerge from the beam-pipe or other material into the radiator are simulated, and these include tracks that travel backwards (particularly in RICH 1), which may radiate directly into the photodetectors, giving clusters of hits unfocused by the mirror.

4. *Unreconstructed tracks:* All particles traversing the RICH radiators, that are above threshold, produce Cherenkov light in the simulation. Some of these, due to their wide angle or low momentum, will not be reconstructed by the tracking system, and therefore provide background hits for the pattern recognition.

5. *Electronic and detector noise:* The effect of random noise in the detectors has been studied, and is found to be small until the probability of a pixel firing is increased beyond 1%, much greater than the predicted level of gaussian noise in the front-end electronics. This follows because the ring-images are searched for using the predictions from the tracking system, and the likelihoods of different particle-type hypotheses are then compared; this comparison is robust against additional random hits.

3.1.3 Tracking

Tracking information is essential for the reconstruction of RICH events. Tracker hits are simulated with a resolution of $\sim\ 200\,\mu$m for the outer tracker, and $100\,\mu$m for the inner tracker. Tracks are reconstructed by fitting these, and any Vertex Detector space points, using a Kalman filter method. At present there is no pattern recognition implemented for the tracking, so Monte Carlo truth information is used to feed the fit with the correct string of hits. Tracks are defined which are suitable for the physics analysis, by requiring that the particle passed through the magnet, that it is above 1 GeV, and that it has a minimum number of tracker space points. The RICH performance is evaluated on these well-reconstructed tracks, of which there are typically 30 which pass through the detectors in triggered signal events. The momentum resolution of these tracks is 0.35% for non-electrons. Tracks of lower quality, including those with unreliable or non-existent momentum information, are also fitted. These are used in the RICH pattern recognition to identify background rings caused by low momentum and wide angle tracks resulting from secondary interactions.

3.2 Pattern recognition

A simulated $\mathrm{b}\overline{\mathrm{b}}$ event in the two RICH detectors is shown in Fig. 11 and 12. The two detector planes of each RICH are drawn side by side, dots mark the positions of detected photoelectrons, and the expected ring images are superimposed.

The Cherenkov rings are not perfect circles, but are roughly elliptical in shape, with a degree of distortion that depends on the direction of the track within the acceptance. Instead of attempting to directly fit these rings, a substantial simplification is achieved by reconstructing the Cherenkov angles at emission $(\theta_\mathrm{c}, \phi_\mathrm{c})$ for each hit under the assumption that it originated from a given track [7]. That calculation accounts for the mirror geometry, and involves the solution of a quartic equation [13]. The hits which truly originate from that track will then all have the same value of polar Cherenkov angle θ_c (within the resolution), and have uniformly distributed azimuthal angle ϕ_c.

The task of the pattern recognition is to assign a particle type to each track, so as to best describe the observed hits. Two approaches have been developed: a “local” method which treats each track separately (and is therefore fast), and a “global” method that optimises the assignment of particle types for all tracks in RICH 1 and RICH 2 in the event simultaneously, to give the most accurate possible particle identification. A third approach is also under study, searching for rings in the RICH data, without relying on the information from the tracking detectors: this may be useful as a later stage in the reconstruction, to help in the rejection of background hits after a first pass has been made using the tracking information [14].

3.2.1 Local analysis

In the local method [15] each track is taken in turn, and the Cherenkov angle of each hit in the detector is calculated relative to that track. For each track a log-likelihood function is calculated, proportional to:

$$\sum_i \ln\left(1 + \frac{1}{\sqrt{2\pi}\sigma_\theta \kappa}\,\exp\left[-\frac{(\theta_i - \theta_x)^2}{2\sigma_\theta^2}\right]\right)\ , \tag{2}$$

where θ_i is the reconstructed emission angle of hit i, θ_x is the expected emission angle of the track under particle-type hypothesis x, and σ_θ is the angular resolution. κ is a hit selection parameter, which defines an effective bandwidth around the considered Cherenkov angle θ_i; a value $\kappa = 1$ is found to give the best performance. The normalisation is chosen such that the value of the log-likelihood function corresponds to the number of hits expected at angle θ. The sum is performed over all hits, but excludes those with θ_i much greater than the saturated Cherenkov angle to save CPU time.

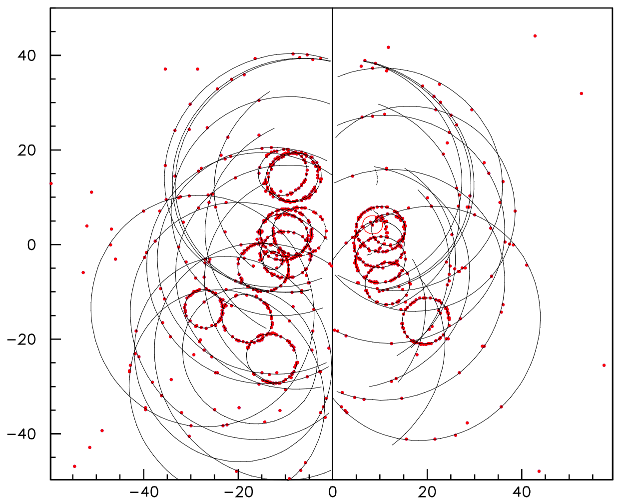

Figure 11: Event display of a simulated $B_d^0 \to \pi^+\pi^-$ event, with the photodetector planes of RICH 1 drawn side by side (scale in cm), and the Cherenkov rings superimposed.

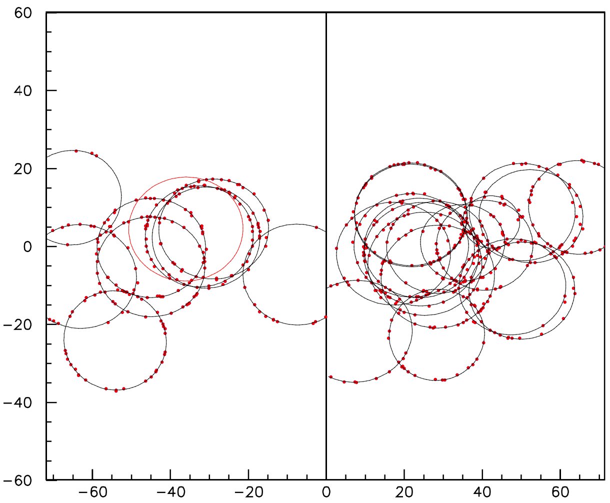

Figure 12: Event display of the same event as Fig. 11, for RICH 2.

The log-likelihood function is used to calculate the number of hits which can be attributed to a given particle-type hypothesis, evaluated at the mean Cherenkov emission angle. A Poisson probability is then calculated from the comparison of the number of reconstructed hits with the number expected, from Eq. (1), and this is used to discriminate between the different particle hypotheses.

This algorithm is a factor of 5 faster than the standard (global) approach. The possibility of using it in the trigger, at Level-3, is under study.

3.2.2 Global analysis

Instead of treating each track separately, in the global method [13] the likelihood is constructed for the whole event. In this way the main "background" for a track in the local method, due to hits from other tracks, is correctly accounted for. For a given choice of particle type for each track, a likelihood is calculated that all the hits observed were produced by the tracks reconstructed in the event, plus unseen secondaries, noise etc. The particle-type assumptions are then changed and the likelihood recalculated; in this way the set of particle types that maximises the likelihood is searched for.

The event likelihood is calculated by comparing the number of photoelectrons detected in each pixel with the number expected in that pixel from all sources: signal (the Cherenkov rings from the various radiators), and backgrounds (from scattering in the aerogel, rings with no reconstructed tracks, electronic noise, etc.). A fitting function is calculated as the expected number of photoelectrons detected in each pixel, for a given choice of particle types for the tracks in the event. For the signal from a single track, that fitting function takes the form of a ring with roughly Gaussian cross-section in radius (the parametrization is Gaussian as a function of the Cherenkov emission angle θ_c, and that is then converted to the detector plane using the RICH optics). The fitting function is illustrated in Fig. 13 for a zoomed region of Fig. 11, for a given set of track hypotheses. The likelihood is then determined from comparison of the fitting function and the observed photoelectron signals. It has the form [13]:

$$\begin{aligned}\ln\mathcal{L} = & -\sum_{\text{track}\,j}\mu_j + \\ & \sum_{\text{pixel}\,i} n_i \ln\left(\sum_{\text{track}\,j} a_{ij} + b_i\right),\end{aligned} \tag{3}$$

where a_{ij} is the expected number of detected

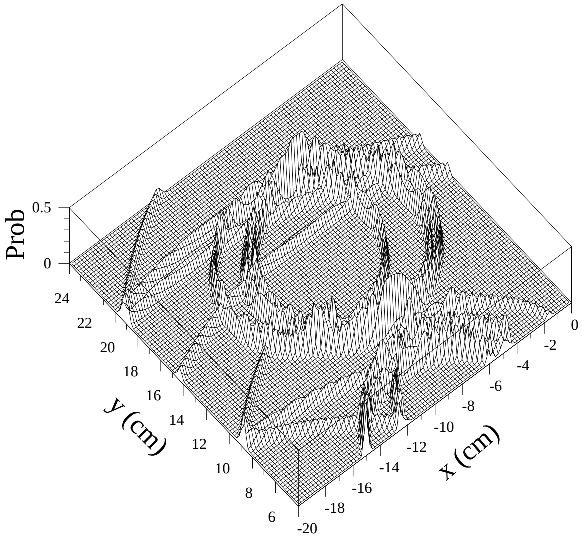

Figure 13: Expected number of photoelectrons in each pixel, for a region of the event shown in Fig. 11, under a given assumption of particle types for the tracks (×10 for the aerogel rings, for clarity).

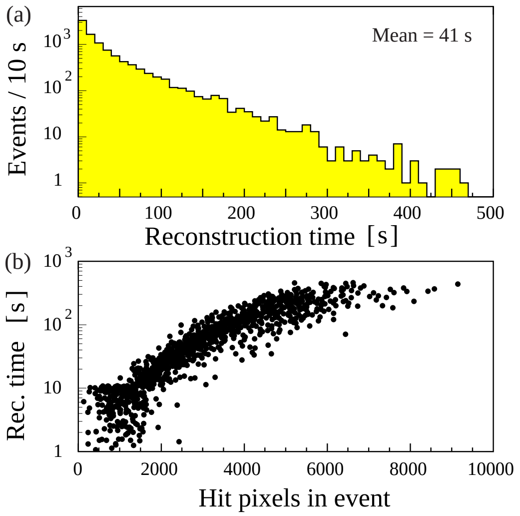

Figure 14: The CPU time of the RICH reconstruction and pattern recognition for triggered and accepted signal events, and the dependence of the reconstruction time on the number of hit RICH pixels in the event.

photoelectrons from track j in pixel i (under a given set of track particle-type hypotheses), and $\mu_j = \sum_i a_{ij}$ is the expectation for the total number of detected photoelectrons from track j; n_i is the number of photoelectrons falling into pixel i; b_i is the expected background falling in pixel i from sources without a reconstructed track. The size and distribution of this background contribution is a priori unknown for the event, but a sensible estimate can be made from the multiplicity of hits in the tracking stations adjacent to the RICH detectors. The first summation is made once per event and then modified per iteration as each track hypothesis is altered, whilst the second is made over *hit* pixels and so is reasonably fast.

One advantage of this approach is that the detailed description of backgrounds is easily included. For example, the distribution of scattered photons from the aerogel, relative to the incident track direction, has been parametrized using the simulation. The resulting contribution has been included for each track in the fitting function.

Although the pattern recognition results are only of interest for those tracks useful in the physics analysis, it is important to include all possible tracking information. Therefore all reconstructed tracks above a minimum standard are included, with their quality flagged to the algorithm by the assignment of an appropriate Cherenkov angle resolution error.

The search for the maximum-likelihood solution is initiated with all tracks taken as pions (the most numerous particle type). The assumption for each track is then changed in turn to each of the other possible hypotheses, and the change which gives the largest increase in event likelihood is chosen. This procedure is then iterated until no further improvement in likelihood is seen.

It is possible to improve the results by repeating the maximum-likelihood search a second time with an improved background estimation. The expected number of photoelectrons seen in each HPD based on the results of the first search is compared with the observed number, and the difference attributed to that background induced by particles without track information. A second maximum-likelihood search is performed with this new estimate. This properly accounts for biases

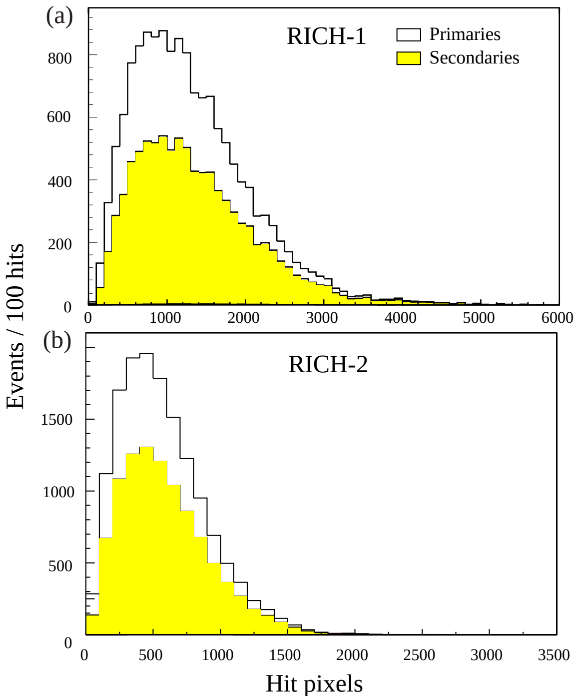

Figure 15: Number of hit pixels per event in Level-0 triggered and accepted two-body events for (a) RICH 1, (b) RICH 2.

caused by, for instance, local hot spots arising from charged particles incident on HPD windoes.

Figure 14 shows the number of seconds per event spent on the reconstruction and pattern recognition for single signal events decaying within the LHCb acceptance and passing the Level-0 trigger. This is measured on a machine of 100 MIPS processing power. The time taken increases strongly with the hit multiplicity, as expected, but the mean of about 40 seconds per event is acceptable. Further optimisation of the speed could still be made if needed.

3.3 Performance

3.3.1 Photon yield and resolution

Figure 15 shows the number of hit pixels per event for single signal events decaying within the LHCb acceptance and passing the Level-0 trigger. As can be seen, a large fraction of the observed hits ($\sim$ 70% overall) originate from tracks produced in secondary interactions.

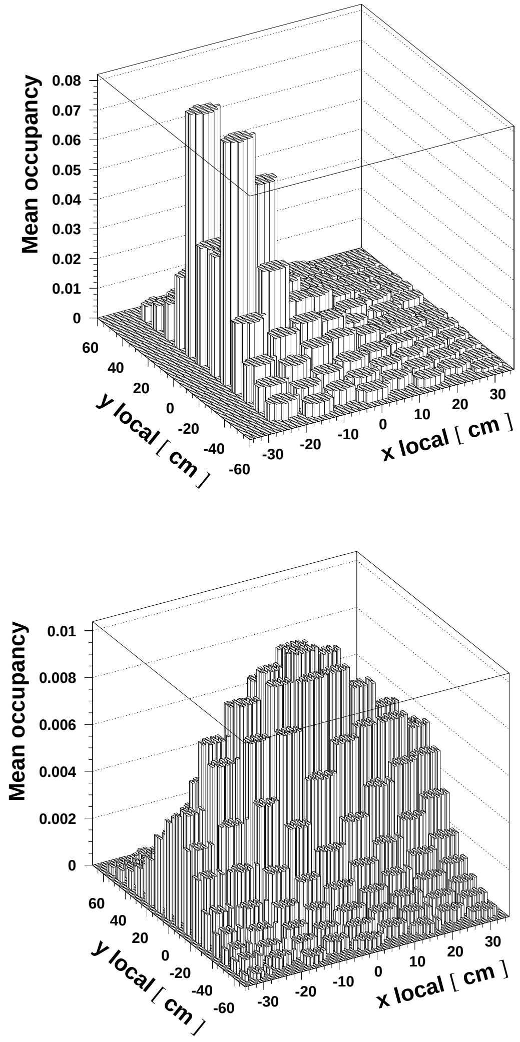

Figure 16: Occupancy as a function of position on the photodetector plane, for RICH 1 (above), RICH 2 (below).

The resulting occupancy of the photodetectors for triggered and accepted signal events is shown in Fig. 16, as a function of position on the photodetector plane. It is highest in RICH 1, in the region illuminated by tracks at low angle, and reaches 8% there. Over the rest of RICH 1, and all of RICH 2, the occupancy is below 1%.

The mean number of detected photoelectrons from a saturated track is listed for the three radiators in Table 1. The resolution on the reconstructed Cherenkov angle for such

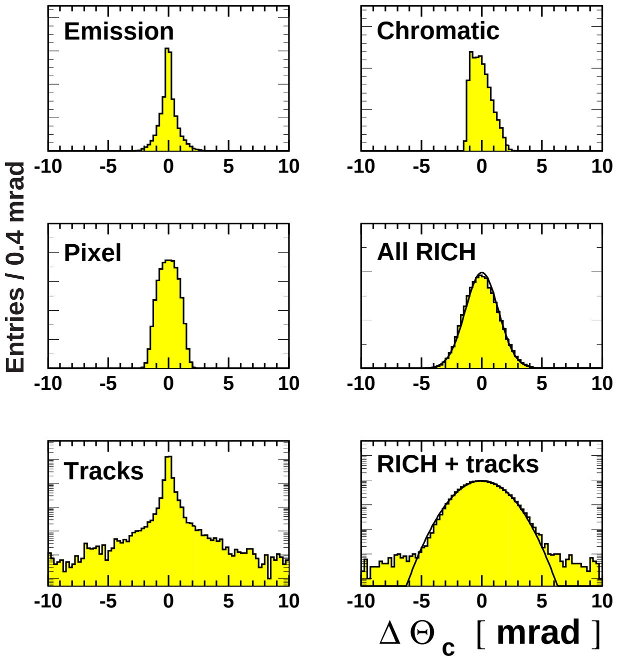

Figure 17: Components of the single photon Cherenkov angle resolution for C_4F_{10}. Shown on a linear scale are the emission point, chromatic and pixel distributions, and the convolution of these three ('all RICH'). Shown on a logarithmic scale are the tracking component and the total resolutions with all contributions present.

tracks has contributions that are also listed in Table 1. These contributions are determined from the RMS widths of the distributions obtained with each feature in turn enabled in the simulation. Figure 17 shows the components of the resolution for C_4F_{10}. The final resolution is Gaussian with a small tail arising from imperfections in the tracking. The values of the final resolutions per photoelectron are 2.00, 1.45 and 0.58 mrad for the aerogel, C_4F_{10} and CF_4 radiators respectively.

3.3.2 Particle identification

The performance of the RICH reconstruction has been tested using all of the tracks that pass through the RICH detectors in simulated $B^0_d \to \pi^+\pi^-$ events. The results are shown in Table 3. Each track gives a single entry: the column gives the true particle type (or X if the track is below threshold in all radiators) and the row gives the reconstructed particle type (or X if the track is reconstructed as being below threshold in all radiators). The performance can be quantified in terms of the efficiency ε (the fraction of true particles of a given type that are identified correctly) and the purity $\mathcal{P}$ (the fraction of tracks that have been identified as a given particle type that are truly that type). As can be seen, the efficiencies are typically better than 80%. The purities are also high, except for muons, which suffer from significant pion contamination due to the much larger number of pion tracks (close in mass to the muon).

Instead of simply choosing the maximum-likelihood solution, the separation between different particle hypotheses can be varied. This is expressed in terms of Gaussian sigma using the correspondence $N_\sigma = \sqrt{2\,\Delta\ln\mathcal{L}}$, where $\Delta\ln\mathcal{L}$ is the difference in log-likelihood between the two hypotheses ($N_\sigma > 0$ for the nominal maximum-likelihood requirement).

Table 3: Results from the global pattern recognition applied to well reconstructed tracks in triggered and accepted signal events between 1 and 150 GeV/c. Each track gives one entry in the table, and X denotes tracks below threshold in all radiators; the rows give the reconstructed particle type, $\mathcal{P}$ is the purity and ε the efficiency. The sample corresponds to 500k tracks, but has been renormalised to 1000.

	True particle type						
Rec	e	μ	π	K	p	X	$\mathcal{P}$
e	97.4	0.7	24.6	1.4	0.5	3.1	0.76
μ	4.0	8.7	69.5	2.0	0.5	4.9	0.10
π	2.5	1.3	545.7	3.3	0.7	5.1	0.98
K	0.3	0.1	12.7	70.6	4.8	4.3	0.76
p	0.2	0.0	1.7	4.3	35.9	0.0	0.85
X	9.9	0.8	19.8	3.2	0.0	55.6	0.62
ε	0.85	0.76	0.81	0.83	0.85	0.76	

Figure 18 shows the average number of sigma separation versus momentum between the pion and kaon hypotheses for true pions in triggered and accepted signal events. Bet-

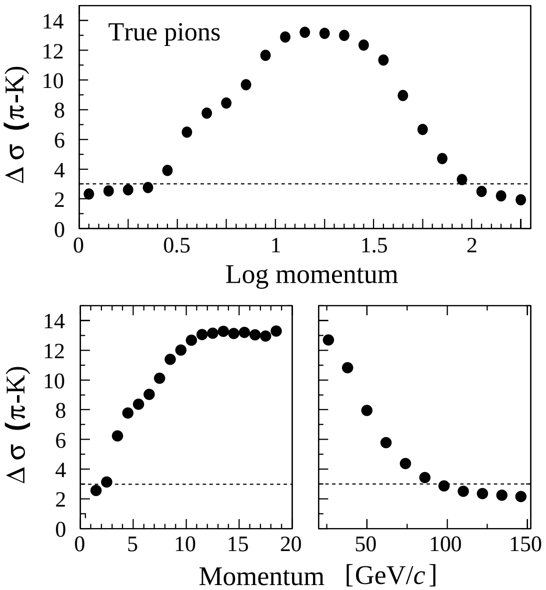

Figure 18: Number of sigma separation between pion and kaon hypothesis versus momentum for true pions in triggered and accepted signal events. Top: logarithmic momentum scale, Bottom: linear momentum scales.

ter than $3\,\sigma$ separation is achieved for particles with momenta between 2 and $100\,\mathrm{GeV}/c$, with useful separation extending down to $1\,\mathrm{GeV}/c$ and up to $150\,\mathrm{GeV}/c$.

Figure 19 shows the same information for events of low, medium and high multiplicity, defined by bins of $0 - 1000$, $1000 - 2000$ and > 2000 hit pixels in RICH 1. The significance of the separation is reduced for high multiplicity events, particularly in the intermediate momentum region; however, the performance at the low- and high-momentum limits is not strongly affected.

The particle-identification efficiency is shown as a function of momentum in Fig. 20, for pions and kaons. Here a pion is considered successfully identified if the particle-type hypothesis selected is that of a pion or lighter particle (π, μ or e), and similarly for the kaon if the selected hypothesis is that of the kaon or heavier particle (K or p).

3.3.3 Two-body B decays

Isolation of the two-body decays $\mathrm{B_d^0} \to \pi^+\pi^-$ and $\mathrm{B_s^0} \to \mathrm{K^+K^-}$ is described in detail in [10].

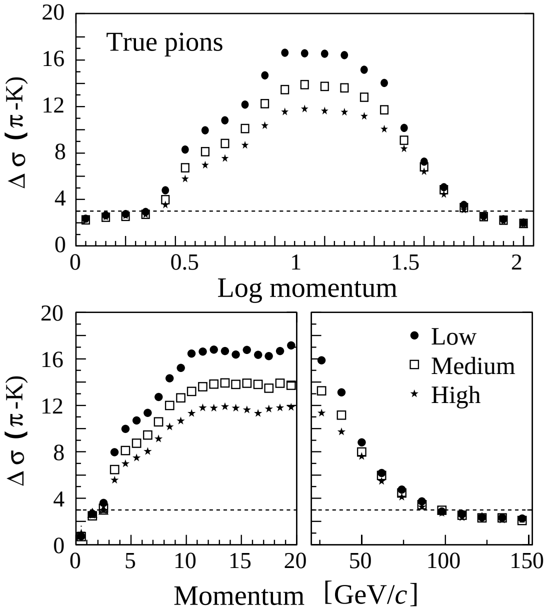

Figure 19: Number of sigma separation between pion and kaon hypothesis versus momentum for true pions in triggered and accepted signal events, in different bins of RICH 1 multiplicity. Top: logarithmic momentum scale, Bottom: linear momentum scales.

The two-body mass spectrum for the $\mathrm{B_d^0} \to \pi^+\pi^-$ selection was shown in Fig. 2, before the use of RICH information. A momentum cut of < 150 GeV/c has been imposed on both candidate tracks. The following branching ratios have been assumed: 0.5×10^{-5} for $\mathrm{B_d^0} \to \pi^+\pi^-$ and $\mathrm{B_s^0} \to \mathrm{K^-}\pi^+$, 1.9×10^{-5} for $\mathrm{B_d^0} \to \mathrm{K^+}\pi^-$ and $\mathrm{B_s^0} \to \mathrm{K^+K^-}$, and 8×10^{-5} for $\Lambda_\mathrm{b} \to \mathrm{p}\pi^-$ and $\Lambda_\mathrm{b} \to \mathrm{pK^-}$; no combinatoric background is included. Without the RICH, the backgrounds dominate. Particle identification in the RICH system is applied by demanding that both tracks be identified as a pion or lighter particle. The resulting mass spectrum is shown in Fig. 21: the signal events now dominate. Tighter cuts could be applied to further reduce the background, if required, at the cost of efficiency loss; the change in the selected sample as the particle-identification cuts are varied will give a strong control of the background.

Figure 22 (a) shows the momentum spectrum of those tracks correctly and incorrectly identified by the RICH in the $\mathrm{B_d^0} \to \pi^+\pi^-$ se-

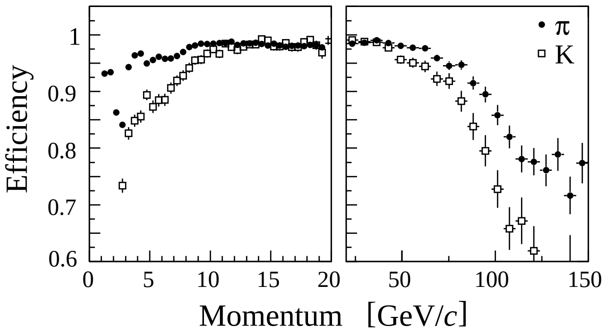

Figure 20: Identification efficiency for pions and kaons versus momentum, for triggered and accepted signal events.

lection. It can be seen that a large fraction of the misidentified kaons are of high momentum.

3.3.4 Multi-body B decays

Separation of the decays $B_s^0 \to D_sK$ and $B_s^0 \to D_s^-\pi^+$ is described in detail in [10].

The mass spectrum for the $B_s^0 \to D_sK$ selection was shown in Fig. 3, before the use of RICH information on the π or K coming directly from the B_s decay. Prior to particle identification the signal is submerged under background from $B_s^0 \to D_s^-\pi^+$ decays; no combinatoric background is included. It has been assumed that the branching ratio for $B_s^0 \to D_s^-\pi^+$ is 15 times higher than that for $B_s^0 \to D_sK$. This background is almost entirely removed using the RICH. A momentum cut of < 150 GeV/c has been imposed on the candidate kaon. For the RICH selection it is demanded that the candidate track be identified as a kaon or heavier particle. The resulting mass plot after particle identification is shown in Fig. 23.

Figure 22 (b) shows the momentum spectrum of those tracks correctly and incorrectly identified by the RICH in the $B_s^0 \to D_sK$ selection.

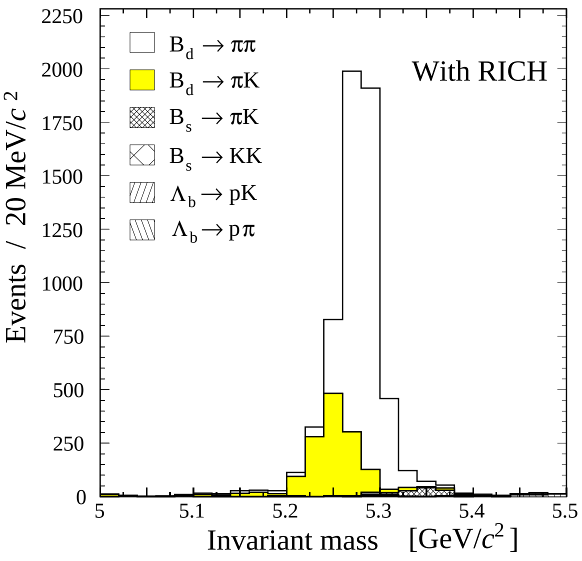

Figure 21: Mass spectrum of $B_d^0 \to \pi^+\pi^-$ candidates after the RICH selection has been applied.

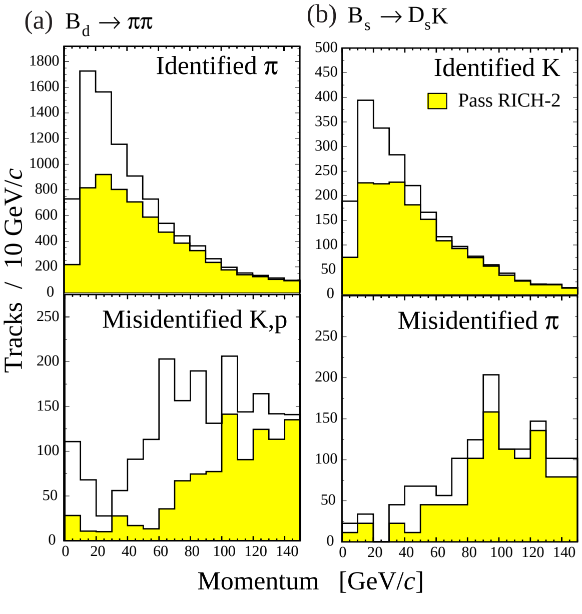

Figure 22: Momentum of tracks correctly and incorrectly identified by the RICH in (a) the $B_d^0 \to \pi^+\pi^-$ selection, (b) the $B_s^0 \to D_sK$ selection. The tracks which pass through RICH 2 are indicated by the shaded histograms.

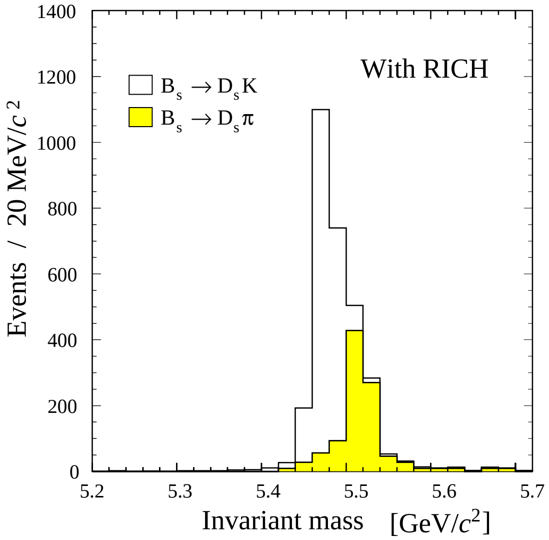

Figure 23: Mass spectrum of $B_s^0 \rightarrow D_s K$ candidates after the RICH selection has been applied.

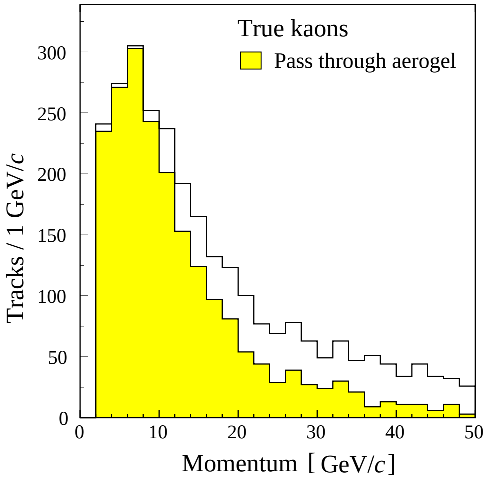

Figure 24: Momentum distribution of true kaons after tag pre-selection, and prior to application of RICH information for accepted signal events, passing Level-0 and Level-1 triggers. Also indicated are those kaons that pass through the aerogel.

3.3.5 Kaon tagging

The performance of the RICH has been investigated in tagging the initial-state flavour of B mesons. For this study two-body decays were considered which had both tracks within the acceptance, and which passed the Level-0 and Level-1 triggers. (The Level-1 trigger is included here, as it selects events with secondary vertices, which will affect the impact-parameter distribution of tracks, used in selecting kaon tag candidates.)

A set of pre-selection cuts were applied to isolate candidate tracks with a high probability of being decay products from the accompanying decaying b hadron in the event. These were:

1. transverse momentum greater than 0.4 GeV/c;
2. impact-parameter significance greater than 3 and an absolute impact parameter less than 3 mm;
3. momentum greater than 2 GeV/c;
4. Vertex Detector hits on the track.

An average of about three candidates pass this selection per event, of which $\sim 15\%$ are kaons. The momentum spectrum of these kaons is shown in Fig. 24, peaked towards low momentum as expected.

The RICH selection is then applied. Tracks are selected as kaons if they have an assigned kaon hypothesis and are above threshold. The efficiency and purity of this selection as a function of momentum are shown in Fig. 25 and 26. The mean efficiency is $(85.6 \pm 0.6)\%$ and mean purity is $(82.2 \pm 0.7)\%$.

The charge of the selected kaon is then used to tag the flavour of the event. If more than one kaon passes all the cuts, that with the highest impact parameter is chosen. The performance is shown in Fig. 27. $(31.2 \pm 0.5)\%$ events have a kaon tag, and of these $(31.0 \pm 0.9)\%$ are incorrectly tagged. For comparison, perfect kaon identification would give an efficiency of $(30.6 \pm 0.5)\%$ and mistag rate of $(26.8 \pm 0.9)\%$. The mistag rate, ω, and efficiency, ϵ, may be combined into a tagging power, $\mathcal{P}$, which expresses the statistical performance of the tag:

$$\mathcal{P} \;=\; \sqrt{\epsilon}\,(1 - 2\omega) \;.$$

For perfect identification $\mathcal{P} = 0.257$, whereas for the RICH $\mathcal{P} = 0.212$. This matches the

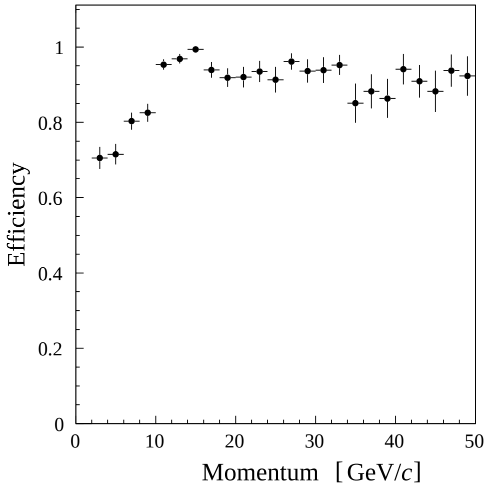

Figure 25: Kaon tag efficiency versus momentum for accepted events passing the Level-0 and Level-1 triggers.

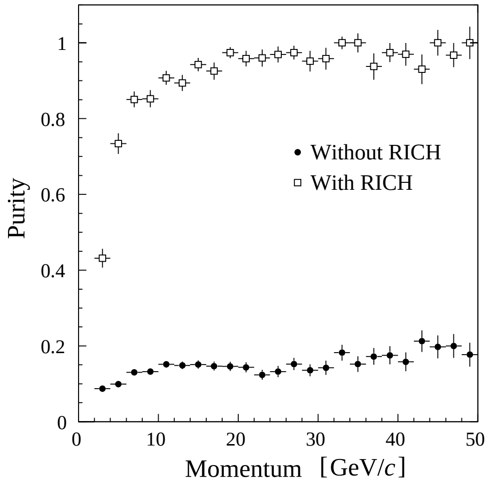

Figure 26: Kaon tag purity versus momentum for accepted events passing the Level-0 and Level-1 triggers; the performance before the use of RICH information is also shown.

performance that was assumed for the physics studies presented in the Technical Proposal [1].

3.3.6 Tracking requirements

The dependence of the particle-identification performance on the precision of the track parameters has been investigated [15, 13]. As can be seen in Fig. 28, no significant degradation is seen as long as the momentum resolution satisfies $\Delta p/p < 0.01$, and the track angular resolution is better than 1 mrad in RICH 1 and 0.3 mrad in RICH 2. These requirements are satisfied by the tracking system of LHCb.

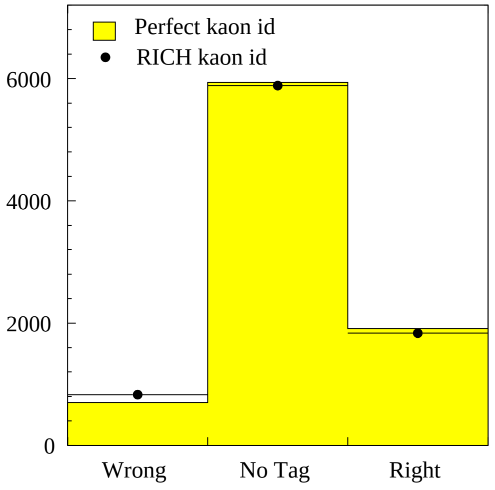

Figure 27: Kaon tag performance for accepted signal events passing the Level-0 and Level-1 triggers, showing the relative contributions of no tag, right tag and wrong tag. The performance is indicated for perfect kaon identification, and for the RICH.

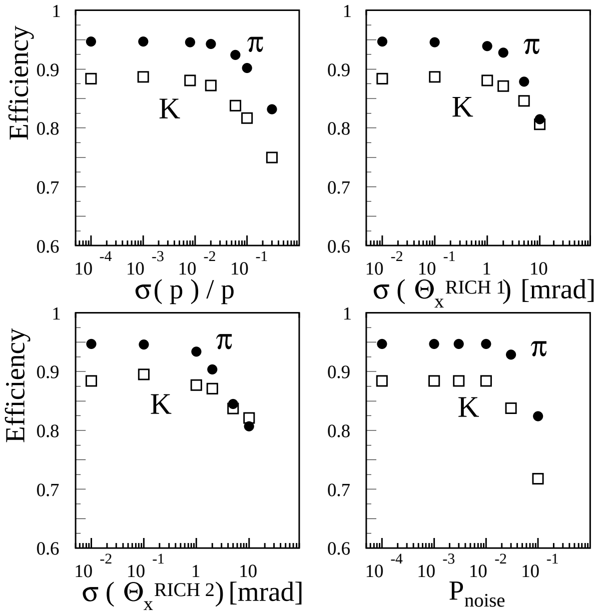

Figure 28: Variation of the identification efficiency with tracking performance and detector noise level.

3.3.7 Future developments

A smooth migration is planned from conventional software to a fully object-oriented implementation. The basis of the migration is the new detector analysis environment [17], that allows the use in parallel of code written in FORTRAN and new algorithms written in C^{++}.

To ease the migration an object-oriented approach to the RICH reconstruction has been studied, in parallel to the baseline reconstruction program. The development was based on the unified software development process [18]. In a first iteration the problem domain was analysed by means of a detailed description of the detector and the relevant physics processes. In addition the reconstruction algorithm was defined by the baseline program [13]. When applicable, so-called use-cases were applied to describe important aspects.

Entities most relevant for the reconstruction process have been identified. Their relations have been studied and an object model has been developed. It is characterised by so-called "smart" event and detector entities, that provide support for a customisable reconstruction algorithm. For example, the track objects can be interrogated not only about simple track parameters such as their momentum or angle, but also more complex quantities such as the length of radiator that they traverse in each RICH.

Care has been taken to decouple dependencies. Event entities within the reconstruction algorithm are related to the event model of LHCb by a so-called adapter pattern [19]. This concept provides smart entities for the reconstruction, whilst shielding the reconstruction environment from development of the global event model.

In a similar way the actual reconstruction algorithm is implemented by a strategy pattern. This allows a customisable reconstruction framework to be developed, that can be used in the future for the implementation of different algorithms.

Currently the development has reached a state that allows a comparison to be made with the results presented in the Technical Proposal [1]. As an important step, the physics performance and resource consumption have been studied and are found to be equivalent [20]. A full implementation, considering the updated geometry and additional sources of detector noise, is foreseen in the near future.

4 Prototype results

4.1 Overview

There has been an intensive programme of development work undertaken for the LHCb RICH detectors. A summary of the work is described in this section.

Prototypes of the RICH 1 and RICH 2 detectors have been constructed to study a number of important properties of radiators and photodetectors in a test-beam and in the laboratory. These studies include measurement of:

1. The performance of the aerogel radiator, its photon yield, scattering properties, clarity and refractive index;
2. The simultaneous detection of Cherenkov rings from gaseous and aerogel radiators;
3. The characteristics of the C_4F_{10} and CF_4 gas radiators, the photon yield and chromatic properties;
4. The performance of HPD's for detecting Cherenkov photons, the efficiency, and the resolution of the Cherenkov angle;
5. The detailed electron optics of prototype Pixel HPD tubes, including a full-scale tube with 72-18 mm demagnification;
6. The operation of Pixel HPD tubes in the presence of a magnetic field;
7. The behaviour of the HPD detectors when charged particles pass through the device.

In addition, a programme of work to evaluate the optical characteristics of prototype mirrors and the stability of their supports is well underway. The methods used for measuring the optical and mechanical properties of mirrors and supports are also described below.

4.2 Prototype tests

4.2.1 The RICH 1 and RICH 2 prototype detectors

The beam tests described here used prototypes of the LHCb RICH 1 and RICH 2 counters in a number of configurations :

1. A $\frac{1}{4}$-scale prototype of the RICH 1 detector [21], shown schematically in Fig. 29. The purpose of this prototype was to simultaneously measure Cherenkov rings from aerogel and gaseous radiators, either air or C_4F_{10}. A 240 mm focal-length mirror reflected the Cherenkov rings onto an array of seven commercial 61-pixel Hybrid Photo-Diodes (HPD's) at the photodetection plane.
2. A full-scale RICH 1 prototype was constructed by adding extension tubes to increase the gaseous-radiator length to 100 cm [21], and to focus the rings onto the photodetector plane using a 1117 mm focal-length mirror.
3. A full-scale prototype of the RICH 2 [22], is shown schematically in Fig. 30. A 4003 mm focal length mirror reflected Cherenkov photons from approximately 1.8 m of CF_4 gaseous radiator onto an array of seven HPD's and a single Multi-Anode Photomultiplier (MAPMT) at the photodetection plane.

A variety of photodetectors were used in the beam studies :

1. The 61-pixel HPD manufactured by DEP[2]. This HPD, shown schematically in Fig. 31, has an S20 (trialkali) photocathode deposited on a quartz window. Photoelectrons are accelerated through a 12 kV potential onto a 61-pixel silicon detector. This device gives an approximate gain of 3000. The pixels are hexagonally close packed and measure 2 mm

---

[2] Delft Electronische Producten(DEP), The Netherlands

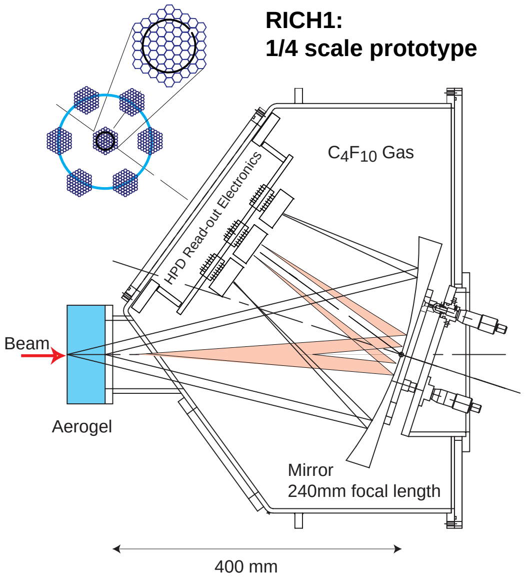

Figure 29: Layout of the $\frac{1}{4}$-scale prototype of the RICH 1 detector.

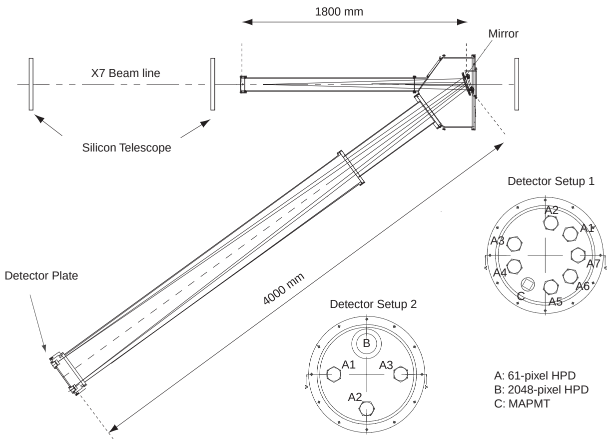

Figure 30: Schematic diagram of the RICH2 test beam setup and two photodetector configurations.

between their parallel edges. The signal is read out by a Viking VA2 [23] ASIC. Using the measurements made by DEP, the quantum efficiency of the S20 photocathode is shown in Fig. 32 as a function of the photon wavelength, and compared to the 2048-pixel HPD (see below).

2. A 2048-pixel HPD, manufactured in collaboration with DEP. This device is described in Section 4.3.

3. A full-scale prototype Pixel HPD with a 61-pixel silicon sensor, manufactured in collaboration with DEP. This device is also described in Section 4.3.

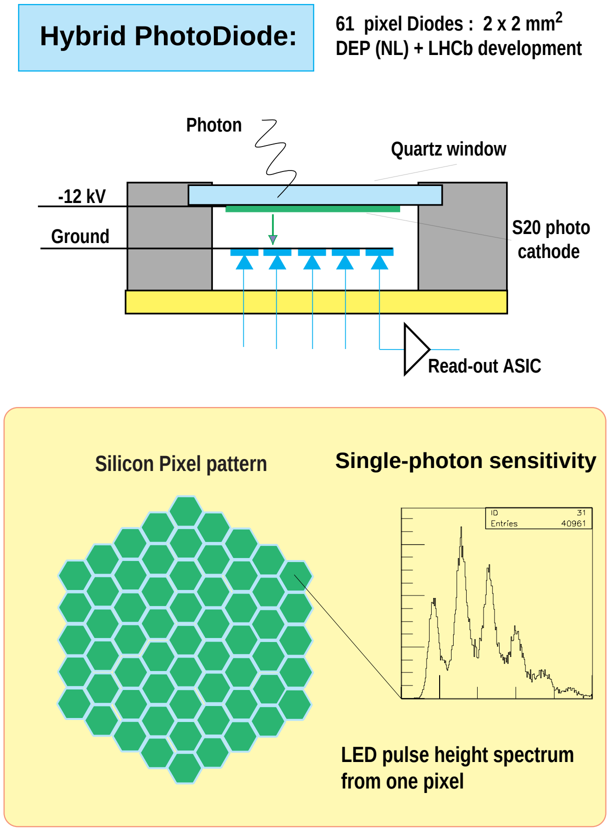

Figure 31: A schematic of the 61-pixel HPD

4. The Pad HPD, fabricated in-house at CERN [24]. This consists of a vacuum tube of 12.7 cm diameter, with a 2.3 fold demagnified image on the silicon sensor which consists of 2048 1 mm×1 mm pixels. The low noise analogue chain was based on Viking VA3 chips.

5. The 64-channel MAPMT manufactured by Hamamatsu. The performance of this device is summarized in Appendix A.

4.2.2 Simultaneous detection of gas and aerogel rings in RICH 1

The $\frac{1}{4}$-scale prototype of the RICH 1 was used to simultaneously measure Cherenkov rings

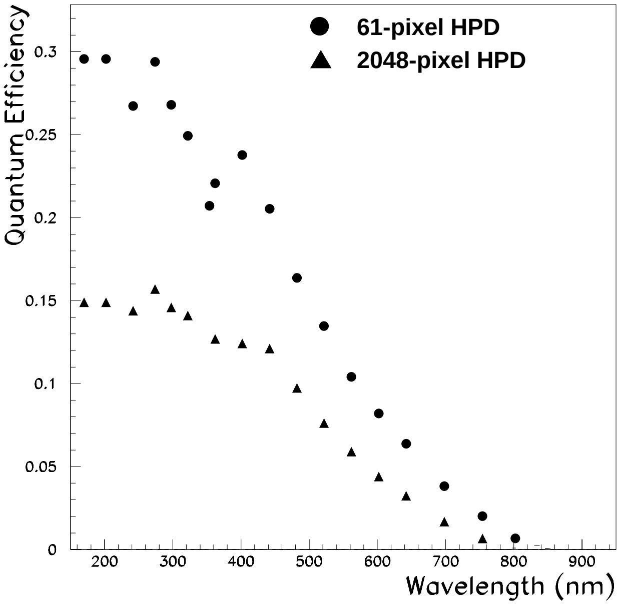

Figure 32: Quantum efficiencies of the 2048-pixel HPD and the 61-pixel HPD as a function of photon wavelength.

from aerogel and C_4F_{10}. The C_4F_{10} was contained within a volume of length 40 cm between a Mylar window and the mirror, and samples of aerogel were placed at the beam entrance window. Aerogel with nominal refractive index $n = 1.03$ was procured from KEK and Matsushita.[3]

Figure 33 shows data taken with a 10 GeV/c π^- beam, with an 18 mm thickness of aerogel (KEK) and C_4F_{10} radiator. The C_4F_{10} ring is too large to be contained within the central HPD; the radius of the arc is compatible with that expected from the refractive index of 1.0014. The outer HPD's exhibit the ring from the aerogel radiator, clearly demonstrating the simultaneous detection of gas and aerogel rings.

4.2.3 Radiator properties

RICH 1 C_4F_{10} gas radiator

The number of photoelectrons per event and the Cherenkov angle resolution have been measured for C_4F_{10}, air and aerogel in the $\frac{1}{4}$-scale prototype with a 10 GeV/c π^- beam. Comparisons have been made with expectations from a detailed simulation of the prototype geometry, incorporating measurements of optical transmission and reflection for each of the elements.

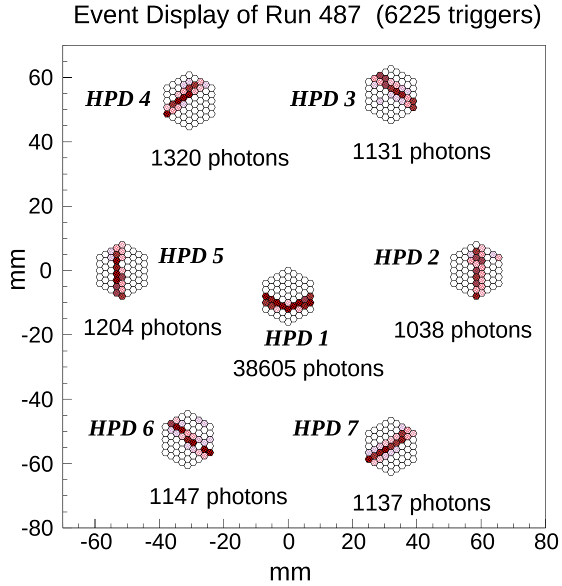

Figure 33: Display of the hits in a run taken with a pion beam in the $\frac{1}{4}$-scale prototype, showing the rings from aerogel and C_4F_{10} radiators.

The numbers of photoelectrons per event were counted for the gaseous radiators and the aerogel, with and without Mylar filters (which absorb wavelengths below 350 nm). The background to the raw photoelectron count was estimated by counting hit pixels not in the signal region. For the air and C_4F_{10} radiators the background correction is small ($\sim$5%), whereas for the aerogel samples it is $\sim$25%. The background consists of photoelectrons from scattered photons in the aerogel, a contribution from backscattered photoelectrons in the HPD's, and electronic noise. Efficiency corrections include losses due to a $3\,\sigma$ pedestal cut and the geometrical acceptance of the photodetectors. The results are shown in Table 4. The observed values are in excellent agreement with simulation, which includes photon absorption and reflection, the quantum efficiency and wavelength cutoff of the phototube, and backscattering of photoelectrons at the HPD

---

[3] Supplied by E. Nappi, Univ. of Bari, Italy.

Radiator	N_{obs}	N_{corr}	$N_{\text{corr}}/N_{\text{pred}}$
Air 40 cm	4.9	4.8	0.99
C_4F_{10} 40 cm	7.9	32.7	1.06
Aerogel 1.8 cm	1.8	10.7	0.82

Table 4: Numbers of photoelectrons per event for the various radiators. N_{obs} is the observed number, N_{corr} is the number after background and acceptance correction, and N_{pred} is the predicted number from the simulation. The aerogel sample is from KEK.

Source	No Mylar	Mylar
Chromatic aberration	1.03	0.20
Emission point uncertainty	0.58	0.58
Finite pixel size	0.56	0.56
Gas pressure variations	0.02	0.02
Particle trajectory error	0.28	0.58
Total predicted	1.34	1.01
Total observed	1.40	1.10

Table 5: Predicted Cherenkov-angle resolution in RICH 1 prototype. Contributions (in mrad) and comparison with the observed value (with and without Mylar filter).

anode.

From the estimate of the photoelectron yield (N_{pe}) of a photodetector, the figure of merit (N_0) is calculated using:
$N_0 = N_{pe}/(\epsilon_A L \sin^2\theta_c)$
where ϵ_A is the fraction of the Cherenkov ring covered by the photodetector, L is the length of the radiator and θ_c is the mean Cherenkov angle. Using the observed yields, the figure of merit is estimated to be 250 cm^{-1} for C_4F_{10} and 50 cm^{-1} for the aerogel (with Mylar filter).

The Cherenkov angle resolution was measured in the full-scale prototype of RICH 1. Rings were reconstructed in the detector plane by fitting an ellipse to the observed hits. The centre of the ellipse was measured to an event-by-event precision of 0.58 (0.28) mrad for the detectors with (without) a Mylar filter placed in front of them.

Sources of uncertainty which limit the Cherenkov angle resolution were included in the simulation, and are as follows :

1. Chromatic Error: This is due to the variation of refractive index of the radiator with wavelength and is largest in the UV region. Use of Mylar filters reduces this contribution.

2. Emission point uncertainty: This arises due to the fact that the beam trajectories do not pass through the centre of curvature of the mirror. The magnitude of this effect is increased due to the substantial tilt angle of the mirror with respect to the beam axis in this measurement. The emission point is assumed to be in the middle of the radiator, regardless of the true but unknown point of emission.

3. The pixel size of the photodetector.

4. Measurement of beam trajectory: This contribution depends on the method used to determine the particle trajectory. When the beam telescope is not used, the error is determined by the precision in locating the centre of the ellipse fit to the ring. When the beam telescope is used the error is due to the granularity of its silicon detector pixels.

The predicted resolution contributions are listed in Table 5 for a 15.5 GeV/c π^- beam. The combined total is in excellent agreement with the observed value. When a silicon telescope is used to determine the beam trajectory, a resolution of 1.06 mrad is measured (with Mylar filter), close to the expectation of 0.96 mrad from simulation.

RICH 2 CF_4 gas radiator

The contributions to the resolution for CF_4 gas have been studied from reconstruction of Cherenkov rings in the full-scale RICH 2 prototype. The beam provided negative particles (mainly pions) with momenta of 120 GeV/c. During different data-taking periods, air and CF_4 were used as radiators, with pressure and temperature monitored for correcting the refractive index [22]. Seven 61-pixel HPDs and one MAPMT were placed on a ring of radius 113 mm on the detector plate. An online display, obtained by integrating events in a run,

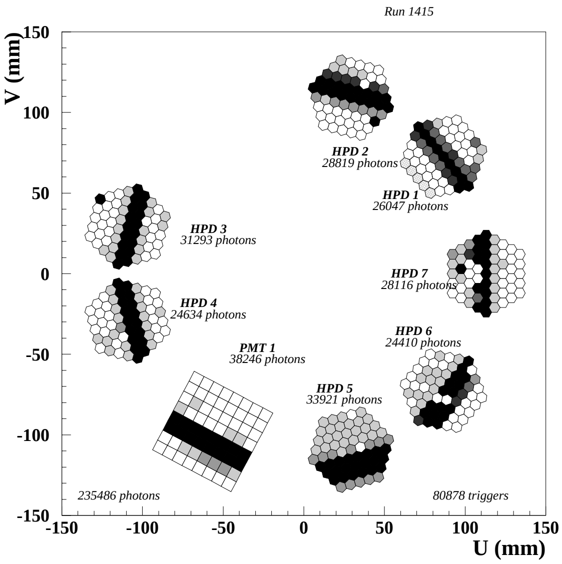

Figure 34: Display of events in a run using CF_4 in the RICH 2 prototype. For clarity the photodetectors are magnified. In this picture, the shade of a pixel gets darker with the number of hits on the pixel.

is shown in Fig. 34. The Cherenkov ring falling on the photodetectors is clearly visible.

The number of photoelectrons per event has been measured by the same method described above, with and without Pyrex filters on the front face of the photodetectors (Pyrex transmits wavelengths above ∼300 nm). The results obtained for the photoelectron multiplicities after correcting for background and signal loss are summarized in Table 6. It can be seen that there is excellent agreement between data and Monte Carlo.

	Pyrex Filter	No Filter
Data	0.29 ± 0.01	0.86 ± 0.03
Simulation	0.31	0.86

Table 6: The average photoelectron yield per event per detector after corrections, for 120 GeV/c π^- using CF_4 radiator in the RICH 2 prototype.

Source	
Chromatic aberration	0.13
Emission point uncertainty	0.05
Finite pixel size	0.13
Beam angle	0.06
Alignment	0.08
Total predicted	0.21
Observed	0.26

Table 7: Resolution components in mrad in the single photon Cherenkov angle distributions (with Pyrex filter) for 120 GeV/c π^- using CF_4 radiator in the RICH 2 prototype.

The Cherenkov angle resolution using the CF_4 radiator was also measured. The sources of uncertainty in the Cherenkov angle, described above, were included in the simulation. The resolutions from each component are shown in Table 7. Reasonable agreement is observed. The expectation from the LHCb Technical proposal [1] is for a RICH 2 angle resolution of 0.35 mrad. Although the observed resolution of 0.26 mrad cannot be compared directly because of non-identical operating conditions and geometry, the required resolution has nevertheless been achieved.

Figure 35 shows a plot of the the mean Cherenkov angle calculated from the hits in the seven 61-pixel HPDs, where the beam was a mixture of kaons and pions, approximately in the ratio 1:9, at 50 GeV/c. Although the geometrical coverage provided by the photodetectors in this test is approximately one quarter of what will be provided in the LHCb RICH 2 detector, clear peaks corresponding to the two charged particle types can be seen in the figure.

Aerogel studies

Independent laboratory and beam tests have been carried out to evaluate the performance of a variety of aerogel samples.

The optical properties of aerogel have been tested in the laboratory, by measuring the light transmission, T, as a function of wavelength and of aerogel thickness. Two samples were tested, one produced by Matsushita and the other produced by Novosibirsk [25]. For a 2 cm-thick tile it was found that, at 600 nm, T=65% in the case of the hydrophobic aerogel produced by Matsushita, and T=82% for

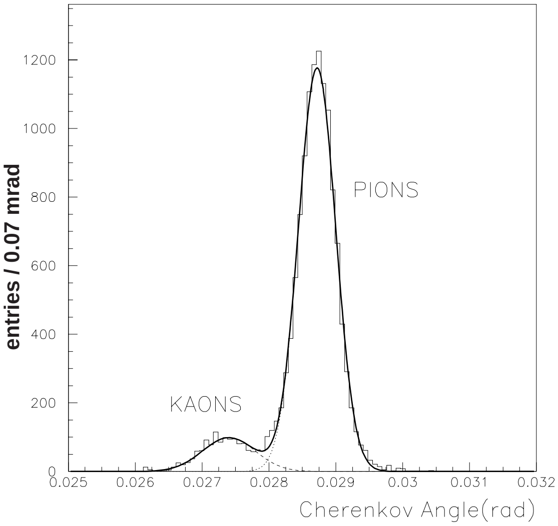

Figure 35: The mean Cherenkov angle from the 61-pixel HPDs without pyrex filter. CF_4 radiator was used in the RICH 2 prototype, where the beam was a mixture of kaons and pions at 50 GeV/c.

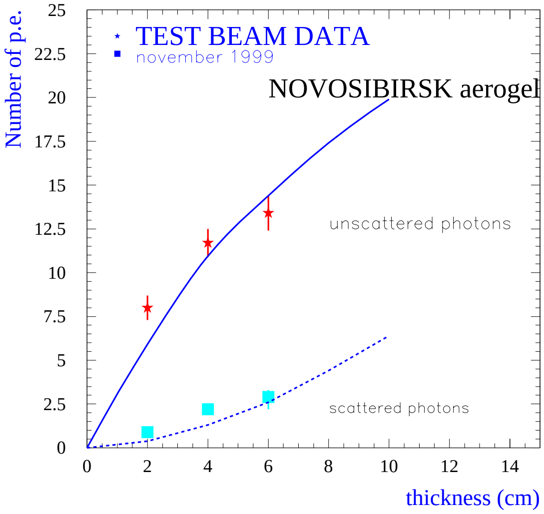

Figure 36: Photon yields in Aerogel, compared with simulation.

the same thickness of hygroscopic aerogel produced at Novosibirsk.

Samples of aerogel of different thickness and optical properties were exposed to pion and proton beams with momenta between 6 and 10 GeV/c in the T7 PS testbeam at CERN. The number of photoelectrons and the radius of the Cherenkov rings were measured in order to determine the performance of proton/pion separation.

Tiles of dimension $55{\times}55{\times}10\,\mathrm{mm}^3$, (cut from the original ones of $110{\times}110{\times}10\,\mathrm{mm}^3$) produced by Matsushita, and $100{\times}100{\times}20\,\mathrm{mm}^3$, produced in Novosibirsk, were exposed to the beam [26]. The Cherenkov photons were detected by two large diameter Pad HPDs with 2048 channels [24] positioned in the focal plane of the mirror. These provided a geometrical coverage of about 1/5 of the total ring. Data were taken with thicknesses of the aerogel radiator varying between 2 and 6 cm, and also with a Mylar film interposed at the exit side of the aerogel in order to absorb photons above 3.1 eV. Photons above this energy are most affected by Rayleigh scattering.

The photoelectron counting was found to be in reasonable agreement with the Monte Carlo expectations for all the aerogel thicknesses, as shown in Fig. 36. A clarity coefficient $C = 0.005\,\mu\mathrm{m}^4/\mathrm{cm}$ and refractive index $n = 1.034$, were used in the simulation. With 6 cm of aerogel, the mean photoelectron yield, extrapolated to a full ring is 13.4, with the hygroscopic (Novosibirsk) aerogel (compare 6.6 in Table 1 for 5 cm of hydrophobic aerogel). Off-ring, a mean of 2.8 photoelectrons has been measured, extrapolated to a circular region centered on the Cherenkov ring and covering an area approximately twice that inscribed by the ring.

The Cherenkov angles, reconstructed from the photon hit coordinates, were measured at various momenta. Pion/proton separation was achieved at all beam momenta, as can be seen, for example, in Fig. 37. This shows the Cherenkov angles produced by 8 GeV/c pions and protons. The analysis of the test-beam data is still in progress.

From the preliminary analysis, it appears

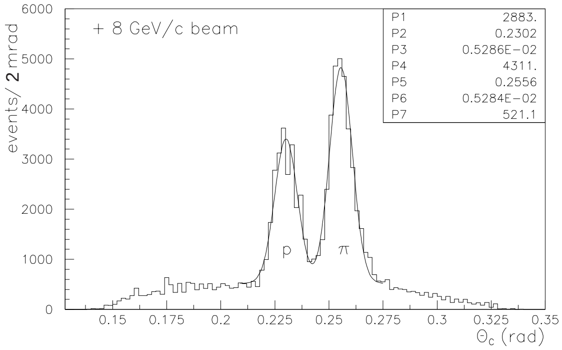

Figure 37: Cherenkov angles measured from the rings of pions and protons produced by an 8 GeV/c beam in Aerogel.

that the properties of the aerogel radiator provided by Novisibirsk are well suited to the needs of the LHCb RICH 1 detector.

4.3 Pixel HPD tests

From the performance studies of the earlier versions of cross-focused image intensifiers [27], it has been established that they can reach a spatial resolution of 10 μm and that the image distortions at the edge are below 10%, which can later be corrected for. Their electron optics is not perturbed by external electric fields and they can be shielded against low external magnetic fields [28].

As part of a staged R&D programme, two pixel HPD prototypes have been specially manufactured by DEP in collaboration with LHCb. The first is a half-scale prototype with a 2048 pixel anode. This tube provided a test of an HPD encapsulating a fine-grained pixel sensor. The second is a full-scale prototype with a 61-pixel anode. This tube provided a test of an HPD with the required electron optics. Studies with these prototype tubes are described in this section. The final prototype tube, a full-scale HPD encapsulating a fine-grain pixel sensor, is currently in production.

4.3.1 Electron Optics

The half-scale prototype HPD :
This HPD has electrostatic cross-focusing by which the image on the photocathode is demagnified by a factor of four at the anode. The operating voltage of is 20 kV, providing a gain of approximately 5000. The anode is an array of 2048 silicon pixels bump-bonded to an LHC1 [29] binary readout ASIC. The tube has a diode structure and the electrodes are designed to demagnify the 40 mm cathode diameter onto the 11 mm diagonal of the LHC1 chip. The tube has an active input window diameter of 40 mm and the silicon pixels are rectangles of size 0.05 mm × 0.5 mm. Details of this device and its readout can be found in [30]. It represents a half-scale prototype of a final tube which will have an 80 mm diameter input window and 1024 square pixels with 0.5 mm side.

The demagnification properties of the tube were measured [30] precisely using a red LED light source mounted on an $x-y$ translation stage, which scanned its full active diameter. From the binary signals produced by the silicon detector at the anode, the location of the photoelectron at the anode (r_a) was estimated as an average of the hit pixel positions recorded over several measurements.

The demagnification law was parametrized as $r_a = \alpha r_c + \beta r_c^2$, where r_c is the photoelectron location at the cathode, α is the linear component of demagnification and β is the non-linear component arising from the distortions at the edge of the tube. In this equation the origin is on the axis of the tube and the change in sign for the hit coordinates due to cross-focusing is not included. From the data, α and β were found to be 0.225 and $1.2\times10^{-3}\,\mathrm{mm}^{-1}$ respectively. This result was verified by simulating the electron optics using the POISSON program package [31, 32] to determine the voltage distribution in the tube and thus the trajectory of the photoelectrons, giving α and β to be 0.214 and $1.9\times10^{-3}\,\mathrm{mm}^{-1}$ respectively. These values are in agreement with the corresponding estimates from real data.

The full-scale prototype HPD :
Four full-scale prototype tubes with 72 mm active input diameter have been manufactured by DEP. These tubes were designed to have a nominal demagnification factor of 4 (72 mm to 18 mm). The input optical window of the tubes is made of quartz and the photocathode is a multi-alkali S20 type. The electron optics is based on a tetrode structure. One tube was equipped with a phosphor screen anode coupled to a CCD camera, and was used to verify the imaging properties and the electron optics behaviour in low magnetic fields. The pixel size of the CCD camera which viewed the phosphor screen ($11\,\mu\mathrm{m}\times 11\,\mu\mathrm{m}$) was small enough to allow characterization of the tube to a precision beyond that required for the LHCb granularity ($\sim 2.5\times 2.5\,\mathrm{mm}^2$). The photocathode quantum efficiency was measured at the DEP factory to be 19% at 400 nm. The tube was operated at 20 kV. The other three tubes were fitted with a 61-pixel silicon anode, identical to the sensor of the commercial DEP device described in Section 4.2.1. The sensor is segmented into hexagonally close-packed pixels that measure 2 mm between their parallel edges.

The demagnification of the 72:18 mm tube was measured [33] as described above. The full active diameter of the tube (75 mm if refraction at the input window is taken into account) was scanned by the LED, and the results are shown in Fig. 38. The experimental values have excellent agreement with the design curves, except at the outer diameter of the tube.

The values of α and β were found to be 0.216 and $0.7\times 10^{-3}\,\mathrm{mm}^{-1}$, respectively. In addition, the point spread function (PSF) of the tube, which shows how much the electron trajectories from a point source at the cathode would spread out when they arrive at the anode, was also estimated. The PSF from the LED data is calculated to be $\sim$33 μm on the tube axis and $\sim$54 μm at the edge, which is in reasonable agreement with the design values. The measured light spot standard deviation is shown as a function of photocathode radial coordinate in Fig. 39. Electron optics measurements performed on the three HPD tubes confirmed the above results [34, 35].

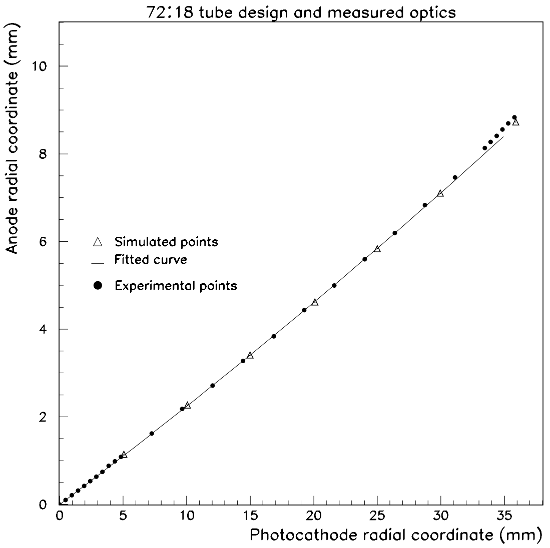

Figure 38: Measured de-magnification of the phosphor tube electron optics (black dots). The triangles and the full line refer to the design values.

4.3.2 Beam tests

The two types of pixel HPD described in Section 4.3.1 have been tested in the prototype RICH counters. Results are reported in Ref. [36, 34, 22]. The data used were collected during 1998 and 1999 at the CERN SPS facility; details of the test beam and experimental setup were given in Section 4.2 and in Ref. [21].

The half-scale prototype HPD :
For the half-scale 2048-pixel HPD, the RICH 1 [36] and RICH 2 [21] prototypes were used with an air radiator and 100 GeV/c π^- beam. The 2048-pixel HPD and three 61-pixel HPDs were placed on a ring of radius 90 mm on the detector plate. Pyrex filters were placed in front of the photodetectors in order to limit the transmission to longer wavelengths for some runs. A pixel threshold map was established on the 2048-pixel HPD using an LED [30]. For

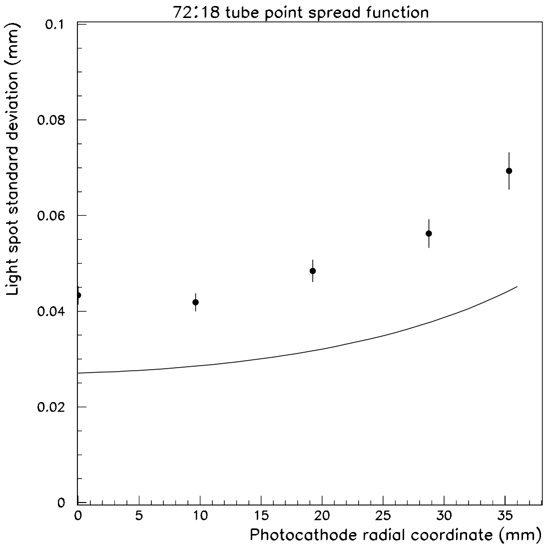

Figure 39: The measured light spot standard deviation as a function of photocathode radial coordinate (black dots). The solid line is the calculated contributions of the LED finite spot size and the CCD pixel size.

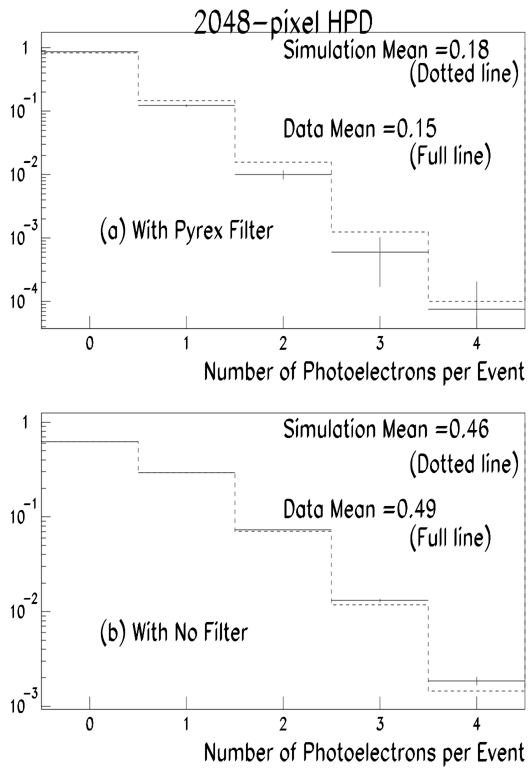

Figure 40: Number of photoelectrons per event in the 2048-pixel HPD (a) with pyrex filter in simulation and real data (b) with no filter in simulation and real data.

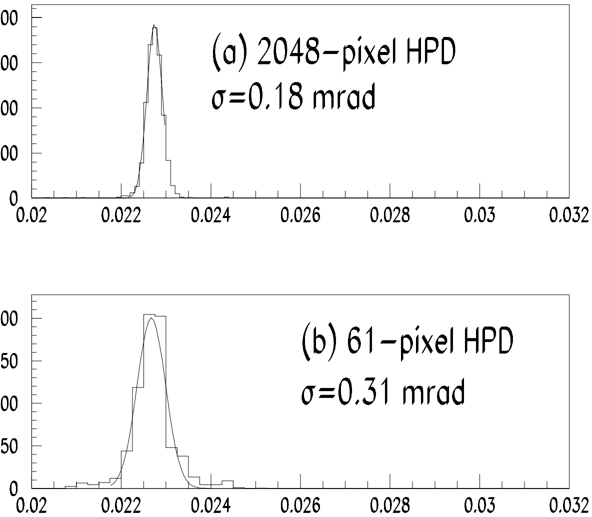

Figure 41: Cherenkov angle distribution for (a) 2048-pixel HPD and (b) 61-pixel HPD.

this, the high voltage applied on the tube was varied, and the voltage for each channel to become active was recorded.

The photoelectron yield from data and simulation in the presence and absence of a pyrex filter is shown in Fig. 40. Using the observed yields, the figure of merit is estimated to be $97 \pm 16\,\mathrm{cm}^{-1}$ in the case without the pyrex filter and $30 \pm 5\,\mathrm{cm}^{-1}$ in the case with the filter. The quantum efficiency of the photocathode of this tube was low, and substantial improvements (a factor of two) have been achieved with later devices.

Figures 41(a) and (b) show the reconstructed Cherenkov angle distribution from the pixel HPD obtained using an air radiator and pyrex filter, compared to a 61-pixel HPD which was diametrically opposite to it on the detector plate. The 2048-pixel HPD has a better resolution than the 61-pixel HPD since the pixel granularity along the ring is 0.2 mm for the former and is 2 mm for the latter.

The source of systematic uncertainty in

Source	
Chromatic aberration	0.15
Emission point uncertainty	0.05
Finite pixel size	0.02
Beam angle	0.06
Alignment	0.06
Total predicted	0.17
Observed	0.18

Table 8: Resolution components in mrad of the single photon Cherenkov angle distributions for the 2048-pixel HPD (with Pyrex filters) with a 120 GeV/c π^- beam.

the Cherenkov angle measurement from each component is tabulated in Table 8. In each case, the overall simulated resolution is in good agreement with that measured in the data. The required resolution for the LHCb RICH detectors is achieved with the 2048-pixel photodetector.

Figure 42 shows the Cherenkov angle distribution for the 2048-pixel HPD without pyrex filter where the beam used was a mixture of pions and electrons at 10.4 GeV/c. Good separation is obtained between the two particle types.

The full-scale prototype HPD :
To test the full-scale prototype tube, the RICH 1 prototype was operated with a ~1 m C_4F_{10} radiator at various pressures, with a 120 GeV/c π^- beam [34, 35]. The analogue readout system comprised a VA2 readout system [5]. Because of the coarse 61-pixel sensor granularity, the studies provide a valuable test of tube operational characteristics and photon yield, but not of the Cherenkov angle resolution. Figure 43 displays the events in a high pressure run where the Cherenkov ring spanned the three HPDs.

The signal and background in each pixel were determined from analysing the corresponding ADC spectra. The photon yields, obtained in low pressure runs where the Cherenkov ring was contained within a single HPD, are compared to detailed simulation in Table 9. Excellent agreement is observed. Using the observed yields, the figure of merit is estimated to be 202 ± 16 cm^{-1}. The Cherenkov

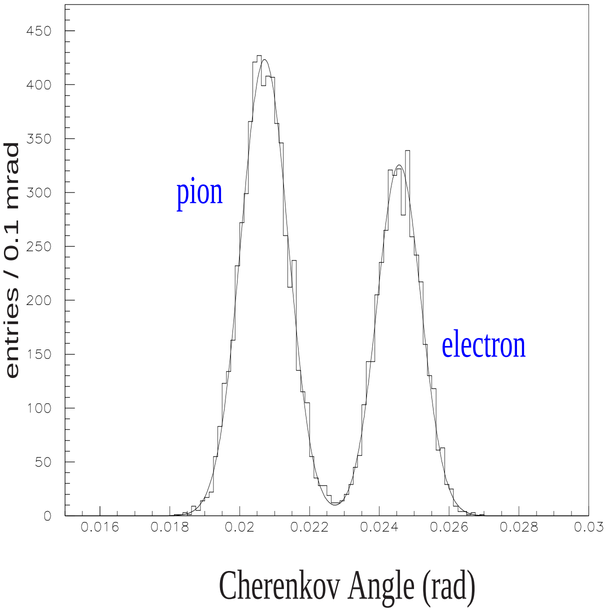

Figure 42: Single photon Cherenkov angle distribution for the 2048-pixel HPD without pyrex filter with an air radiator and using a 10.4 GeV/c beam composed of pions and electrons.

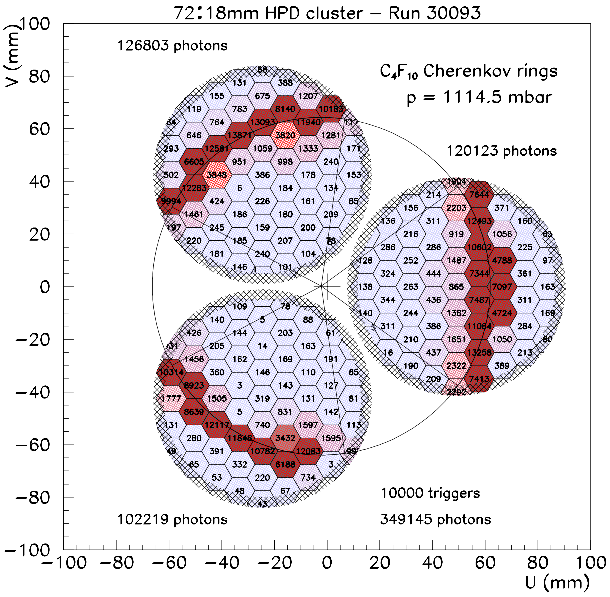

Figure 43: Display of events in a run where the ring covers the three HPDs. In the figure, the shade of a pixel gets darker with the number of hits on the pixel.

angle resolution also agrees with expectations.

Ring location	Yield per event	Simulated yield
HPD-1	8.50± 0.08	8.53 ± 0.61
HPD-2	7.27± 0.04	7.19 ± 0.56
HPD-3	7.37± 0.05	7.56 ± 0.62

Table 9: Photoelectron yield per event (after background subtraction) The background is estimated with a 4σ pedestal threshold cut.

4.3.3 Magnetic field tests

Magnetic field tests have been carried out on the full-scale HPD equipped with a phosphor screen anode. A small solenoid and a Helmholtz coil were used to provide fields up to 3 mT. The performance of the electron optics were studied and full details appear in a technical note [38]. A 200 mm long, 0.9 mm thick cylindrical Mu-metal shield was used. The shield extended 20 mm beyond the centre of the entrance window, resulting in minimal light shadowing of the photocathode. The shield attenuation and the image distortions of the shielded tube were measured in longitudinal and transverse fields of 1, 2 and 3 mT. In the case of a transverse field, a non-uniform image shift occurs, maximal at the tube axis and about 0.3 mm at 3 mT. In the case of a longitudinal field, image rotation and distortion occur. The effects are shown in Fig. 44. Important points to note are:

- The periphery of the image remains confined within the boundary of the silicon pixel detector (at 3 mT).
- The point spread function is barely affected.
- Image distortions can be corrected offline.

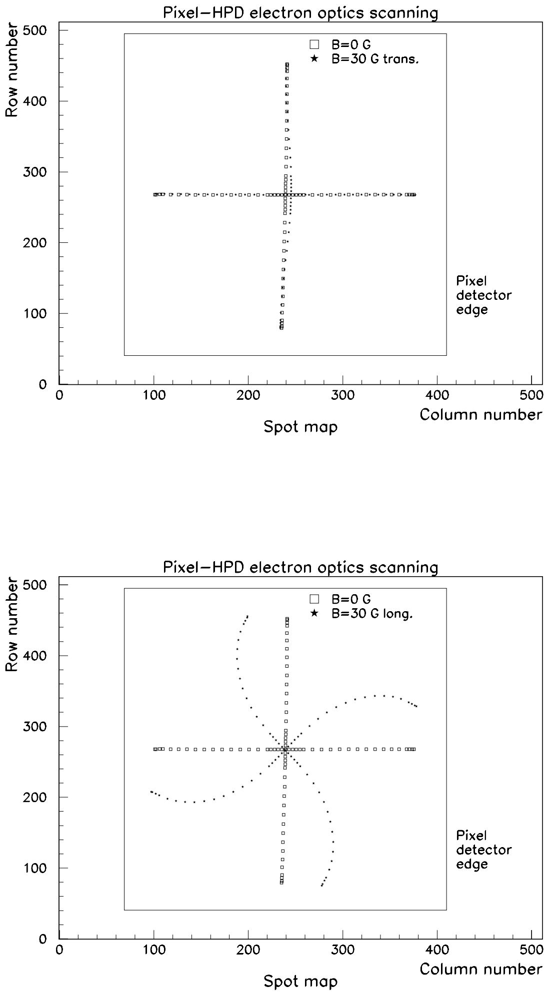

Figure 44: Displays of the image of a cross, seen on the phosphor anode. The image with and without magnetic field are superposed on each display. Top: Transverse field of 3 mT. Bottom: Longitudinal field of 3 mT.

4.3.4 HPD response to charged particles

When a charged particle traverses the quartz entrance window of an HPD from either its front or back face, Cherenkov light is produced along its trajectory. The Cherenkov photons can in principle make multiple internal reflections within the window, with a finite probability of an electron conversion every time the photon impinges on the inner (photocathode) surface. This effect can result in multiple spu-

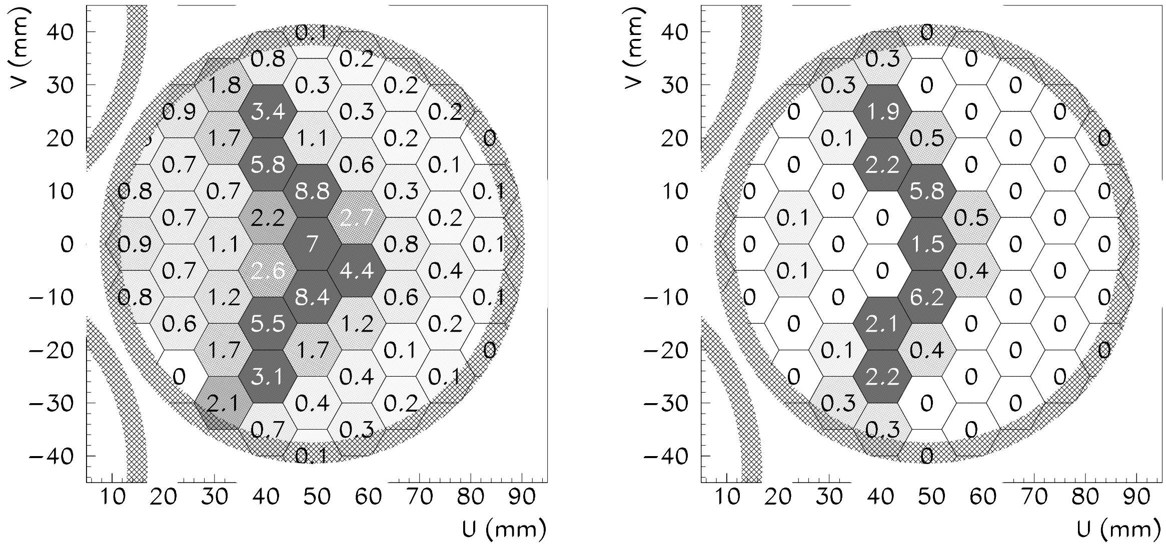

Figure 45: Displays of the average number of pixel hits in data (left) and in simulation (right), for 120 GeV/c charged pions passing at 135° to the HPD axis, ie. entering from the rear.

rious hits in the HPD, and render those pixels dead for genuine Cherenkov photons from the RICH radiators.

Beam tests have been performed to study the effect of charged particles [35] using the prototype 72 mm pixel HPD. The HPD has a 7 mm quartz window with 61 × 2.5 mm hexagonal pixels. The purpose of the study was to investigate the number of pixels firing as a function of beam incidence angle through the HPD window. The resulting patterns of hits are compared with Monte Carlo simulation. The coarse pixellation of the prototype HPD allows only a qualitative study to be made since the granularity of the final 1024-pixel device will have greatly improved photon counting capabilities.

A beam of 120 GeV/c pions was incident through the centre of the HPD window at five different angles : 0° (pions entering the HPD window normally from the front), 45°, 90°,135° and 180° (pions entering the HPD window from the rear). A comparison of data with the simulation for pions incident at an angle of 135° is shown in Fig. 45. Although more photons than predicted are seen in the data, good qualitative agreement is observed. Based on a pulse height analysis for photon counting, Table 10 summarises the comparison of data and Monte Carlo at the five angles of incidence. In all cases the event shapes are distinctive, and are in good agreement with simulation. It is expected that such characteristic patterns of hits can be searched for in data, and masked off when counting true Cherenkov hits. Importantly, a tube is not rendered completely dead due to the passage of a charged particle. Typically 25-35% of the tube must be masked off, a fraction which is angle dependent. Simulations have shown [10] that 10-15% of all hits in the RICH detectors will originate from these charged particle hits.

4.4 Testing the pixel chip

A prototype LHCb readout chip is being developed as a collaborative effort with the readout chip for the ALICE Inner Tracking system [37, 39]. Experience of operating and maintaining large numbers of pixel channels has been obtained with previous chips in heavy-ion experiments [29].

Angle	N_{obs}	N_{MC}
0°	≥138	172
45°	≥119	58
90°	≥258	273
135°	83	25
180°	168	129

Table 10: Numbers of photoelectrons per event in data and simulation for 120 GeV charged pions passing through the entrance window of the HPD.

Some of the requirements that the pixel chip must meet [5, 9] are:

- Peaking time at or below 25 ns for the front-end amplifier.
- Discriminator threshold below 2000 electrons with a pixel-to-pixel spread below 200 electrons.
- Radiation tolerance to an integrated 10 year dose of 30 kRad.

As described below, these goals have been already achieved with prototype chips. In the first of these chips [41], developed for X-ray photon imaging, the threshold of each pixel cell can be adjusted individually using a 3-bit register to reduce the channel-to-channel variation. This chip has been demonstrated to have a minimum threshold of 1400 electrons with an RMS spread of 80 electrons.

Another chip [42], developed with $0.5\,\mu$m commercial CMOS technology has a peaking time of 25 ns. The measured time-walk is less than 25 ns for signals that are 100 electrons above a typical threshold of 1650 electrons. In addition, the chip was found to be radiation tolerant up to 600 kRad.

Based on this design, a third chip [43] was developed with $0.25\,\mu$m commercial CMOS technology. It was demonstrated to have a minimum threshold of 1500 electrons and a threshold spread of 160 electrons. With an adjustment of individual pixel thresholds using the 3-bit register, this spread could be reduced to 25 electrons. For this chip the electronic noise was measured to be 220 electrons and the static power consumption per channel was $50\,\mu$W. It was also shown that this chip remains functional up to an X-ray dose of 30 MRad. A set of these chips were subjected to a bake-out at DEP, similar to that during the HPD manufacturing process, and the subsequent electronic tests [5] showed no degradation of the chip performance.

4.5 Mirrors

4.5.1 Test facility

Over the past two years, an optical laboratory has been set up at CERN. Its main task consists of studying, characterizing and qualifying optical elements for future RICH and other optically-based particle detectors. In the RICH project for the LHCb detector, the main optical elements are the mirrors and their mounts.

Mirror parameters are being partially determined on the basis of measurements on mirror prototypes [44]. Further, to ensure the required quality, mirror specifications have to be verified by measurements. It is planned to check the most critical specifications on all the mirrors, that is: visual inspection, to assess cracks, bubbles, etc., dimensions, average value of radius of curvature, R, average angular resolution, and average reflectivity.

Mirror mount prototypes have to be characterized in their adjusting precision and stability [45, 46]. Long-term stability is a very critical parameter. It is important to keep the variations well below what will be required by the off-line alignment procedure. We aim at a stability in the range of $\sigma < 0.1$ mrad. The issue of possible radiation damage on components has also to be addressed.

To carry out the aforementioned checks, three benches have been set-up and two more are being assembled. Special attention has been paid to automate the setups as much as possible, in order to minimize operator manipulation and to increase reliability.

4.5.2 Mirror quality

Each spherical mirror will be tested for its radius of curvature and average angular precision before installation inside the RICH vessel. The setup measures the variation from the ideal mirror spherical surface by imaging a point source reflected from the sample mirror and by analyzing the size and shape of the resulting focal spot. Thus, it provides a direct measurement of R and the average angular precision σ_θ [44].

By measuring a sample of mirrors, we will obtain a distribution in R. For RICH 2, its standard deviation should not exceed

$$\sigma_R = \frac{\sigma_d}{r_c - \sigma_d} \sim 1.0\% \text{ of } R,$$

where σ_d is the photodetector precision and r_c the Cherenkov cone base radius.

If the mirror had a perfect spherical surface, the spot on the focal plane should have the same dimensions as the point source, as the measurement is intrinsically spherical aberration-free. However, geometrical distortions can be present for mirrors with large surfaces ($\geq$0.10 m^2) and thin substrates ($\leq$ 7 mm). These distortions should be distinguished from polishing imperfections, which greatly depend on the hardness of the substrate and also generate poor optical quality. The net result is an enlargement of the focal spot with the presence of irregularities on the borders. We will therefore define that a circle in the focal plane which contains 95% of the reflected light has a diameter $D_0 = 4\sigma_s$ where σ_s is the RMS of the spot size.

We have tested 40 RICH mirror prototypes and provided feedback to the mirror manufacturers. In Fig. 46, the fraction of reflected light falling into circles of different diameters for a mirror prototype is shown. In Fig. 47, the diameter D_0 of the light spot is shown as a function of the distance d of the light spot from the mirror surface for different light fractions inside the circle [44]. These measurements permit the precise calculation of R and σ_θ, which are equal to 6644 mm and to 0.026 mrad respectively for this mirror.

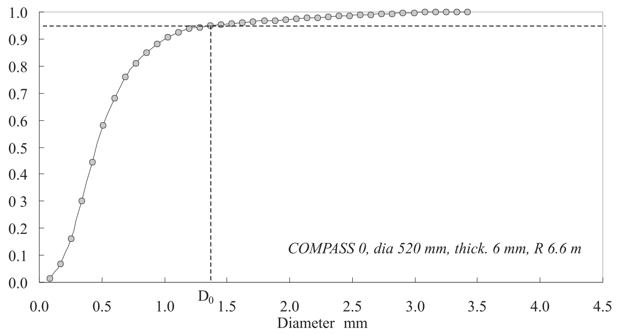

Figure 46: Light fraction inside circles of different diameters. Shown is the corresponding D_0.

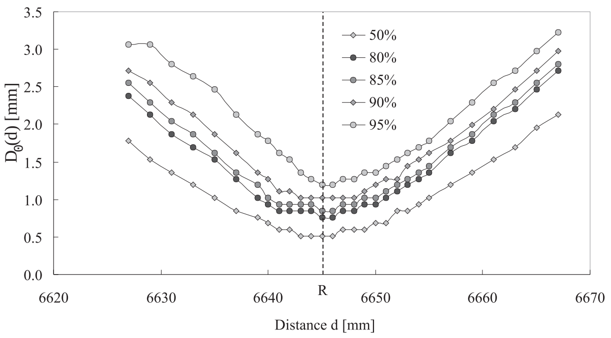

Figure 47: Spot size as a function of distance d for a COMPASS mirror. This demonstrates the procedure for finding the radius of curvature.

Mirror quality has been improving with time and the measurements performed allow us to conclude that mirrors with a Simax glass substrate, a thickness of 6 to 7 mm, a radius of curvature of 8 m and a diameter up to ∼500 mm are feasible with the geometrical requirement of $\sigma_\theta = 0.03$ mrad. That is, they are capable of focussing 95% of the reflected light into a circle with diameter $D_0 = 2$ mm at the plane defined by the mirror radius of curvature $R = 8$ m. Finally, two effects on the mirror geometrical quality have yet to be carefully analyzed: the influence of the final mirror mount and the mirror long-term behaviour.

Spectral reflectivity is another parameter that is measured in the CERN optical laboratory to qualify RICH mirrors. In order to minimize mirror manipulation, we incorporate the reflectivity measurement into the same bench as for the previous set-up. It makes use of a hand-held spectrophotometer and it enables us

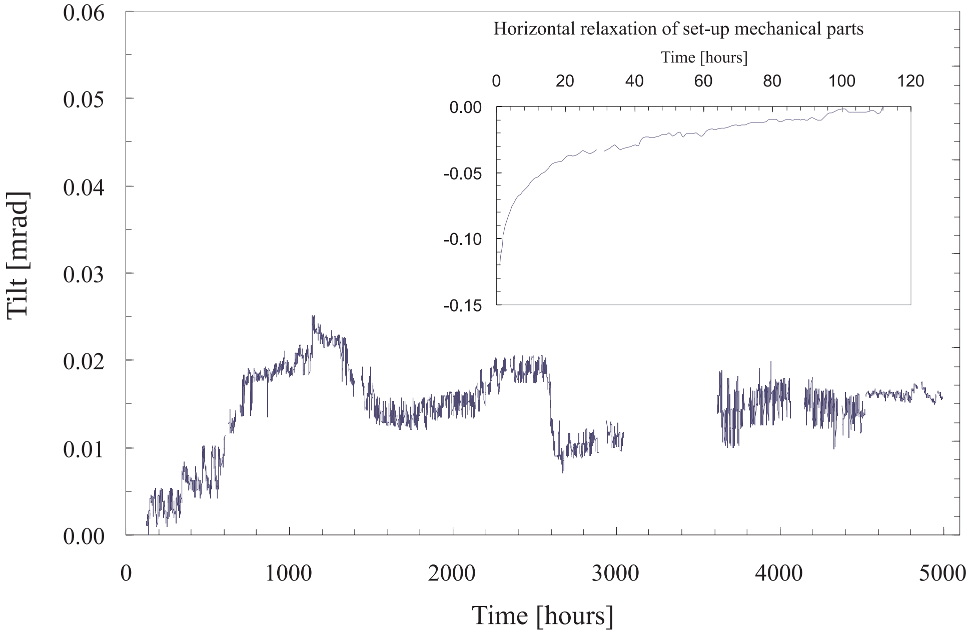

Figure 48: Mirror support horizontal tilt (arbitary zero). Shown in the insert is the strong mechanical relaxation observed at the start of the measurement.

to measure in the wavelength range from 200 to 850 nm.

4.5.3 Mirror supports

Two set-ups for the evaluation of the adjustment characteristics and the long-term stability of mirror mounts were developed. The detailed principles and results can be found in [45, 46]. A few mount prototypes have been tested and in particular the one retained for RICH 2, which is based on the membrane principle and it is exclusively made out of Polycarbonate material [45]. In Fig. 48, its long term stability is shown by means of the monitoring of its tilt chart during over 5000 hours. The vertical and horizontal tilts stay well into the 0.03 mrad required. However, the 1.7 kg weight loaded on the mount simulates a smaller mirror than that foreseen for RICH 2, therefore a measurement with a heavier weight has started.

The mount alignment precision is shown in Fig. 49 [46]. The adjustment range is 3 mrad, which should be sufficient for the machined mounting holes in the supporting structure. A tilt change of 0.1 mrad corresponds to a screw turn of 36°, which enables a sufficiently precise adjustment. The relationship between tilt and screw-turn is nearly linear[4]. The RMS of the parasitic coupling, crosstalk between the horizontal and the vertical movement, was less than 0.01 mrad.

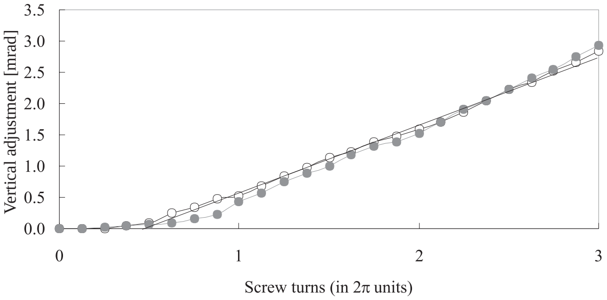

Figure 49: Results from the mount prototype. The measurement was repeated twice. A linear fit to the measurement is shown.

---

[4] The screw used had a pitch of 0.7 mm, that means a displacement of the wedge of 0.0875 mm for 45° turn.

5 Technical Design

5.1 Pixel HPD Photon Detector

The photodetector planes of the RICH detectors cover a total area of 2.6 m^2 over which it is necessary to detect single photons with a high efficiency and with spatial granularity of about 2.5 mm×2.5 mm. The photodetectors need to be sensitive to Cherenkov light at visible and UV wavelengths and readout must be fast, compatible with the 25 ns time between LHC bunch crossings and the overall LHCb readout scheme [8]. The photodetectors will be situated in the fringe field of the spectrometer magnet and will experience a radiation dose of up to 3 kRad/year.

The baseline photodetector technology selected for the LHCb RICH is the Pixel hybrid photon detector (HPD) which uses a silicon detector anode inside the vacuum envelope. Photoelectons released by photons incident on the photocathode are accelerated onto the silicon sensor by an applied high voltage $\sim$ 20 kV, resulting in a signal $\sim$ 5000 e in the silicon. This device, shown schematically in Fig. 9, has been developed commercially, in a long-standing collaboration with DEP. It is based on an image intensifier technology, employing electrostatic cross-focussing to accelerate and image photoelectrons from the photocathode onto the anode, demagnifying by a factor $\sim$ 5. The anode assembly comprises a segmented silicon pixel sensor which is bump-bonded to a pixel readout chip. This assembly is encapsulated within the vacuum tube and must be compatible with the bake-out and other features of the vacuum tube and photocathode deposition process. During LHCb operation at nominal luminosity the channel occupancy of the photodetectors due to Cherenkov photons is typically 1%, and the probability of multi-photon hits is low. This has permitted the use of a binary readout scheme, with consequent low power consumption and simplifications in the electronics chain between detector and DAQ.

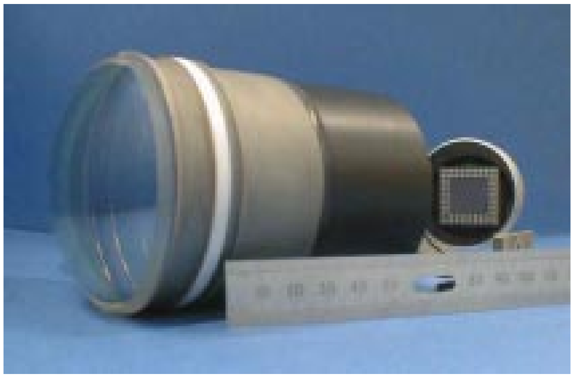

Figure 50: A prototype 80 mm HPD, produced by DEP. The 61-pixel PGA is seen reflected by a mirror placed behind the tube.

As described in Sections 4.2–4.4, all features of this pixel HPD have been tested in prototypes. Full-scale devices with external readout electronics (see Fig. 50) have been used to verify the electron optics and to measure the detected photon yield from Cherenkov light produced by charged particle beams. A half-scale device, with encapsulated pixel electronics has similarly been used to detect Cherenkov rings in a test beam. The current schedule for the development project foresees an LHC-speed pixel readout chip in operation before end 2000. This will be encapsulated in a full-scale HPD. Rigorous performance criteria have been defined as a milestone for this HPD; they require >85% efficiency for detection of a photoelectron in operational channels, with 95% of channels satisfying this criterion. In addition, the threshold set to detect a photoelectron signal is required to satisfy the following: signal/threshold >2.5, and threshold/noise >6. The schedule for this milestone is discussed in Section 6. The implementation of an alternative, backup photodetector technology using commercial metal channel multi-

Table 11: Measured quantum efficiency (Q) at given wavelengths λ for a thin-S20 multi-alkali photocathode deposited on a 7 mm-thick quartz window.

λ (nm)	200	240	270	400	600
Q (%)	10.2	22.0	25.7	19.3	4.3

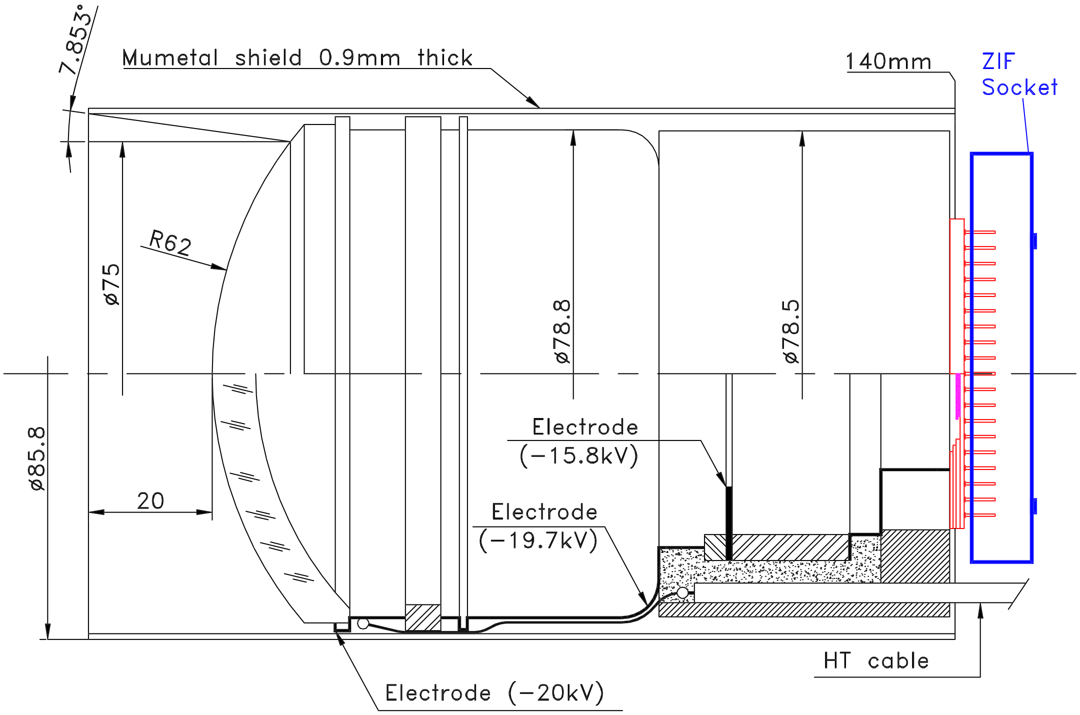

Figure 51: Outline drawing of the Pixel HPD and its magnetic shield.

anode photomultipliers (Hamamatsu R7600-03-M64 MAPMT), equipped with hemispherical quartz lenses to increase the active area, is described in Appendix A.

Technical details of the Pixel HPD and its readout electronics are summarized in the following sections. More details on the Pixel HPD [5], the readout chip [9] and the MAPMT [6] can be found in LHCb notes.

5.1.1 Vacuum tube and electron optics

The vacuum tube is assembled from metal (kovar) and ceramic sections as shown in Fig 51. The entrance window is made from 7 mm-thick quartz. It is spherical in shape and has a thin-S20 multi-alkali photocathode deposited on its inner surface. The quantum efficiency (Q) was measured on a prototype tube and values are listed in Table 11, and result in an energy integrated efficiency $\int Q\,dE = 0.77\,\text{eV}$. Cherenkov photons can be detected over an active diameter of 75 mm and the overall diameter is 83 mm, resulting in an active area fraction of 0.82.

Photoelectrons are focussed using the tetrode structure shown in Fig. 51. The nominal voltage at the photocathode is −20 kV. A 300 V potential difference between the photocathode and first electrode defines the magnification. The radial coordinate r_a (expressed in mm) at the anode is related to the coordinate at the cathode window, r_c by

$$r_\mathrm{a} = 0.200 r_\mathrm{c} - (4 \times 10^{-4}) r_\mathrm{c}^2 \ .$$

Taking into account the lensing effect of the entrance window the 0.5 mm square anode pixels correspond to 2.62 mm on the tube axis and 2.82 mm at the periphery. The RMS point spread function is approximately constant over the entrance window and equal to 0.4 mm.

The performance of the electron optics was measured using a full-scale prototype tube equipped with a phosphor anode coupled to a CCD. These measurements were described

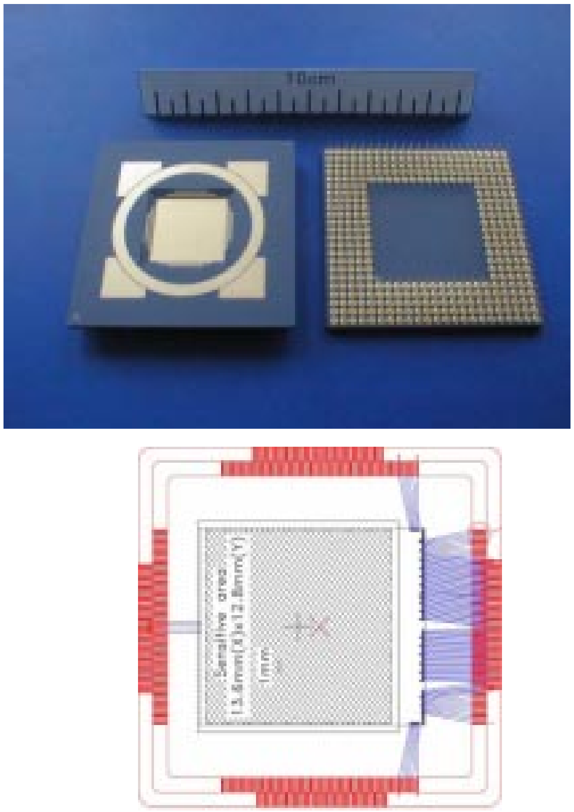

Figure 52: Top: Photograph of the ceramic PGA carrier. Bottom: the pixel chip wire-bonded to the carrier.

in Section 4.3.1; the effects of magnetic fields were also studied and reported in Section 4.3.3. Fringe fields up to 3 mT are expected at the location of the HPDs in RICH 1. In RICH 2 the fringe fields are stronger and will be attenuated by large soft iron enclosures, but the HPDs still require local magnetic shielding. This local magnetic shielding is provided by 0.9 mm thick Mu-metal cylinders, 86 mm in diameter and 140 mm long. In order to shield effectively they extend 20 mm beyond the photocathode. The shield is shown in Fig. 51 and is insulated electrically from the tube.

5.1.2 Anode assembly

The 20 kV photoelectrons strike the back surface of a silicon pixel sensor. To minimize the energy lost by photoelectrons in the (insensitive) n^+ layer at the sensor surface, the back (ohmic) side is formed by a thin 150 nm n^+ implant, a standard fabrication option offered by the manufacturer, Canberra[5]. The sensor is segmented into small reverse-biased diode pixels with dimensions $50\,\mu\text{m}\times 500\,\mu\text{m}$, arranged as a matrix of 320×32. Each pixel is connected via a solder-bump bond to a readout cell with matching dimensions on the front-end pixel readout chip. The readout chip, with bonded sensor, is mounted and gold-wire bonded to a ceramic pin grid array (PGA), manufactured by the Kyocera[6] company and proven to be compatible with the HPD manufacturing process. A photograph of the PGA carrier designed to encapsulate the ALICE-LHCb pixel chip is shown in Fig. 52.

5.1.3 Pixel chip

The binary readout chip [9] must satisfy the following requirements. It must discriminate single photoelectron hits with high efficiency and time-tag them with the LHC bunch crossing. This implies a front-end amplifier shaping time < 25 ns and a discriminator threshold < 2000 e with pixel-to-pixel spread of < 200 e. This value of the threshold allows detection of single photoelectrons that experience charge sharing among neighbouring pixels. Secondly, the characteristics of LHCb operation place demands on the digital circuits which store the discriminated hits. Single event occupancies up to 8% (corresponding to a time-averaged occupancy of 4% when including beam crossings with 0,1,2...interactions), a 1 MHz mean Level-0 trigger rate and a long ($4\,\mu$s) Level-0 latency require the storage of large numbers of hits for long periods, and the ability to transfer data at high rate to avoid dead time losses. The requirements are summarized in Table 12. With these specifications the photoelectron detection efficiency, taking into account the 18% backscattering probability, is expected to reach 90%.

The LHCb pixel chip comprises super-pixels (corresponding to one channel) of

---

[5] Canberra Semiconductors N.V. Belgium.

[6] Kyocera Corporation, Japan.

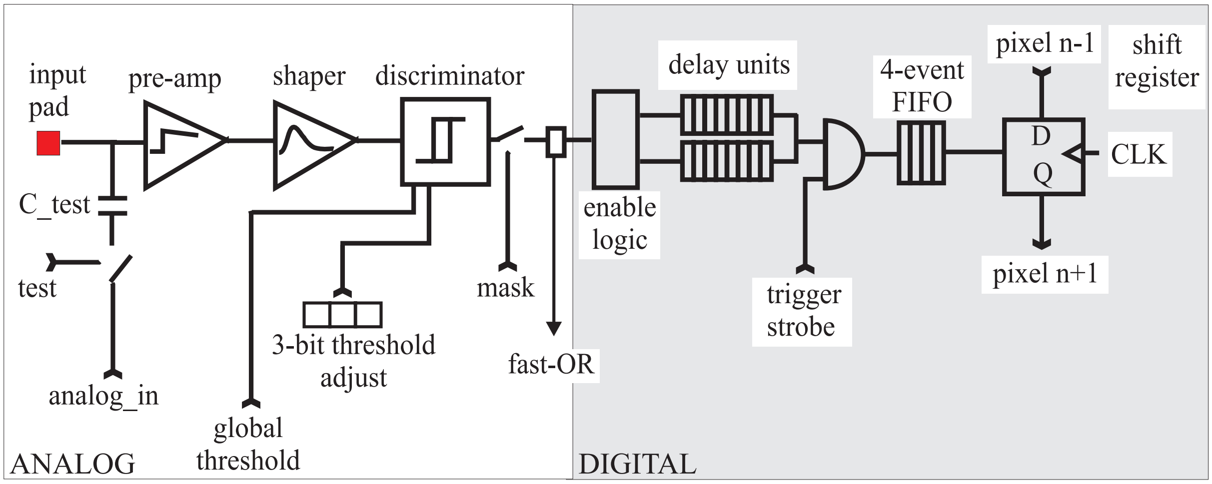

Figure 53: Schematic of the Pixel cell architecture.

Table 12: Specifications for the RICH binary Level-0 electronics

Operational threshold	< 2000 e
Dynamic range	Linear between 0—5000 e, with recovery for large signals
Max. noise occupancy	1%
Time resolution	25 ns
Channel size	500 μm×500 μm
Maximum time-averaged pixel occupancy	4%
Bunch crossing rate	40.08 MHz
Average L-0 trigger rate	1 MHz
Level-0 latency	4 μs
L-0 derandomizer depth	16
Max. readout time	900 ns
Rad. dose in 10 years	30kRad

500 μm×500 μm, arranged as a matrix of 32 × 32. Each super-pixel will be sub-divided into 10 pixel cells of 50 μm×500 μm. This arrangement of small pixel cells reduces the input capacitance and the cell occupancy seen by each analogue input. The schematic circuit of each cell is shown in Fig. 53 and includes a differential pre-amplifier (250 e RMS noise) and shaper (25 ns) followed by discriminator (3-bit threshold adjustment). Discriminator outputs from 10 pixels will be ORed to enable one of 20 delay units, whose delay can be set to match the trigger latency. Thus a maximum of 20 hits can be stored at any one time in one channel. Following the Level-0 trigger, data are stored in a FIFO buffer with capacity for 16 events. The four 4-event FIFOs of the topmost pixels within a super-pixel are configured together to form this 16-deep buffer. The main task of this FIFO is to de-randomize the data after the Level-0 accept. This architecture allows the data from each chip to be read out in < 900 ns; (32 rows ×25 ns + headers) through 32 parallel lines at 40 MHz, thus ensuring that dead time losses in the DAQ are maintained below 1%.

The chip is fabricated in 0.25 μm CMOS technology using a layout adapted for tolerance to ionising radiation and single event upset. The total power consumption of the 10,240 cell chip is ~ 0.5 W.

The current development of the chip [40] has 8192 pixel cells and combines both ALICE and LHCb functionality. In ALICE mode the matrix of 256×32 cells is read out as individual cells, whereas in LHCb mode, 8 cells are ORed to form a super-pixel. The ALICE-LHCb chip will be delivered to CERN in September and tested during October. It will then be mounted with the silicon sensor into the PGA carrier and encapsulated into an HPD. Only minor modifications to this chip are required to meet fully the LHCb specifications. These include:

- Increasing cell matrix to 320 × 32 with 10 cells ORed in a super-pixel: It is desirable to increase the size of a super-pixel from $425\,\mu\mathrm{m}\times400\,\mu\mathrm{m}$ to $500\,\mu\mathrm{m}\times500\,\mu\mathrm{m}$. The increase from $425\,\mu$m to $500\,\mu$m in the x-direction requires a simple spacing of the input columns and end-of-column logic. In the y-direction, one option is to add a further two $50\,\mu$m pixel cells within a super-pixel. This will provide four further delay units to store hits and is the optimum in terms of performance. Another possible solution, which involves fewer modifications to the current design, would be to maintain eight cells per super-pixel and increase the pixel front-end (and the sensor) pitch to $62.5\,\mu$m. This does, however, restrict the number of delay units to 16, and simulations are underway to assess the implications, given the estimated occupancies. All the modifications described above may require re-sizing of the buffers which drive the control signals across the chip and up the pixel columns. Measurements of the ALICE/LHCb chip will provide data on this issue.
- Logic to monitor FIFO and prevent overflow: The current ALICE/LHCb chip relies on external logic to monitor the content of the FIFO buffers. This will be included in the final version to prevent overflow of the buffers and control the readout when events are available.
- Logic to attach bunch-crossing tag to data packet: To ensure correct synchronisation between the Level-0 electronics and the Level-1 boards $\sim$100 m away, a header will be added to the data packet. This will take the form of a 12-bit bunch crossing number, stored on the arrival of the corresponding Level-0 trigger for each accepted event. A 12-bit counter will be implemented on the chip to generate this number.
- Addition of four on-chip DACs to provide bias voltages: The ALICE/LHCb chip requires the magnitude of the front-end calibration pulses to be set by external DACs. For accurate determination of the noise and threshold dispersion, the precision and range of these signals are such that 12-bits are needed. A design for an 8-bit DAC has been implemented into the current chip, and it is planned to use two such DACs to provide the 12-bit range and precision. By modifying the output stages of the DACs, one will set a coarse control, and the other a fine control.

The possibility of implementing the additional logic and DACs in a separate PILOT chip, external to the HPD, as described in Section 5.2, is under investigation. This has advantages for the timescale and allows flexibility in system integration.

5.1.4 Integration

The photodetector arrays will be constructed from hexagonal close-packing of the HPDs, including their Mu-metal magnetic shields. The packing pitch is 87 mm, resulting in an active-to-total area fraction of 0.67. A total of 430 HPDs is required, 168 for RICH 1 and 262 for RICH 2. Each pair of HPDs is connected via its PGA to a Level-0 interface board from which optical fibre links transmit binary signals to the Level-1 electronics in the counting room. Configuration of the encapsulated pixel chips is provided via a JTAG interface which is serviced by the LHCb Experiment Control System (ECS).

The high voltages for the photocathode and focussing electrodes are provided from a low-ripple supply with a $250\,\mathrm{M}\Omega$ voltage divider. The bleeder current of $80\,\mu$A exceeds the average photocathode current by at least 10^4. For redundancy each column of HPDs in RICH 1 and each half column (maximum of

8) in RICH 2 has its own HV supply and bias voltage for the silicon sensors.

Further details of the off-detector readout electronics and the photodetector mounting are included in Sections 5.2—5.4.

5.2 Readout electronics

5.2.1 Overview

The RICH readout system has the following major components :

- The first stage of readout is the binary front-end pixel chip, encapsulated inside the Pixel HPD vacuum envelope, and described in Section 5.1.3.

- Each pair of pixel chips is connected via the HPD pin grid arrays to a "Level-0 Adapter Board", mounted on-detector. The adapter board further multiplexes the data, drives optical data links to the off-detector (Level-1) electronics, and distributes clocks and triggers to the front-end chips. The binary pixel chip and the adapter board are together referred to as the "Level-0" electronics.

- The "Level-1 Readout Board" is located ∼100 m away from the detector in the counting room. This board receives the multiplexed data from the adapter boards via the optical links, it buffers and processes the data, and transports the data to the LHCb DAQ system.

A schematic of the LHCb readout architecture is shown in Fig. 54. Tables 13 and 14 give a summary of the total number of units in the system and the Level-0 and Level-1 parameters, respectively. These tables will be referred to in the following sections.

The design philosophy of the RICH readout has been to avoid building customised electronics where suitable commercial and/or general-purpose devices are available, except where a significant gain in simplicity or cost saving can be achieved. The Level-1 electronics have higher complexity and have therefore been moved away from regions of high radiation dose into the LHCb counting room. This eases accessibility for maintenance, and eliminates problems of radiation damage and single event upsets (SEU's). It also facilitates the use of radiation-soft Field-Programmable Gate Arrays (FPGA's).

LHCb will use the RD12-developed Timing, Trigger and Control Receiver ASIC (TTCrx) [47] to synchronize the front-end electronics to the rest of the LHCb sub-detectors and for the local distribution of the clocks and triggers. Downloading configurations to the pixel chip and the adapter board is provided by a JTAG interface [48] which allows read and write access to all registers. The JTAG interface is serviced via the Experimental Control System (ECS) [49]. The RICH detectors do not contribute to the Level-0 or Level-1 trigger decision.

The readout system is designed to allow efficient stand-alone running, calibration, monitoring and debugging. These features, together with a full description of the RICH readout system, are described in Ref. [50].

5.2.2 The Level-0 Adapter Board

The first stage of readout is the binary pixel chip, described in Section 5.1.3. On a Level-0 trigger accept, the data from a pair of pixel chips are multiplexed out at a 40 MHz rate as two 32-bit streams to the Level-0 adapter board. The multiplex grouping of 32 is chosen to match the maximum average LHCb Level-0 trigger rate of 1 MHz. There are 84 and 136 adapter boards for RICH 1 and RICH 2, respectively (one for each pair of HPD's, and five extra for RICH 2 in order to read out single HPD's in odd-numbered columns).

The Level-0 adapter board is shown schematically in Fig. 55. The main functions are:

1. To provide a further multiplex stage for the data from the Pixel HPD's and to drive the data via optical links to the Level-1 electronics. G-Link protocol is a candidate technology.

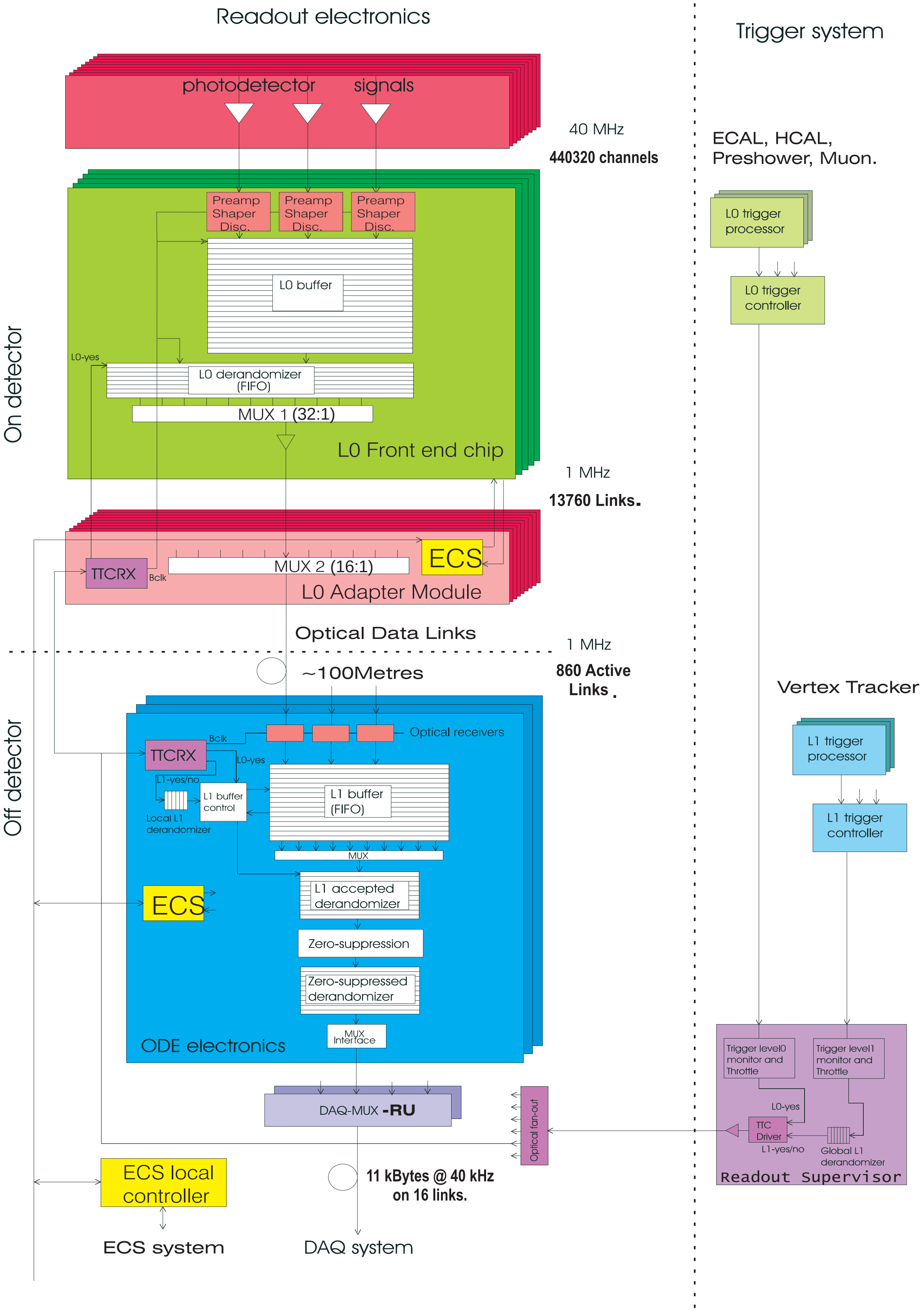

Figure 54: A schematic of the LHCb RICH readout architecture.

Item	RICH1	RICH2	Total
HPD's	168	262	430
Readout channels	172032	268288	440320
HPD adapter boards	84	136	220
G-Link transmitters	336	524	860
TTCrx & ECS interface	84	136	220
Level-1 boards	21	33	54
G-Link receivers	378	594	972
TTCrx & ECS interface	21	33	54
FPGA's	210	330	540
SLink drivers	21	33	54
Crates & power supplies	2	2	4

Table 13: The total number of units (excluding spares).

2. To receive, phase and fan-out the clocks and triggers via the TTC.
3. To receive and distribute the LHCb ECS commands to the binary chips.
4. To receive, regulate and distribute the various local low-voltage power to the binary chip.

The Level-0 Adapter Board provides a second level of multiplexing of the data of 16:1, which matches the bandwidth of the optical fibre links to the Level-1 electronics (∼1.0 Gbits/s). This second multiplexing stage is necessary to minimize the number of optical links, and hence the cost. The time available for reading out the data from the Level-0 into the Level-1 boards is 900 ns, determined by the average Level-0 accept rate of 1 MHz, with 100 ns contingency.

Referring to Fig. 55, the "PILOT" chip [51] is used to control the readout of the pixel chip, to interface between the pixel chip and the G-Link and serialiser ASIC, and to provide JTAG distribution. The PILOT, G-Link and serialiser chips are active design projects [52, 53]. Settings and configuration values of the pixel chip – the shaping current, the bias currents, the discriminator values, the masking, the output multiplex grouping, the pixel grouping, the running mode and the calibration values – will be downloaded to the binary chip via the ECS. The ECS will also monitor and report error states of all components.

Since the Level-0 Adapter module is located on-detector and in a hostile environment, radiation-tolerant components will be required. The expected maximum charged particle radiation level in the RICH electronics region is ∼30 kRad per ten years. The rate of SEU's is expected to be low enough that automated detection and recovery will be effective, and flagged and reported through the ECS.

5.2.3 Multiplexing and Data Links

The data links from the Level-0 to the Level-1 will be fibre optics of length ∼100 m. The data will be serialised at Level-0, transmitted at ∼1.0 Gbits/s, received by commercial G-Link receivers at Level-1, deserialised, and phase-aligned to the TTC clock. The total number of data fibres from the two RICH detectors will be 860.

5.2.4 Level-1 Electronics

The Level-1 module performs the following functions :

Level-0 ASIC parameters	
Number of pixel channels per HPD	1024
Number of bits per digitised detector channel	1
Maximum channel occupancy	<8% (<1% typical)
Average Level-0 accept rate	1 MHz
Multiplexing at ASIC output	1024:32
Level-0 multiplexer output clock speed	40 MHz
Location	On detector
Level-0 adapter board parameters	
Number of ASIC's per module	2
Multiplexing factor at output link	16:1
Output link multiplexer clock speed	1.25 GHz
Effective maximum output bandwidth/fibre	1.00 Gbit/s
Output data links per adapter board	4
Location	On detector
Level-1 trigger parameters	
Average Level-1 accept rate	40 kHz
Maximum latency	2048 events
Location	Counting room
Event building network input parameters	
Maximum input bandwidth per Readout Unit (RU)	1.0 Gbit/s
Maximum number of inputs per RU	4
RU input standard	SLink
Average bandwidth into RU's	420 MByte/s
Location	Counting room

Table 14: Parameters of the RICH readout.

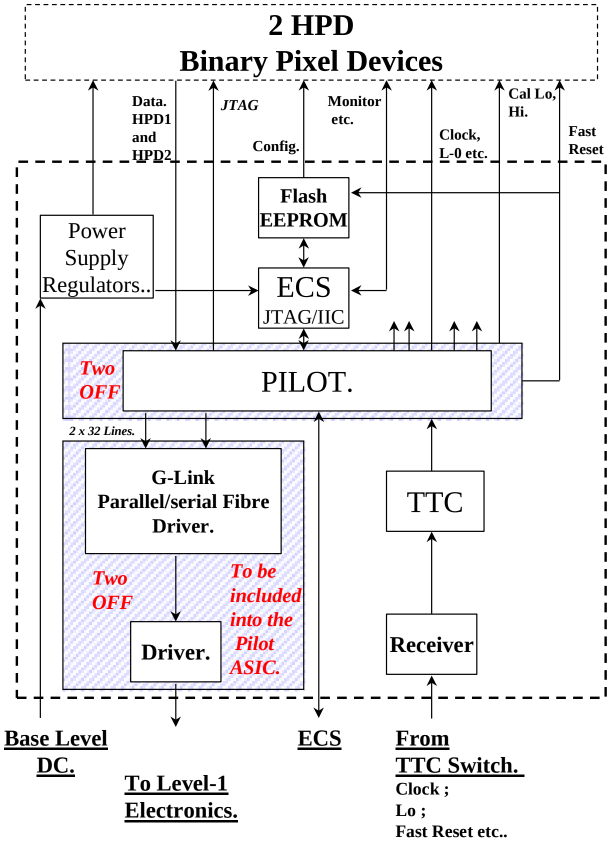

Figure 55: A schematic of the Level-0 Interface Unit.

1. Receives multiplexed data from the RICH detectors via the ∼100 m optical links;
2. Buffers the data during the Level-1 latency;
3. Removes events accepted by the Level-0 for which a negative decision was made by the Level-1 trigger;
4. Provides an interface to the Timing and Control (TTC) system and the Detector Control System (DCS);
5. Transports the data onwards to the DAQ and event building network.

The Level-1 architecture is shown schematically in Fig. 56 and the relevant Level-1 readout parameters are summarised in Table 14. Each Level-1 board will receive the multiplexed data from four Level-0 adapter modules on a total of 16 × 1 Gbit/s fibres. In addition, binary data from a Level-0 reference module (see below) will arrive on an extra two fibres. This gives a total of 972 optical links which are input to a total of 54 Level-1 boards.

At Level-1, the data are aligned, then stored in external DRAM of at least 2048 events depth until a Level-1 decision is made. This depth allows for the maximum time of a Level-1 trigger decision (2048 μs) at an average Level-0 accept rate of 1 MHz. The Level-1 latency is variable and has an average 40 kHz accept rate. On receipt of a Level-1 trigger accept the data are output-formatted. The logic will also include algorithms for zero suppression. The data are subsequently copied into a derandomizer register of depth 16, ready for transmitting to the LHCb Readout Units and the Event Building network. All Level-1 electronics modules will be driven from the same global clock (distributed via the TTC system).

All the buffering control and processing described above is implemented in FPGA technology. FPGA's are chosen to give maximum flexibility, with the possibility of reconfiguring the logic should it become necessary.

Accepted data stored in the Level-1 derandomizer buffer will be further multiplexed at the output stage of the Level-1 on 54 links, one per Level-1 board. The links are capable of sustaining a maximum rate of 1.25 Gbits/s into the Readout Units [54], one Readout Unit receives data from up to four Level-1 boards. Table 14 summarises the expected data flow requirements taking into account all data formatting overheads. The DAQ interface will use the SLink protocol [55], which will be implemented in FPGA technology. The average event size of RICH data is 10.5 kByte, which gives a bandwidth from Level-1 into the Readout Units of 420 MByte/s.

For error monitoring, a "Level-0 Reference Module" will continuously generate reference data that can be compared with Level-0 accepted data. This will emulate the Level-0 readout chain, and be equipped with a pixel chip in carrier form. The reference module will be located close to the Level-1 electronics in

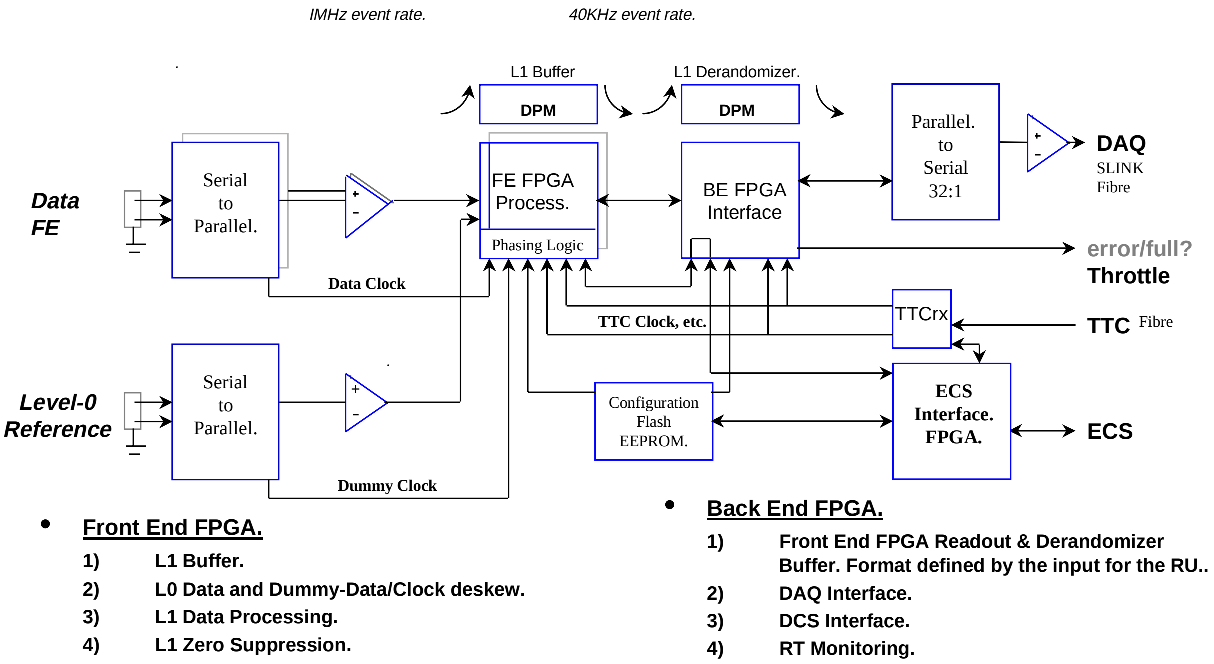

- **Front End FPGA.**
  1) **L1 Buffer.**
  2) **L0 Data and Dummy-Data/Clock deskew.**
  3) **L1 Data Processing.**
  4) **L1 Zero Suppression.**
- **Back End FPGA.**
  1) **Front End FPGA Readout & Derandomizer Buffer. Format defined by the input for the RU..**
  2) **DAQ Interface.**
  3) **DCS Interface.**
  4) **RT Monitoring.**

Figure 56: A schematic of the ODE architecture.

the low radiation environment and will therefore not suffer from SEUs. The integrity of the data can be checked event-by-event, by using the Level-0 data bunch-crossing ID in data, the bunch-crossing ID from the Level-0 reference module, and the expected value, calculated using the TTC bunch crossing ID. Errors due to missing clocks, phase shifts etc in the real data will hence be detected. All errors are flagged in the data and also reported via the ECS.

The 54 Level-1 modules can be comfortably accommodated in four 9U crates (two each for RICH 1 and RICH 2). We envisage housing the electronics in four racks. Each rack would then contain one 9U chassis for the Level-1 electronics, with the possibility of one further 9U chassis for the corresponding readout units.

5.2.5 Power supplies

Commercial power supplies are well known for not being radiation tolerant, hence all bulk regulated commercial supplies will be located within the counting room area. For the Level-0 adapter boards, it is proposed to have a base supply located in the counting room and radiation-tolerant on-detector regulators providing local regulation and control.

5.2.6 Ongoing developments

A prototype adapter board has been designed to read out the prototype HPD with encapsulated 256×32 binary pixel chip. The board has been fabricated and is currently under test.

Tests of prototype Level-1 modules are well underway. The 1999 test-beam readout system used the CMS Front End Driver (FED) [56] which already implements much of the required functionality. This includes the the implementation of the Level-1 buffering and programmability in FPGA technology. The extension to a binary front end with TTCrx and ECS functionality is currently under development. A Level-1 preproduction prototype will be available by the end of 2001.

5.3 RICH 1 Mechanics

The acceptance of the RICH 1 detector covers the angular range up to ±300 mrad in the horizontal (xz) plane and up to ±250 mrad in the vertical (yz) plane. An aerogel radiator lies between z=1060 mm and z=1110 mm,

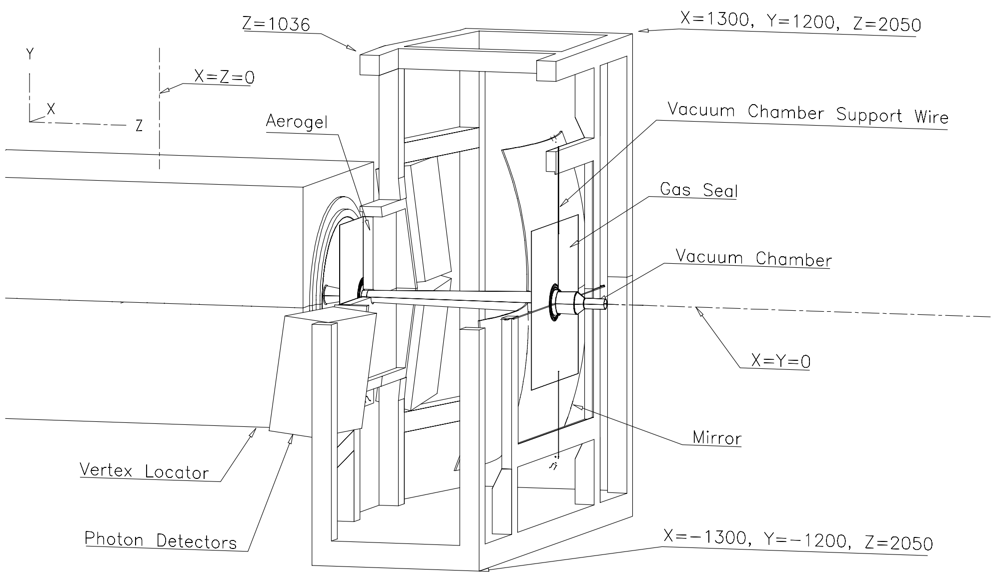

Figure 57: RICH 1 mechanics. The arrangement of the main components.

and a radiator of C_4F_{10} fills the region between z=1110 mm and z=2050 mm. The mirrors are tilted by ∼286 mrad horizontally and ∼65 mrad vertically. The detector will be operated at ambient temperature and within ∼50 Pa of the atmospheric pressure. The arrangement of the main components of RICH 1 is shown in Fig. 57. Figures 58 and 59 show the top (xz) view and side (yz) views of the detector.

Details of the RICH 1 design can be found in reference [57].

5.3.1 Gas vessel and support structure

A frame of stainless-steel box-section stiffened by plate will provide an adequately stable support for the RICH 1 components. The mirrors are the most demanding as they require that their angle be maintained to ∼0.1 mrad. The frame also supports the section of the vacuum chamber, which passes through RICH 1, by means of four wires at the entrance and exit window of the detector. The wires are attached to rings on the vacuum chamber.

As well as supporting the vacuum chamber during operation, the frame is intimately involved in its installation [58]. It will require the RICH 1 frame to be moved transverse to the beam by ∼2.5 m and carrying the vacuum chamber with it. Permanent support points, to which the frame can be returned with a precision of order 0.1 mm will be provided. These support points will probably be on the concrete floor at $y = -2150$ mm.

During access to the inside of RICH 1, the vacuum chamber will need protection. This protection will be mounted on a temporary bench standing on the vessel floor at $y = -1100$ mm.

The frame will be sealed to contain the C_4F_{10} gas radiator. The vacuum chamber acts as part of the boundary to the gas volume. Kapton foils of 150 μm thickness and ∼400 mm diameter will be glued to flanges on the vacuum chamber (Fig. 60). Carbon-fibre composite seals the rest of the boundary within the RICH 1 acceptance. Fused-silica windows of 5 mm thickness in front of the photon detectors and stainless-steel sheet elsewhere seal the rest of the volume.

The Kapton foils must not impose undue stress on the vacuum chamber. They have undulations moulded in to make them more flexible. They will be assembled from three layers of Kapton cut radially, passed over the vac-

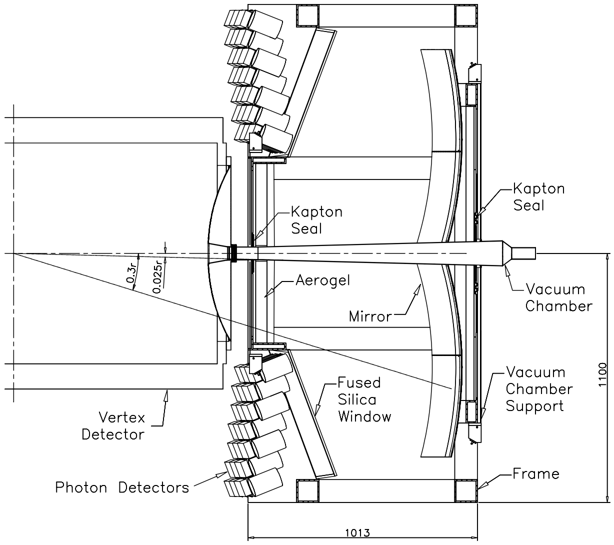

Figure 58: RICH 1 mechanics. Top view.

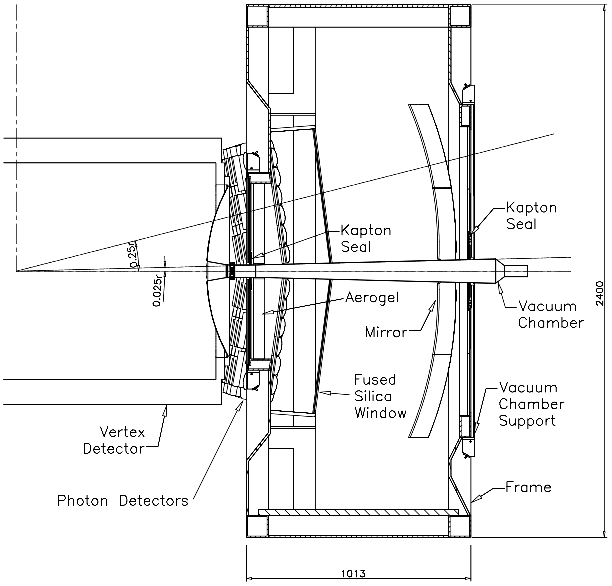

Figure 59: RICH 1 mechanics. Side view.

uum chamber and bonded together in place. All seals, including the fused silica windows, must withstand a working pressure differential of 300 Pa guaranteed by the gas supply. A peak differential pressure of 500 Pa is set by high throughput safety bubblers. Further information about the fluids system can be found in Section 5.5 and in Reference [59].

5.3.2 Photon detector mounting

The Pixel Hybrid Photon Detectors (HPDs) [5] are arranged in a hexagonal close-packed array with 87 mm spacing. Local reduction of the residual magnetic flux density will be achieved with a magnetic shielding alloy around each HPD. Each pair of HPDs is served by a single electronics card (Level-0 interface) as shown in Fig. 61.

The individual magnetic shields for the HPDs are grounded. The high voltage components of the photon detectors will be insulated from their magnetic shields by two layers of 125 μm Kapton film. All electrical connections to a photon detector will be made through the end opposite the photocathode.

Since the photon detectors must point towards the incident light, their axes are not normal to the image plane on which the photocathodes lie. They are rotated towards the beam by ~ 500 mrad horizontally and away from the beam by ~ 125 mrad vertically. In this way the magnetic shields cast minimal shadows on the photocathodes. It is the vertical rotation which forces the photon detectors on each side to be separated into quadrants.

The magnetic shields will be located with a precision of ± 0.4 mm in a metal web. This web is built up with increasing offsets along the photon detector axis for successive tubes. This ensures the correct angle between tube axes and the image plane. A black plastic moulding, screwed to the HPD and the web, will locate them in z and provide some light-tighting. An aluminium frame surrounds the web. It provides the means to withdraw and replace the quadrant reproducibly. As the quadrants will need to be withdrawn to the sides in order to replace photon detectors, they will be mounted on rails with the working positions defined by dowels. Once the photon detectors are mounted, there will be no further adjustment of position because there is no room for useful movement in z and the image can be moved over the photocathodes by adjusting

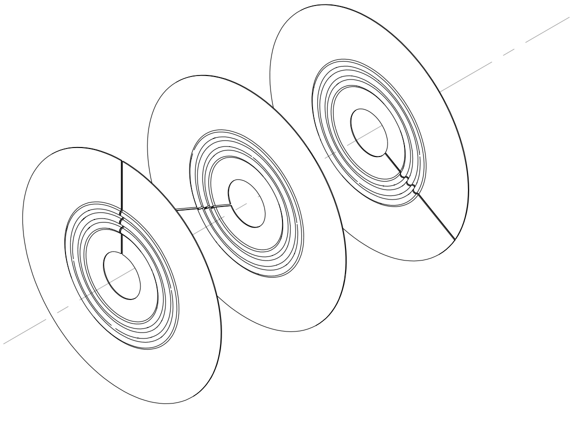

Figure 60: The Kapton seal between the vacuum chamber and the RICH 1 structure. These seals are constructed from 3 layers with the radial cuts that are needed to pass them over the vacuum chamber. The cuts are staggered to prevent leaks along one joint.

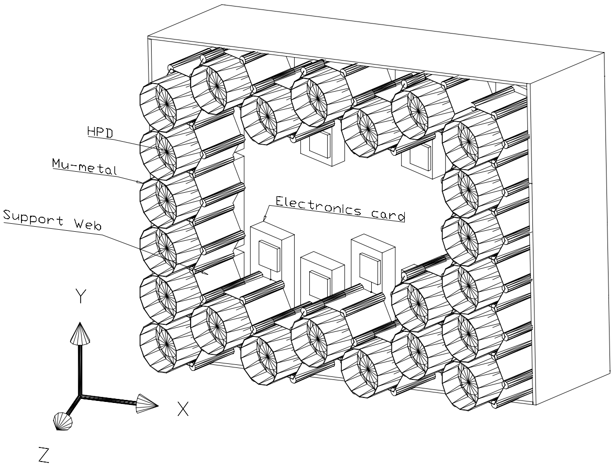

Figure 61: Part of the photon detector array for one quadrant in RICH 1.

the mirror.

5.3.3 The mirrors and the mirror support

The four mirrors are parts of spheres of radius 1700 mm, with their centres at (±500, ±110, 275). The shorter focal length and increased tilt compared to the Technical Proposal [1] are imposed by the need to accommodate the photon detectors with the vertex detector tank. Each quadrant covers an area of 900 × 750 mm^2 and is divided into 4 mirror segments supported at their centres. The baseline choice of material is 6 mm thick aluminised glass protected by a coating of quartz [45].

The mirror support is designed to allow adjustment of the horizontal and vertical angles of each mirror segment from outside the RICH gas radiator volume. There will be limited adjustment of the z-positions, but only from inside the gas envelope. The support structure for each segment consists of a 3-legged spider made of a composite material (Fig. 62). These segments are in the Cherenkov gas enclosure. Dedicated tests are scheduled to define the material and the compatibility with the fluorocarbon gas.

The legs radiate from a central hollow cylinder glued to the mirror with epoxy resin. This central position is the only place where the spider is fixed to the mirror. Adjustment of the angle of a mirror segment will be made by worm and cam mechanisms mounted where the feet of the spider locate on a space-frame. This supports all the segments on one side of the beam. The space-frames (Fig. 62) consist of C-frames outside the acceptance. Intermediate members carry the worm and cam mechanisms. All the mirrors on each side of the beam have to be removed from RICH 1 when access is needed to the beam-pipe. This will be done by withdrawing the space-frames, with the mirror segments attached, to a protective housing at the side. The motion will take place along rails near the top of RICH 1. The working position for each side is defined by two support points on the rail and one point fixing z near the bottom of RICH 1.

All the segments on one side of the beam will be aligned with the assembly withdrawn from RICH 1. The centres of curvature are thereby accessible. When the mirrors are inside RICH 1 the centres of curvature are inside the vertex detector tank, but the relative alignment of mirror segments can be checked by shining parallel light onto two or more segments at once and examining the image on the focal surface [60].

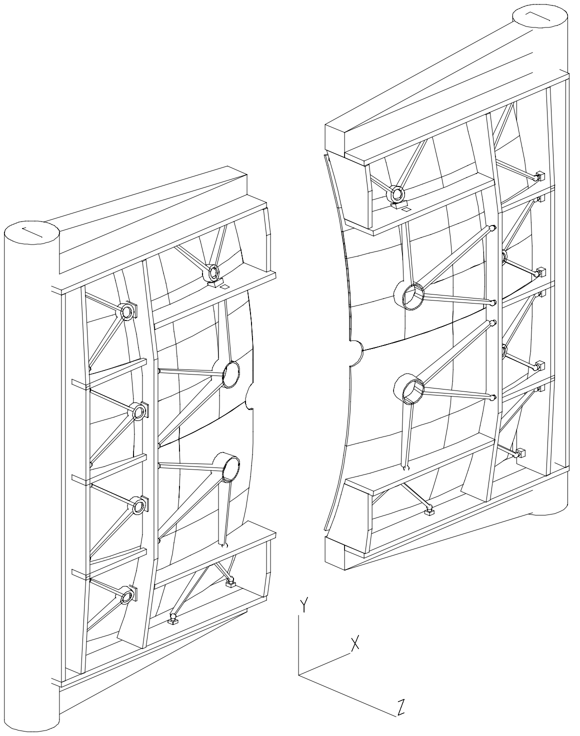

Figure 62: Two halves of the space-frame which supports the mirror adjustment points in RICH 1. Each quadrant covers an area of 900 × 750 mm^2.

5.3.4 Aerogel

The aerogel radiator [25] will be assembled from tiles approximately 200 × 200 × 50 mm^3. They will be housed in an envelope of aluminium with the Cherenkov light leaving via a window of 250 μm thick transparent plastic. The aerogel of the preferred type is hygroscopic. Provision will be made to flush the envelope with dry nitrogen.

5.4 RICH 2 Mechanics

The acceptance of the RICH 2 detector [61] covers the angular range up to ±120 mrad in the horizontal projection, xz-plane, and up to ±100 mrad in the vertical projection, yz-plane. The enclosed gas volume extends from z=9450 mm to z=11470 mm. The optical system consists of two spherical mirror arrays and two flat mirror arrays. The radius of curvature of the spherical mirrors is 8000 mm. The tangent to the spherical mirror plane at $x = 0$ in the xz-plane is ±450 mrad with respect to the x-axis. The flat mirror plane is tilted in the xz-plane by ±140 mrad with respect to the x-axis. The two detector planes are thereby defined between $[x, z]$ [±4052,10342] and [±3635,10827]. The flat mirror plane is outside the 120 mrad acceptance. The mean Cherenkov radiator length is about 1670 mm. The gas is CF_4 at atmospheric pressure [59] and ambient temperature. Figure 63 gives the horizontal projection and Fig. 65 gives the side projection of the detector. Figure 64 gives xy-projections of the detector.

5.4.1 Gas vessel and support structure

The supporting mechanical structure is an open rectangular space frame where all structural components are kept outside the acceptance of the LHCb spectrometer which is ±300 mrad in the horizontal plane (the bending plane) and ±250 mrad in the vertical plane. The structure is welded and the total weight is about 11000 kg. The entrance and exit windows are light-weight composite material panels made from 48 mm polymethacrylimid foam with 1 mm thick glass-fibre reinforced epoxy sheets, G10, on each side. A thin skin of metal foil is added to the G10 plates which faces the Cherenkov gas volume. The total radiation length for each panel is 1.4 % X_0. The windows are designed to withstand the hydrostatic pressure of the Cherenkov gas $^{+200}_{-100}$ Pa as defined at the top of the detector. A tube, coaxial to the vacuum chamber, runs through the detector. The tube is 3 mm thick and made from G10. It has a 30 mm larger radius than the vacuum chamber. A 5 mm-thick plate of fused quartz separates the Cherenkov gas volume and the volume occupied by the photon detectors.

5.4.2 The mirror array and support

The spherical mirror arrays are made from a matrix of smaller hexagonal mirror segments, as seen in Fig. 64. Each mirror is inscribed in a circle of diameter 502 mm and made from a 6 mm-thick glass substrate with a UV enhanced aluminium coating. A quartz protec-

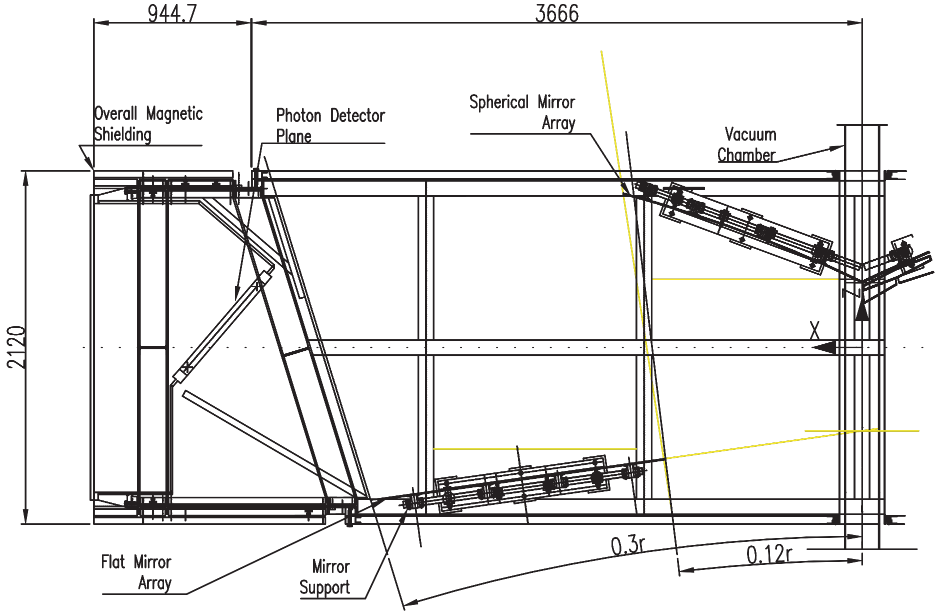

Figure 63: Horizontal projection of the RICH 2 mechanics.

tive coating will be added onto the reflective surfaces. (See Reference [45]). Only one size of mirrors is used apart from at the vertical edges where half mirrors are introduced. Special segments have to be foreseen near to the inner tube. The acceptance of the spherical mirror arrays extends to 125.4 mrad in the horizontal plane to reflect all the Cherenkov light created by particles inside the 120 mrad acceptance. Along the vertical axis the mirror arrays extend up to about 120 mrad. The flat mirror segments are similar, but are assumed to be squares of 437 × 437 mm^2 (Fig. 64).

A 40 mm-thick aluminium honeycomb flat panel is the supporting structure for both the spherical and the flat mirror arrays. The lightweight metallic structure is preferred here in order not to have any problems of compatibility with the fluorocarbon gas and maintaining a high degree of mechanical stability. The average overall radiation length is 3.3 % X_0. The plate is referred to a tri-square which acts as an optical bench. This optical bench is supported by the space frame.

A polycarbonate ring is glued with standard epoxy resin to the back of each of the spherical mirror segments and a corresponding flexible polycarbonate membrane is inserted into the aluminium honeycomb flat panel. A polycarbonate hollow rod connects these two elements–see reference [46] and Fig. 66. This flexible mirror mount has been demonstrated to be stable in the vertical and in the horizontal projection to within 0.03 mrad over 5000 hours after the first 100 hours relaxation period [45]. We have chosen polycarbonate for the mirror support due to its excellent mechanical stability and long, 346 mm, radiation length. It also has a low, 0.2 to 0.3 %, Total Mass Loss and a low water absorption of 0.15 % [7]. We started a year ago a long term stability test of polycarbonate in fluorocarbon by immersing test samples in warm, 40°C, vapour of C_6F_{14}.

5.4.3 Overall magnetic shielding

A heavy iron structure is used to shield the photon detectors from the stray magnetic field–see Reference [62] and Fig. 63. A triple layer of 40 mm-thick soft steel, separated by

---

[7] MATLAB: 003 and Bayer Corp. Plastics Div. Makrolon, Polycarbonate

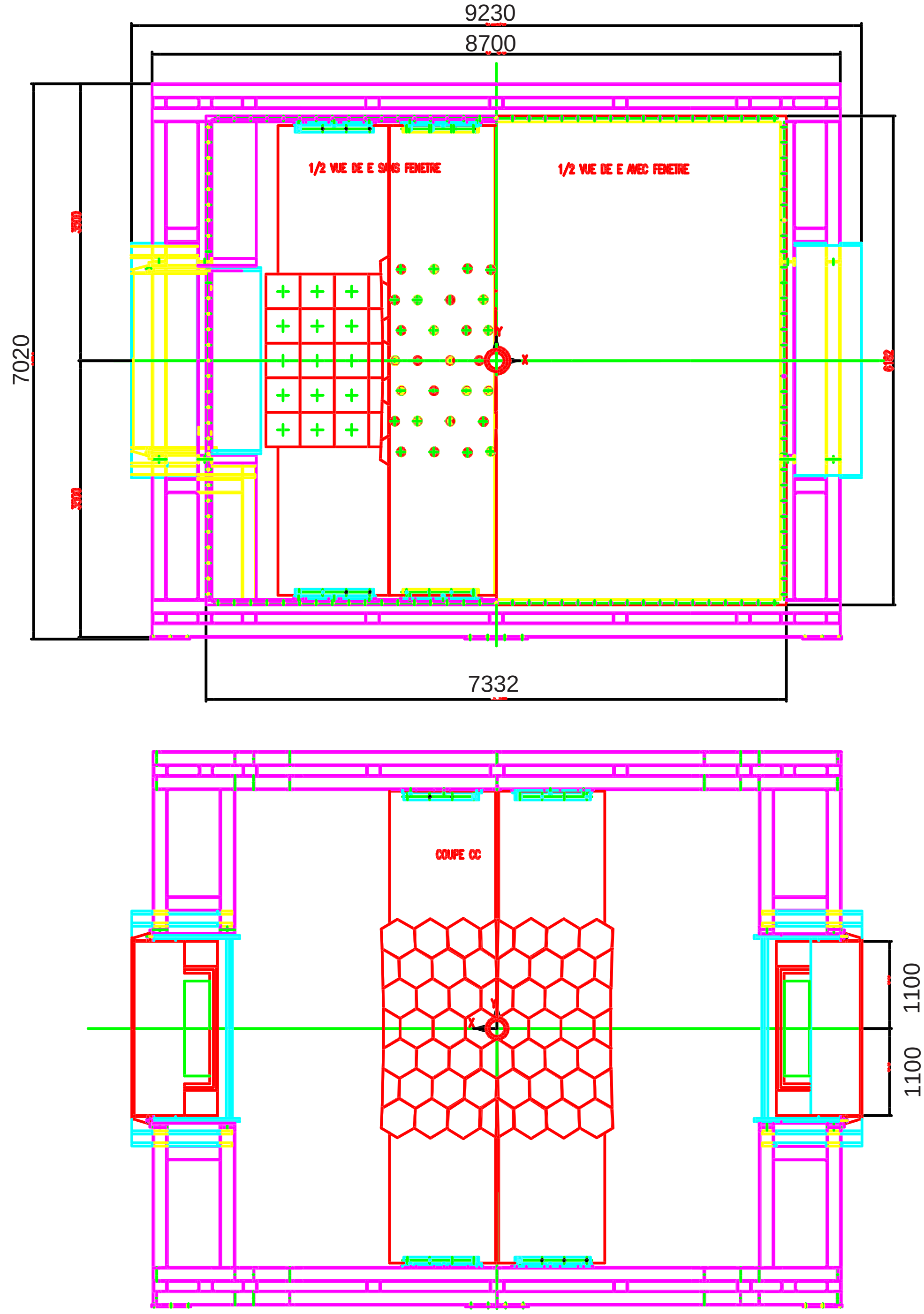

Figure 64: RICH 2 mechanics. Projections onto the xy plane with the windows partially removed.

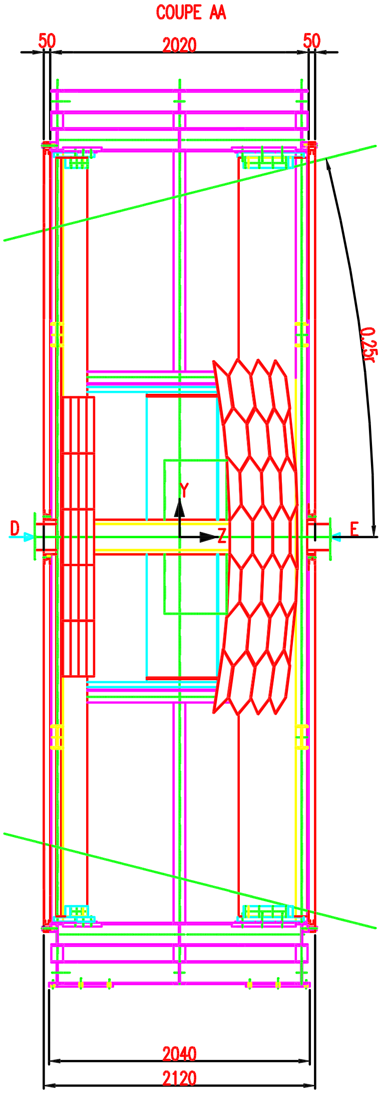

Figure 65: Side view of the RICH 2 mechanics.

about 115 mm, surrounds the sides of the detector. In addition, two 40 mm thick soft steel walls close the front of the detector while leaving full acceptance for the Cherenkov photons. The weight of this structure is about 11000 kg on each side which takes the total weight of RICH 2 to about 34 tonnes.

With reasonable assumptions about the stray magnetic field, this structure will assure a residual magnetic flux density below 1 mT in the region of the photon detector plane. Local reduction of the flux density will be achieved with a cylinder made of magnetic shielding alloy around each HPD. This cylinder is an integral part of the HPD assembly. Further details are in Reference [5].

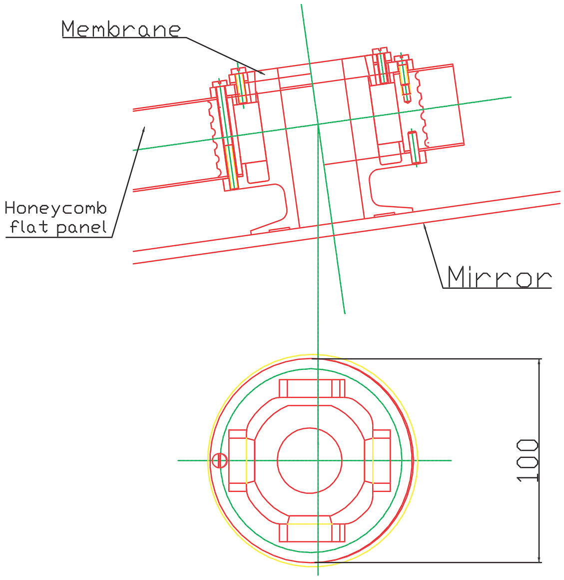

Figure 66: The mirror support in RICH 2.

5.4.4 The detector plane

The Hybrid Photon Detectors (HPDs) [5] are arranged in groups of two, located by means of their own pins on a common multilayer board through a ZIF socket, thus making an elementary subassembly unit. Each of these units is located in an aluminium supporting frame that houses 8 sub-assemblies arranged in columns. These sub-assemblies are mechanically fixed to the HPDs back-plate through spacers made of thermoplastic resin–see Fig. 67 and Reference [63]. The frame also houses one electronics board (Level-0 interface) on the back of each unit.

There are in total 9 supporting frames on each panel which can be individually pulled backward without disturbing the neighbouring ones, sliding on their own guides. They are fixed by means of dowel pins and screws to a main supporting frame. This main supporting frame is made of aluminium.

All HPD cables will leave the HPD through its back-plate, and will be routed by the side of the supporting frame. Local strain relief of the cables to the frame can be easily foreseen.

As the heat generated by the HPDs themselves is relatively low, we do not expect any problem in draining it away with natural, or eventually forced, gas flow. The heat power loss of the electronic boards on the rear side of the detector plane will probably not require a conductive cooling system as the packaging is rather open.

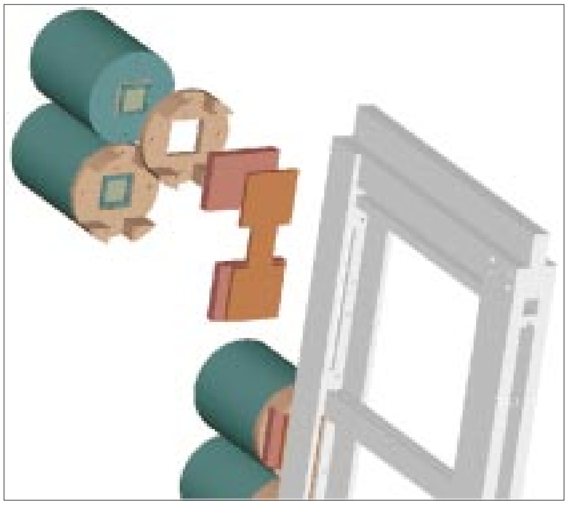

Figure 67: The arrangement of the HPDs at the detector plane in RICH 2.

5.4.5 Mechanical structure analysis

A preliminary study of the RICH 2 mechanical structure was performed to assess the response of the structure under static and dynamic loading conditions. The complexity of the geometry of the structure is such that a Finite Element Analysis is necessary to calculate the exact mechanical behaviour. Both an initial static and modal analysis have been carried out.

The rigid mechanical space frame of the RICH 2 structure was modelled [8]. Structural contributions from the thin stainless steel panels and the low-mass composite entrance and exit windows are ignored in the calculations. Figure 68 shows a maximum static deflection of 1.4 mm occurring at the centre of the upper longitudinal beams. A modal analysis was performed using the same geometry and constraints to enable the determination of the first three natural frequencies of the structure. In this calculation only the mass of the magnetic shielding together with the self mass of the structure are included in the model.

Further work is now envisaged to subsequently optimize the mechanical design with regards to the important stability and accuracy requirements of the detector.

Mode	1	2	3
Frequency (Hz)	1.2	1.4	2.9
Twist along	z	z	x

Table 15: The relative movement of the nodes in the RICH 2 structure.

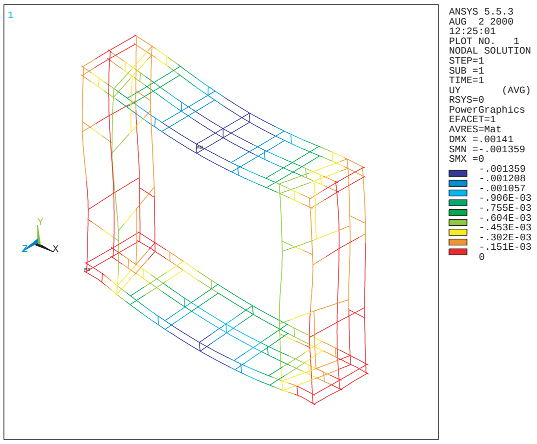

Figure 68: Static deflection of the RICH 2 space frame. Magnetic shielding and mirror plane included.

5.5 The Gas Systems

The RICH 1 radiator with its volume of 4 m^3 will use C_4F_{10} and RICH 2 will be filled with 100 m^3 of CF_4. The main parameters can be found in Table 16 and in Fig. 69. Further information about the systems can be found in Reference [59]. Both radiators remain gaseous at normal temperature and pressure. To keep the

---

[8] ANSYS 5.5 Elements Reference Manual 4-993

photon absorption at an acceptable level, the oxygen and water impurities have to be limited to about 100-200 ppm. The nitrogen contamination has an effect on the refractive index and therefore will be kept constant and below 1 %. Both gas systems will run in a closed loop circulation, distributed over three regions; at the surface in the gas building, in the cavern behind the radiation wall and at the detector. The expected circulation flow rate per hour will be close to 10 % of the total gas volume. The exact rate will depend on the level of impurities in the system. An inline purifier consisting of a 3Å or 4Å (C_4F_{10}, CF_4) and a 13X (CF_4) molecular sieve will remove the water impurities as well as trace gases. Two gas inlets and two gas outlets, one of each at the bottom and on the top of the detector, will be connected to the distribution system. A pump in the return line allows the gas to be compressed before entering the gas buildings at the surface. To stabilise the pressure in the RICH detector, the pump will be driven by a frequency regulator controlled by pressure sensors in the detector. A buffer volume in the RICH 2 gas circuit is needed in order to react to fast changes of the atmospheric pressure.

		RICH 1	RICH 2
Cherenkov Gas		C_4F_{10}	CF_4
Detector Volume	(m^3)	~ 4	~ 100
Flow Rate	(m^3/h)	~ 0.4	~ 10
Impurity			
O_2	(ppm)	100-200	100-200
H_2O	(ppm)	100-200	100-200
N_2	(%)	≤ 1	≤ 1
Relative Pressure Stability	(Pa)	≤ 50	≤ 50

Table 16: Cherenkov Gas Parameters

To recover the fluorocarbons of the RICH 1 and RICH 2 detectors, recovery plants are recommended. They will separate the fluorocarbon from nitrogen and oxygen. The C_4F_{10} will be liquefied at a temperature of -50°C and CF_4 at -160°C, which allows the nitrogen and oxygen to be vented while they remain in gaseous state. The CF_4 of RICH 2 will only be recovered during the filling and emptying phase, while the C_4F_{10} recovery will be implemented in the RICH 1 closed loop system (Fig. 69). The existing DELPHI supply and return pipes between the SGX building and the UX cavern will be reused by the LHCb experiment and hence for the two RICH systems. The gas control will follow the general recommendations of the Joint Control Project of the four LHC experiments (JCOP).

5.6 Alignment

The angular resolution of the RICH detectors of LHCb depends critically on having an accurate alignment of all its optical components. The experimental aim is to have an angular resolution of 1.4 mrad in RICH 1 and 0.5 mrad in RICH 2 [1]. In order to ensure that any uncertainty in the alignment does not degrade the angular resolution of the RICH detectors, the aim is to maintain such an alignment error below 0.1 mrad.

It is foreseen that the alignment strategy be carried out in three stages [60] [45]:

1. Installation and survey of the mirror and detector components;
2. Monitoring of the alignment with a laser alignment system;
3. Final alignment with data.

5.6.1 Installation and Survey

The first step towards providing an alignment procedure is to accurately survey the positions of the mirrors and photon detectors as they are mounted.

In the case of RICH 1, the assembly of the whole module will be performed in a separate laboratory. The centres of curvature of each mirror quadrant, the centre of the photocathode of each HPD and the directions of the axis of each HPD will be known to ±0.5 mm in the transverse co-ordinates (x and y) and ±2 mm in z. The centres of curvature for the four segments in a mirror quadrant will be adjusted until these coincide in a single point. The hexagonal web that supports the HPD array has a mechanical tolerance of ±0.4 mm but this

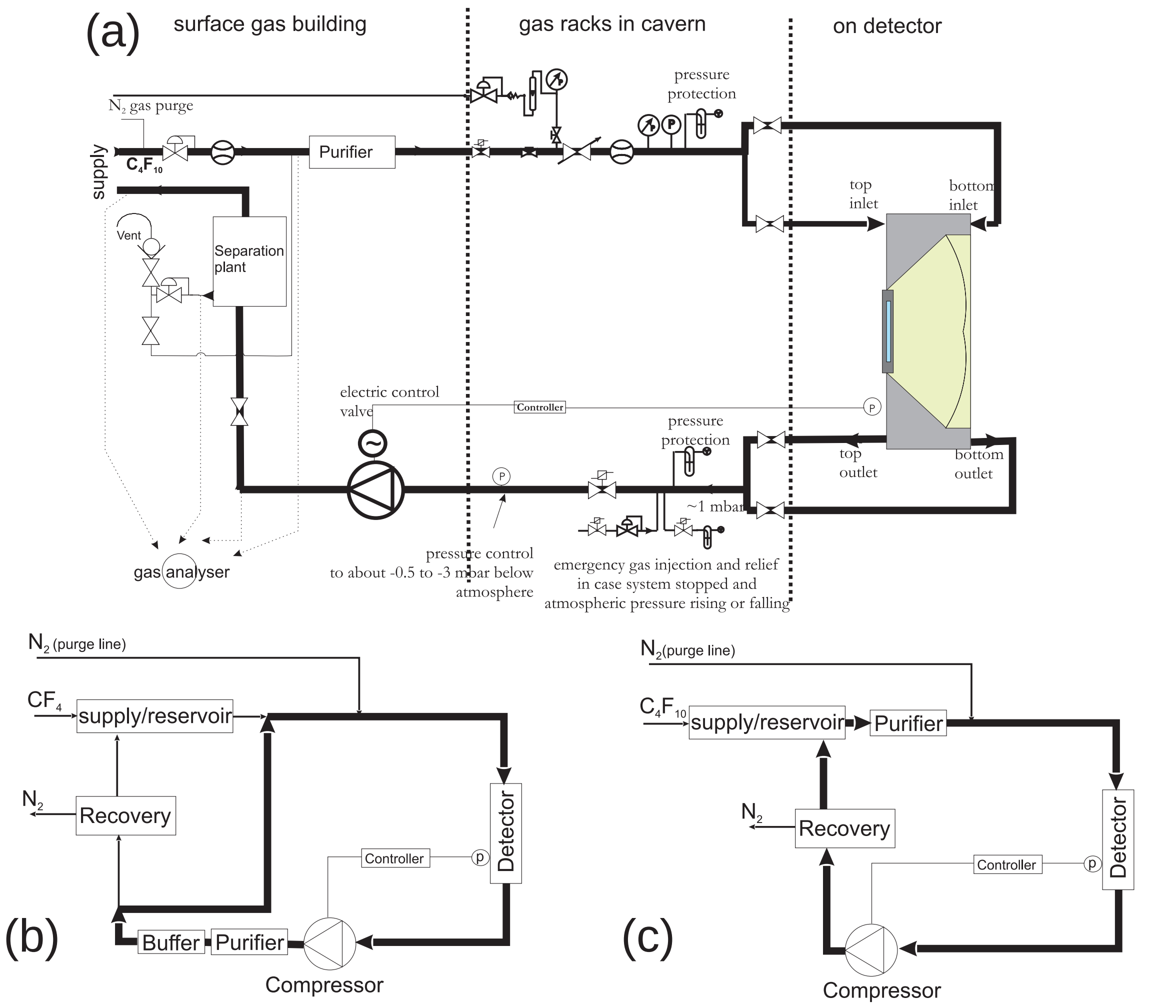

Figure 69: Flow diagram for the RICH gas systems: (a) the distribution system for C_4F_{10}; (b) and (c) the conceptual layout for RICH 2 and RICH 1, respectively.

can be further constrained by a pre-surveyed array of LEDs and a mask perpendicular to the HPD axis to illuminate these and to give the relative positions of the HPDs with respect to the support frame. The RICH 1 detector would then be positioned in place and the vacuum chamber installed, allowing one to obtain the relative positions of the frame structure with respect to the vacuum chamber co-ordinates.

For the case of RICH 2, each of the mirror and detector components will be assembled independently in clean laboratory conditions and then brought together. Each spherical (flat) mirror will be aligned with respect to the other mirrors to form a sphere (plane) with the centre of curvature pointing to the centre of the hypothetical focal plane. The superstructure is surveyed and the optical bench is defined. This defines the reference axes and the focal points. Then the spherical walls are mounted and aligned with respect to these focal points by means of a laser point source[9]. Next, the flat walls are mounted and the point source is moved into a position situated roughly on the particle beam axis. The photon detector plane is installed and surveyed with respect to the superstructure. Then the flat and spherical walls are aligned to generate a single im-

---

[9] The mirrors are aligned to generate a point image corresponding to the point source.

age point on the normal to the photodetector plane. When the RICH 2 detector is lowered in the pit and placed on the beam axis, the relative alignment of the flat and spherical walls is repeated to check and correct eventual misalignments. The overall alignment error foreseen is set solely by the survey (±1 mm shift on the photodetector plane) and by the precision of the optical mounts. The resolution for the spherical and the flat mirrors and the mount precision will set the overall resolution of the optical system. At the photocathode plane, it can be expressed as

$$\sqrt{\sum_i \sigma_i^2 \times l_i^2}$$

where l_i is the path length of the light to the photocathode and i denotes the different components; spherical/flat mirror and the mirror mounts. For equal error on all the components and an overall error $\sigma \leq 0.1$ mrad gives $\sigma_i \leq 0.06$ mrad.

5.6.2 Laser Alignment System

A laser alignment system for each of the two RICH detectors can perform the following two functions:

1. It can perform a quick and final cross-check of the link between the mirror planes and the photon detector plane before any gas is introduced into the gas enclosure.
2. It can be used to continue monitoring the positions of the detector components throughout data taking, thereby making allowances for thermal and vibrational corrections.

The laser alignment system would consist of a series of discrete laser points installed in front of the first mirror plane (at least two points per mirror) that can be compared with their theoretically mapped positions on the photon detector plane. The unambiguous nature of the laser points simplifies the alignment procedure, allowing one to optimise the tilts and positions of the mirrors in real time. The delivery system for these laser beams could be an array of single-mode optical fibres with collimator optics, producing diffraction limited Gaussian shaped laser beams. These have been proposed for the multi-point alignment system of the ATLAS muon spectrometer [64, 65, 66] producing beams with a width of 2-3 mm over distances between 10-20 m [64]. These fibres with their collimating optics could be arranged in a matrix, supported by a light frame structure, in front of the spherical mirrors, only adding minimally to the material budget inside the acceptance of the RICH detectors. The fibres could be mounted on the spherical mirrors themselves, perpendicular to the mirror surface. This would avoid having a support structure. Alternatively a laser system with a piezo-assisted mirror can scan the whole mirror array onto the photodetectors. The aim is for an initial alignment precision of about 0.5 mrad. Further discussion on these systems is given in Reference [60].

5.6.3 Alignment with data

The final stage in the alignment process would involve performing an iterative alignment procedure with the data themselves, by selecting tracks with $\beta \cong 1$, and minimising the residuals incurred by tilt and position adjustments with respect to the theoretically expected positions of Cherenkov photons unambiguously associated to mirror segments, if the mirrors and detectors were ideally aligned [67, 68].

If the reconstructed Cherenkov angle is θ_{rec} and the expected angle is θ_{exp}, any misalignment in the mirror segments with respect to the photon detectors is observed by measuring the difference between the two angles as a function of the reconstructed azimuthal Cherenkov angle ϕ_{rec}:

$$\theta_{rec} - \theta_{exp} = A\cos(\phi_{rec} - \phi_0), \qquad (4)$$

where A and ϕ_0 are fit parameters.

The positions and tilt angles of the mirror segments are displaced in such a manner that the Cherenkov angle residuals are minimised. This procedure has to be iterated a number of times to achieve the optimal residuals in all the mirror segments. A preliminary study performed within the context of RICH 2 [68], suggests that if the initial alignment has an accuracy of ~ 0.5 mrad, then a total alignment accuracy of 0.2 mrad (including mirror quality) can be achieved.

5.7 Monitoring and Control

The performance of the RICH detectors of LHCb can be kept under control if one is able to monitor physically relevant quantities throughout the duration of the experiment [60]. The main factors that affect the performance are the conditions of the gas, including its refractive index and transmission characteristics, the stability of the support structures, the functionality of the electronics and the efficiency and quality of the photon detectors.

Each of the closed circuit re-circulation gas systems for the two RICH detectors [59] include control and monitoring systems to ensure the quality of the two gases, C_4F_{10} and CF_4. The following parameters will need to be monitored in the re-circulation plants:

1. Flow meters to measure the gas flow;
2. Pressure sensors for atmospheric pressure and for pressure differentials between gas inlet and outlet;
3. Gas purity analysers, to measure the concentration of water and oxygen (to remain below 100-200 ppm);
4. Temperature sensors in the gas vessel;
5. The temperature, pressure and valve controls of the cryogenic plant;
6. The nitrogen concentration in the gas (which should be constant ≤ 1 %) by means of an ultrasonic sensor to measure the velocity of sound [69];
7. The refractive index of the gas as a function of pressure with a Fabry-Perot interferometer [70, 71] consisting of a monochromator, etalon and CCD camera[10];
8. The transparency and attenuation length of the gas between 200 and 800 nm with a monochromator and a gas vessel of varying length [72].

The mechanical stability of the supporting frame needs to be monitored to ensure that thermal and vibrational movements do not affect the position resolution of the mirror mounts and the photon detector mounts. Semi-transparent position sensitive amorphous silicon sensors [64, 65, 66], developed for the optical multi-point alignment system of the ATLAS muon spectrometer, can be deployed on the mechanical frames. Deflections in the supporting structures are measured by alignment reference points delivered by lasers attached to single-mode fibres with collimating optics. The sensors consist of two 20×20 mm^2 orthogonal layers of 64 strips that can achieve a spatial resolution of ~ 1 μm [64, 73].

The following detector electronics parameters will need to be measured and controlled:

1. High voltage of the photon detector tubes;
2. Voltage across the HPD focusing elements;
3. Bias voltage for the pixel detector;
4. Leakage current of the pixel detectors;
5. Low voltage for the detector electronics;
6. Binary electronics discriminator threshold;
7. Test pulse for electronics calibration.

The identification of dead channels and the measurement of photon detector efficiencies can be performed with a diffuse pulsed light

---

[10] One would compare to the average n obtained from the reconstruction of the Cherenkov angle.

source (either an LED, a xenon lamp with filters or a monochromator) inside the RICH vessels. The magnetic field at the position of the photon detector plane will also be monitored with a series of Hall probes.

The control hardware and software of the RICH detectors of LHCb will conform to the accepted format for the Joint Control Project (JCOP) of the four LHC experiments [74]. The LHCb Experimental Control System (ECS) will interface with the Detector Control System (DCS) of the the RICH detectors. Programmable Logic Controllers (PLC) will run each of the devices under the Supervisory Control and Data Acquisition (SCADA) software, which will be common to all LHC experiments[11]. The SCADA system will be versatile enough to allow the configuration of multiple device components running on a variety of data buses.

Device user interfaces will allow users to control and monitor parameters, alarm levels and execute specific actions. Proper logging of the data will be carried out within this framework. A partitioned data model in which the control units are mounted locally will allow autonomy from the general operation and will minimise the network traffic. The use of common hardware and software control systems amongst all the LHC experiments allows one to standardise solutions for common problems. The RICH control systems group will work in close collaboration with the ECS group of the LHC to find common solutions for all the control demands of the LHCb RICH detectors.

5.8 Cabling and Infrastructure

Low voltage power cables and optical fibres from the counting room to RICH 1 and RICH 2 will be of the order of 80-100 metres in length. The aim is to keep the lengths of the power cables as short as possible to reduce both ohmic losses and to improve the stability of the base supplies in the counting rooms. Therefore the power cable route should be as direct and as short as possible but routed along standard cable trays. The cables will route through the RICH photodetector enclosure using standard low voltage sockets and panel mounting plugs.

The fibre optic route should not incur sharp bends or compressive/tension loads for the fibres. There is not the same restriction on the overall length. Lengths of fibres terminating at the same Level-1 module will be of equal lengths to better than 1/6 metre (0.5 ns). The differences in time due to fibre length to each receiving module can be compensated within the TTCrx for time differences spanning 16 bunch crossings (400 ns). The ideal optical fibre route should pass through the RICH photodetector enclosure without incurring a penalty of additional coupling connectors at the wall. Options are currently being investigated. The conceptual design is shown in Fig. 70.

The high voltage cables, 20 kV, will be routed from the control room to the RICH vessels. There will be a total of 64 cables. The cables will ideally pass through the RICH photodetector enclosure via a multi-way HV gastight connector. The total energy due to the charge in any cable will not exceed 2 Joules. The proposal is to terminate the cables and fibres at the RICH 1 and RICH 2 areas at eight regions. This corresponds to the quadrants in RICH 1 and RICH 2.

General cable information:

1. 64 high voltage cables carrying 20 kV.
2. 64 low voltage cables for each voltage[12] It is hoped to reduce the number of the transmitted voltages by using local onboard regulators. In this scheme, total current capacity in any cable for each voltage is seen not to exceed 5 A.
3. Each supply will have its own current carrying return (Common).

The installation program for power supplies/racks/links and commissioning will follow the LHCb schedule.

---

[11] A commercial tool contracted out by a tendering process.

[12] +5 V; 3.3 V; 2.0 V; +1.6 V digital; +1.6 V analogue; +0.8 V analogue; +0.8 V digital.

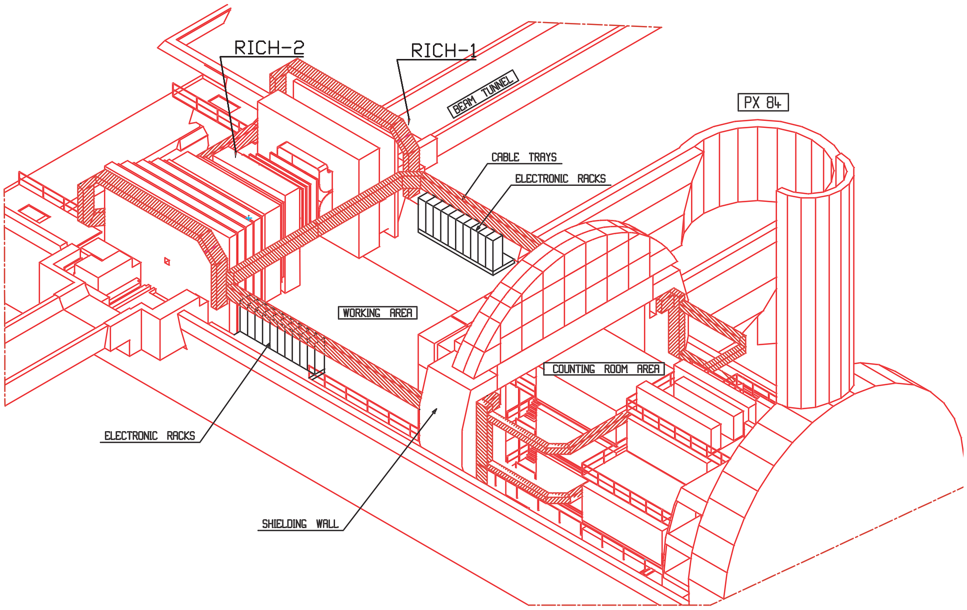

Figure 70: Layout of the LHCb experiment showing the detectors, the counting rooms and the cable routing. RICH electronics racks are located in the counting rooms.

The common point for the low voltage and the high voltage will be at the detector end. Care will be taken to ensure that if any break or open connection occurs in these cables or links the high and low voltages do not drift to dangerous levels. Where necessary, earthing standards, currently being studied by LHCb, will be adhered to.

5.9 Safety aspects

The RICH detectors of LHCb will follow the CERN safety rules and codes, CERN safety document SAPOCO 42 and European and/or international construction codes for structural engineering as described in EUROCODE 3.

Specific risks, and actions, as discussed in the Initial Safety Discussion (ISD) with the CERN Technical Inspection and Safety (TIS) Commission:

1. The Cherenkov gases, C_4F_{10} (CAS-RN 355-25-9) and CF_4 (CAS-RN 75-73-0), are not flammable and have UN classification 2.2 [13]. Due to the relatively large quantities of these gases in the cavern, 4 m^3 of C_4F_{10} and 100 m^3 of CF_4, and the high density of these gases, 10.5 g/l for C_4F_{10} and 3.9 g/l for CF_4, oxygen deficiency meters will be installed near to the detectors.
2. As the detectors will be operated with a maximum overpressure towards the atmosphere of 500 Pa set by high throughput bubblers, the vessels are not classified as pressure vessels [14].
3. The quartz plates, which isolate the photon detector environment from the Cherenkov gas, will be tested [15].
4. Particular attention will be given to the Welding Procedure Specification both for the aluminium and for the stainless steel and to the inspection of these welds.
5. The photon detectors will be run at 20 kV [16]. The total current for each supply line will be $\leq 100\mu$A. The low volt-

---

[13] UN classification 2.2 corresponds to non-toxic and non-flammable substances.

[14] Safety code D2 Rev.2

[15] Safety Instructions 34

[16] H.V.A. as defined in Safety Instructions 33

age supply to the detector read-out is below 15 V [17]. The total power dissipation on the detectors is $\leq$ 1kW and $\leq$ 8kW in the counting rooms in the cavern. Appropriate interlocks and current monitors will be installed together with interrupts at the source.

6. Work will occasionally be done inside the gas enclosure of the detector. Appropriate purge of the fluorocarbons and ventilation will be ensured [18].
7. The high pressure part of the gas systems is located in the surface buildings. The systems will be built according to the appropriate rules [19].
8. The effects of Seismic activity will be studied in collaboration with TIS.

---

[17] Safe Extra Low Voltage (S.E.L.V.) as defined in Safety Instructions 33

[18] Safety Code A4 Rev

[19] Safety Instruction 42 and Safety Code D2 Rev.2

6 Project Organisation

6.1 Schedule

The overall work programme and schedule is summarized in Fig. 71. It covers the period up to mid 2005, the time at which LHC collisions are anticipated. The schedule is planned to ensure that the RICH detectors are fully commissioned and operating together with other LHCb sub-detectors by this time.

A critical task is the production of the HPD photon detectors. The manufacturer (DEP) has proposed a production rate of 20 HPDs per month. Before this production can commence the anode assembly, including the pixel readout chip must be available for encapsulation in the HPD. In the event of a delay in the readout development DEP could increase the production rate to 30 tubes per month, but this contingency would require an additional fabrication plant with consequent increase of 3% on the HPD price. The schedule for the backup MAPMT technology, given in Appendix A, also ensures that the RICH detectors will be ready by mid-2005. This is possible due to the fact that the readout electronics is external to the tube, so its production and testing can be carried out in parallel with tube manufacture.

6.1.1 Completion of R&D

Several of the tasks included in the schedule will involve further R&D before production.

1. The pixel chip: the current ALICE-LHCb iteration of this chip will be delivered in September 2000. Following testing it will be bump-bonded to the silicon sensor then encapsulated and tested in an HPD. Design of the final chip will continue during 2000 and testing will be completed in 2001.

2. Readout electronics: Prototypes of the Level-0 adaptor board, the optical links and the Level-1 readout board will be produced during 2000 to verify the complete binary readout chain.

3. Engineering design: the design of the RICH vessels, support structure, mirrors and their adjustable mounting system will be reviewed and, in the case of the optical components, undergo further testing before finalizing detailed drawings by end 2001.

4. Aerogel: large tiles with high clarity will enhance the low-energy particle identification performance. An ongoing R&D programme testing high clarity samples produced at Novosibirsk will continue during three further years.

5. Alignment, monitoring and control: different options are proposed to fulfil the various tasks in this category, and prototyping and testing will continue before the final technique is chosen before end 2001.

6.1.2 Construction

The major construction tasks include:

1. RICH vessels, superstructure, optics and photon detector mounting: require a production time of approximately one year, and will be completed during 2003. The production time of the largest component, the RICH 2 vessel and support, has been estimated at 10 months by a commercial engineering company.

2. Photodetectors: the rate of production proposed by DEP is 20/month, thus two years are needed. Years 2002 and 2003 are foreseen in the schedule.

3. Readout electronics: the pixel chip production is scheduled during 2001, in time for encapsulation in the production HPDs. Production of the readout electronics chain (from HPD pin-out to DAQ) is scheduled to be completed by end 2003. The only LHCb-specific electronics components are the radiation-hard chips required for the Level-0 interface board. These involve common LHC

developments (TTC chipset, voltage stabilizers) and an adaptation of the optical link multiplex and driver chips, designed for use by the ALICE collaboration. The Level-1 electronics make maximum use of FPGAs to implement specific functionality. The modules are situated in the counting room and so are not exposed to a high radiation dose.

4. Gas systems: similar circulation and recovery systems are foreseen for the RICH 1 and RICH 2 gas radiators. These have been designed by the LHC gas group and will be ready when required for commissioning detectors in 2004.

5. Testing: systematic tests and certification of the photodetectors and readout electronics will be a time-consuming task and must follow the production process. An extensive series of measurements of the photocathode response and the electron optics will require about two days per HPD tube, so two test facilities will be installed in the collaborating institutes to complete the task within two years.

   It is planned to test the RICH 1 detector, equipped with one quadrant of mirrors, photodetectors and readout, in a charged particle beam during the second half of 2003.

6.2 Installation and commissioning

The LHCb spectrometer magnet will be installed and its field measurements completed at latest by end 2003. RICH 1 installation can begin from early 2004. Due to the restricted space in the LHC tunnel, RICH 1 will need to be partially assembled *in situ*. RICH 2 will be assembled in a clean surface laboratory, then lowered into the cavern, and installed mid 2004. Both RICH 1 and RICH 2 detectors will undergo commissioning during the second half of 2004. By early 2005, commissioning with other LHCb sub-detectors, using common DAQ will begin. Six months of operation in this mode are foreseen to ensure the RICH detectors will be ready to take data at nominal LHCb luminosity by mid 2005.

Table 17: RICH project Milestones. * See Section 6.3

Date	Milestone	
	Mechanics and Optics	
2002/Qtr 1	Mechanical designs completed	
2003/Qtr 4	Mechanics and Optics completed	
2004/Qtr 1	Begin Assembly RICH 1 in IP8	
2004/Qtr 3	Begin Installation RICH 2 in IP8	
	Photodetectors	
2000/Qtr 4	Prototpye HPD completed	*
2001/Qtr 3	Place HPD order	*
2004/Qtr 1	Production/testing completed	
	Readout electronics	
2002/Qtr 2	Prototype chain tests completed	
2004/Qtr 1	Production/testing completed	
	RICH Detectors	
2005/Qtr 2	Commissioning completed	

6.3 Milestones

Key milestones for the RICH project are listed in Table 17.

The photodetector milestone at the end of 2000 requires further comment. At the time when this milestone was established the schedule for delivery of the pixel readout chip was anticipated by early 2000. Finalising and checking the design, prior to submission, and the chip production schedule have taken longer than expected, with the result that the pixel chip will not be delivered and tested before mid October. In addition, the bump-bonding contractor, with whom the CERN pixel detector group had a long-established relationship, has withdrawn its services and trials with new contractors have to be established. It now appears unlikely that the end 2000 milestone of demonstrating an HPD with the encapsulated pixel chip can be met. A delay of 4-6 months is estimated before the technical criteria could be achieved. By making use of the contingency, offered by the accelerated DEP HPD production, it would still be possible to meet the 2004 milestone for completion of HPD production

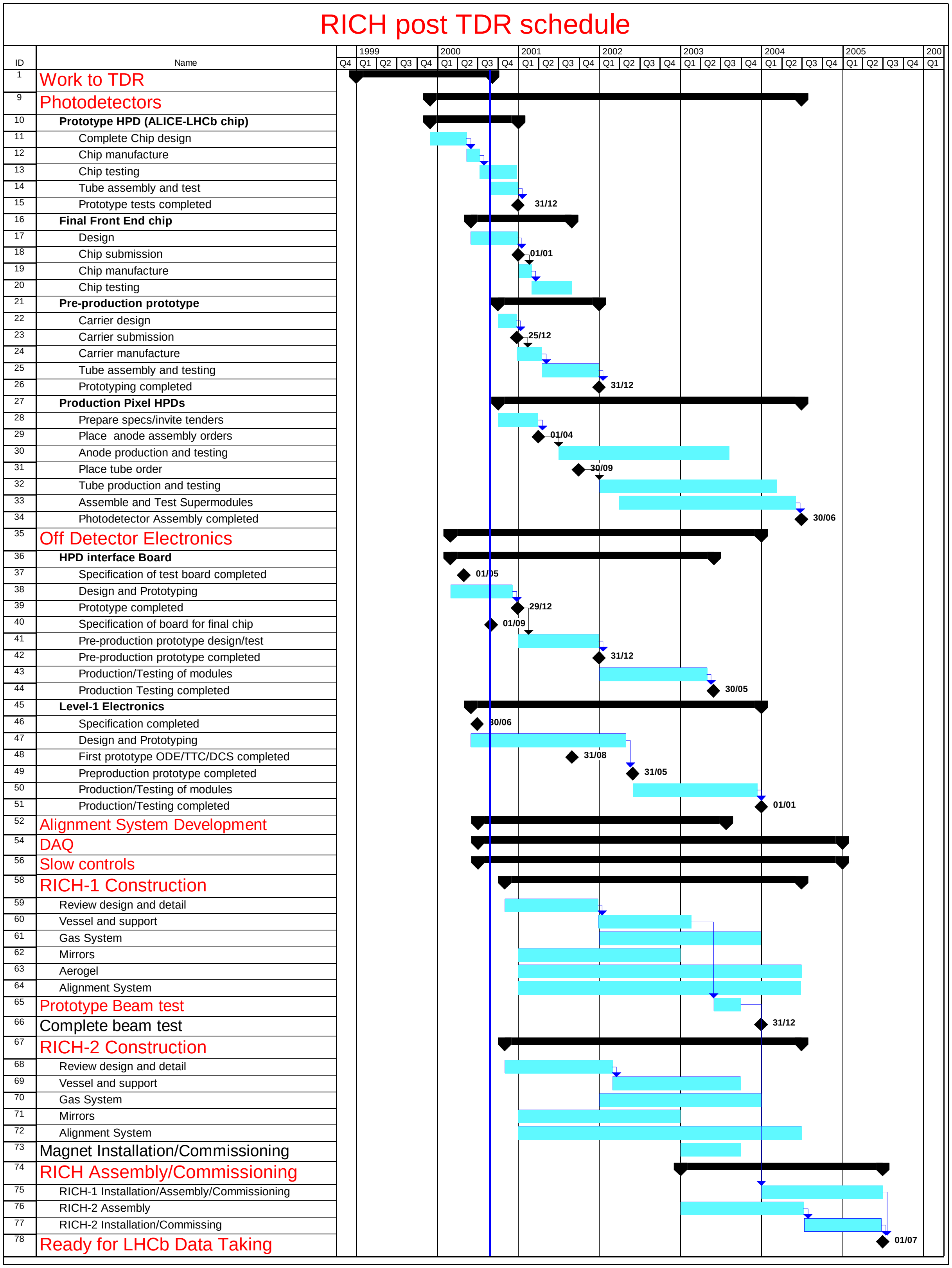

ID	Name	
1	Work to TDR	
9	Photodetectors	
10	**Prototype HPD (ALICE-LHCb chip)**	
11	Complete Chip design	
12	Chip manufacture	
13	Chip testing	
14	Tube assembly and test	
15	Prototype tests completed	31/12
16	**Final Front End chip**	
17	Design	
18	Chip submission	01/01
19	Chip manufacture	
20	Chip testing	
21	**Pre-production prototype**	
22	Carrier design	
23	Carrier submission	25/12
24	Carrier manufacture	
25	Tube assembly and testing	
26	Prototyping completed	31/12
27	**Production Pixel HPDs**	
28	Prepare specs/invite tenders	
29	Place anode assembly orders	01/04
30	Anode production and testing	
31	Place tube order	30/09
32	Tube production and testing	
33	Assemble and Test Supermodules	
34	Photodetector Assembly completed	30/06
35	Off Detector Electronics	
36	**HPD interface Board**	
37	Specification of test board completed	01/05
38	Design and Prototyping	
39	Prototype completed	29/12
40	Specification of board for final chip	01/09
41	Pre-production prototype design/test	
42	Pre-production prototype completed	31/12
43	Production/Testing of modules	
44	Production Testing completed	30/05
45	**Level-1 Electronics**	
46	Specification completed	30/06
47	Design and Prototyping	
48	First prototype ODE/TTC/DCS completed	31/08
49	Preproduction prototype completed	31/05
50	Production/Testing of modules	
51	Production/Testing completed	01/01
52	Alignment System Development	
54	DAQ	
56	Slow controls	
58	RICH-1 Construction	
59	Review design and detail	
60	Vessel and support	
61	Gas System	
62	Mirrors	
63	Aerogel	
64	Alignment System	
65	Prototype Beam test	
66	Complete beam test	31/12
67	RICH-2 Construction	
68	Review design and detail	
69	Vessel and support	
70	Gas System	
71	Mirrors	
72	Alignment System	
73	Magnet Installation/Commissioning	
74	RICH Assembly/Commissioning	
75	RICH-1 Installation/Assembly/Commissioning	
76	RICH-2 Assembly	
77	RICH-2 Installation/Commissing	
78	Ready for LHCb Data Taking	01/07

Figure 71: Schedule of RICH project, up to start of LHCb data taking in mid-2005

and testing. The situation will be reviewed at the end 2000 milestone date, when more information on the status of the pixel chip and on the bump-bonding process will be available. Options to be considered at this time would include pursuing the HPD, with a revised schedule, or changing over to the backup MAPMT technology.

6.4 Costs

The total cost for the RICH detector system is estimated to be 7677 kCHF. Costs are shown in Tables 18 and 19, separately for RICH 1 and RICH 2. Where appropriate, spares have been included. More than 70% of the total cost estimate is based on quotes from industry or recent purchases of similar items (e.g. mirrors and quartz plates by the COMPASS collaboration).

6.5 Division of responsibilities

Institutes currently working on the LHCb RICH project are: CERN, Universities of Bristol, Cambridge, Genova, Glasgow, Edinburgh, Milano, Oxford, Imperial College (London) and the Rutherford Appleton Laboratory.

The sharing of responsibilities for the main RICH project tasks is listed in Table 20. It is not exhaustive, nor exclusive. For example software is clearly a major task, where it is understood that the RICH group is responsible and will have the resources (8 FTE) to provide all RICH specific software, for DAQ, monitoring, reconstruction, pattern recognition, and Level-3 trigger algorithms. The responsibilities for the MAPMT as specified in the Table are limited to maintaining its viability as a backup, until the HPD satisfies the milestones.

Table 18: RICH 1 project costs (kCHF).

Item	Unit	Number of units	sub-total (kCHF)
Mechanics:			629
Vessel superstructure	m^3	5	
Spherical mirror	m^2	3	
Mirror support structure	module	1	
Photodetector support	module	4	
Quartz window	m^2	1.5	
Aerogel	litre	50	
Photodetectors:			1473
Vacuum tube	piece	184	
Ceramic carrier	piece	184	
Silicon sensor	piece	184	
F/E chip	piece	184	
Anode assembly (incl bump bond)	piece	184	
Silicon bias supply	module	28	
HV supply	module	28	
Electronics:			537
Adapter board	board	92	
L0-Trigger/clock links	link	92	
L0-L1 data links	link	368	
L0 reference module	module	2	
L1 boards	board	23	
L1-Trigger/clock links	link	23	
L1-RU data links	link	23	
Readout Units	module	7	
Crates	crate	2	
power supplies/cables	piece	28	
Services:			365
Freezer	module	1	
Compressor	module	1	
Storage tank	module	1	
Tubing, instr/high pressure	system	1	
Tubing, instr/low pressure	system	1	
Programmable controllers	system	1	
Optical alignment system	system	1	
Gas system monitoring	system	1	
Refractive index monitoring	system	1	
RICH 1 TOTAL			**3004**

Table 19: RICH 2 project costs (kCHF).

Item	Unit	Number of units	sub-total (kCHF)
Mechanics:			1204
Vessel superstructure	m^3	100	
Spherical mirror	m^2	9.2	
Plane mirror	m^2	7.6	
Mirror support structure	module	4	
Photodetector support	module	2	
Quartz window	m^2	2	
Magnetic shielding	tonne	22	
Photodetectors:			2290
Vacuum tube	piece	288	
Ceramic carrier	piece	288	
Silicon sensor	piece	288	
F/E chip	piece	288	
Anode assembly (incl bump bond)	piece	288	
Silicon bias supply	module	36	
HV supply	module	35	
Electronics:			814
Adapter board	board	150	
L0-Trigger/clock links	link	150	
L0-L1 data links	link	574	
L0 reference module	module	2	
L1 boards	board	36	
L1-Trigger/clock links	link	36	
L1-RU data links	link	36	
Readout Units	module	11	
Crates	crate	2	
power supplies/cables	piece	36	
Services:			365
Freezer	module	1	
Compressor	module	1	
Storage tank	module	1	
Tubing, instr/high pressure	system	1	
Tubing, instr/low pressure	system	1	
Programmable controllers	system	1	
Optical alignment system	system	1	
Gas system monitoring	system	1	
Refractive index monitoring	system	1	
RICH 2 TOTAL			**4673**

Table 20: RICH project: Sharing of responsibilities

Task	Institutes
Photon detectors:	
Pixel chip design, production	CERN
Pixel chip testing	CERN, Glasgow
HPD production	CERN
Photodetector test facilities	Edinburgh, Glasgow
MAPMT backup (<2001)	Edinburgh, Genova, Oxford
Readout Electronics:	
Design, production	Cambridge, Oxford
Testing	Cambridge, Oxford
DAQ interface	Cambridge, CERN, Oxford
RICH 1 Mechanics:	
Project management	Imperial
Vessel and superstructure	Imperial
Mirror support, engineering and manufacture	Bristol
Mirror procurement, characterization and testing	Bristol, CERN
Photodetector mount	Imperial
RICH 2 Mechanics:	
Project management	CERN
Vessel and superstructure	RAL
Mirror support, engineering and manufacture	CERN
Mirror procurement, characterization and testing	CERN, Milano
Photodetector mount	Genova
Overall magnetic shield	Milano
Radiators:	
Gas systems	CERN
Aerogel	Milano
Experimental Area Infrastructure	CERN
Monitoring, Control, Alignment:	
Design, production	CERN, Edinburgh, Milano, RAL

A Back-up Photodetector

A.1 Multianode photomultiplier

The multianode photomultiplier tube (MAPMT) consists of an array of square anodes each with its own metal dynode chain incorporated into a single vacuum tube. The most dense pixelization available, 8×8 pixels, provides the spatial resolution required for the LHCb RICH detector. Figure 72 shows a schematic of the MAPMT. The dynode structure is separated into 64 square pixels of 2.0×2.0 mm^2 area, separated by 0.3 mm gaps.

The 64-pixel MAPMTs are commercially available and have been tested by LHCb in 1998 [22]. Since then the manufacturer, Hamamatsu, has provided some modifications which better match our specifications. The MAPMT R7600-03-M64[20] has a 0.8 mm thick UV-glass window with a semi-transparent photocathode deposited on the inside. Light transmission through the UV-glass window extends down to a wavelength of 200 nm. The photons are converted into photoelectrons in a Bialkali photocathode. The quantum efficiency of the MAPMT, measured by Hamamatsu, has a maximum of 22% at 380 nm. For each pixel the photoelectrons are focused onto a 12-stage dynode chain and multiplied through secondary emission. The mean gain of the MAPMT is about 3×10^5 when operated at a voltage of 800 V.

The geometrical coverage of the MAPMT, i.e. the ratio of the sensitive photocathode area to the total tube area including the outer casing is only $\sim 48\%$. This fraction can be increased by placing a single lens with one refracting and one flat surface in front of each MAPMT [75], as shown in Fig. 73. In the thin lens approximation a single refracting surface with radius-of-curvature R has a focal length

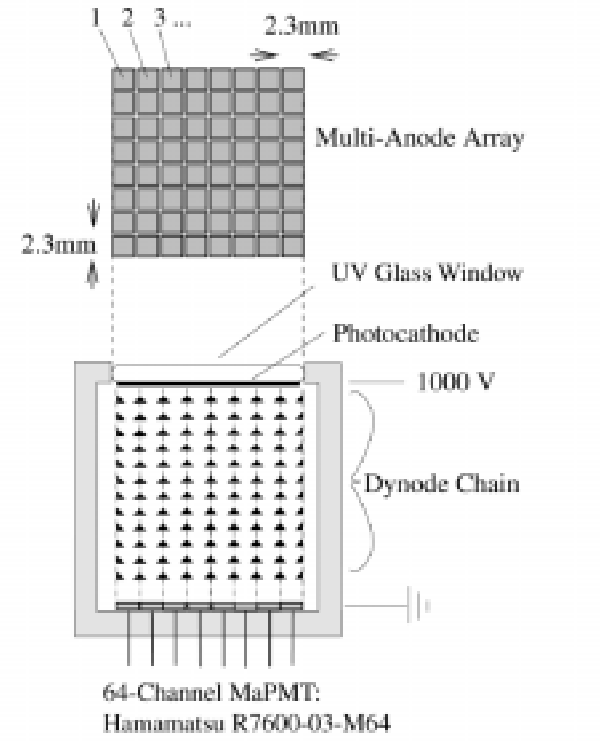

Figure 72:
Sketch of a multianode photomultiplier tube.

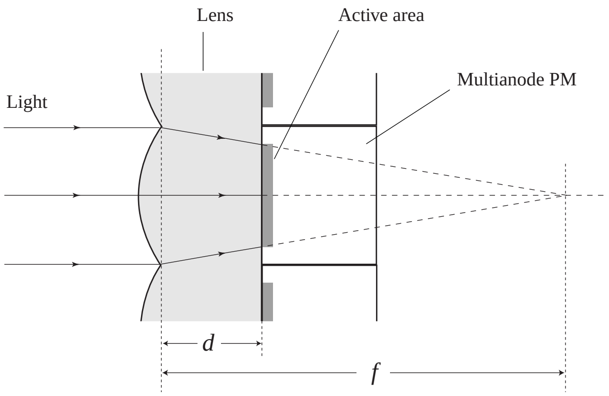

Figure 73:
Schematic view of lens system, in front of the close-packed photomultipliers (side view). The focusing of normally incident light is illustrated. The full aperture of the lens is focused onto the sensitive area of the MAPMT.

---

[20] With respect to its predecessor, the R5900-00-M64, the borosilicate window is replaced by a UV-glass window which increases the integrated quantum efficiency by 50%. In addition, a flange of 1 mm size around the MAPMT is removed, thereby improving the packing fraction by 14%.

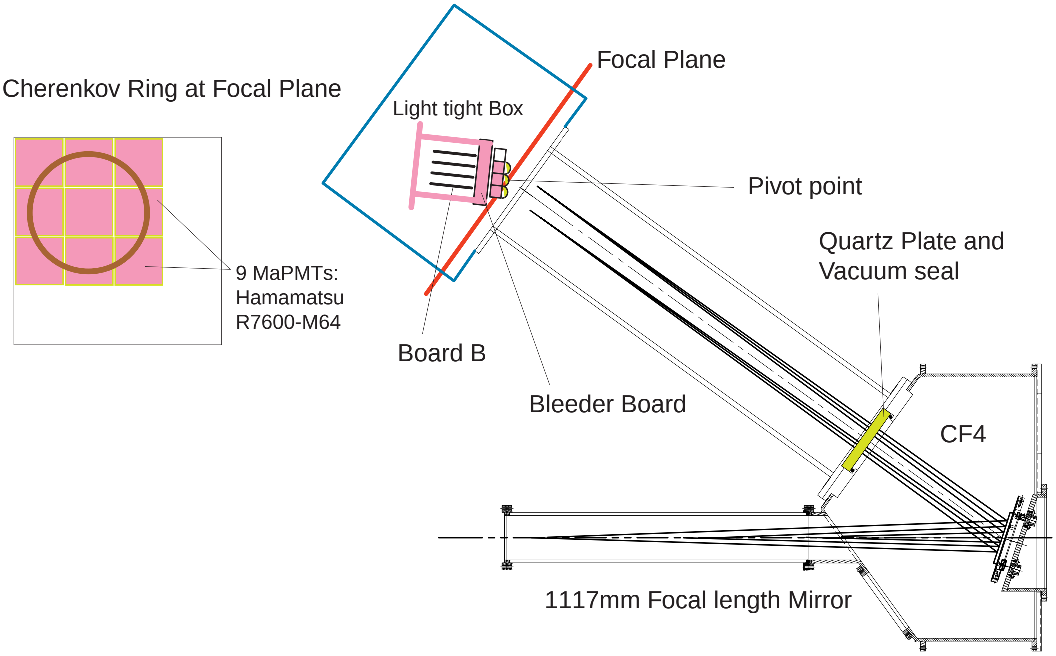

Figure 74: A schematic of the beam test setup.

$f = R/(1 - 1/n)$ where n is the refractive index of the lens material. If the distance d of the refracting surface to the photocathode is chosen to be equal to R the demagnification factor is $(f - d)/f \approx 2/3$. Over the full aperture of the lens, light at normal incidence with respect to the photodetector plane is focused onto the photocathode, thus restoring full geometrical acceptance.

A.2 Tests of the MAPMT

The results of the extensive R&D programme carried out for the MAPMT over the last two years are summarized here. More details can be found in references [76, 22].

A.2.1 Cluster test with lenses

Single MAPMTs and an array of 3 × 3 MAPMTs have been tested in the full-scale RICH 1 prototype, shown in Fig. 74, in a beam at the CERN SPS facility. The cathode voltage was set at -1000 V. Quartz lenses with a radius of curvature of 25 mm and maximum height 24 mm were mounted onto the front face of each MAPMT to focus the Cherenkov light onto the sensitive area of the tubes. The vessel was filled with gaseous CF_4 at a pressure of 700 mbar, giving an expected Cherenkov angle of 26 mrad for highly relativistic particles. Measurements were taken with a 120 GeV/c π^- beam at intensities of typically a few 10^4 particles per spill of the CERN SPS cycle.

The main aim of the tests was to demonstrate that the MAPMT is a viable photo–detector for the LHCb RICH system. These tests fall into three main areas:

1. Demonstration of the performance of the MAPMTs, both individually and in an array, with and without lenses;
2. Operation with pipelined read–out electronics, compatible with the LHC 25 ns bunch crossing interval and partially satisfying the requirements of the LHCb trigger and read–out architecture;
3. Testing the functionality of the tubes in a real detector environment, i.e. the effect of charged particles traversing the tubes and the lenses, and the impact of magnetic fields on the performance of the tubes (with and without shielding).

Further tests of tubes and the electronic read–out were performed using LED scanning facilities. The MAPMTs were protected from extraneous light by a dark box housing. The light source used was a blue 470 nm LED with a maximum luminosity of 1000 mcd and a view angle of 15°. The pulsing of the LED was performed using a FET circuit which provided a switching rate of 10 kHz with a pulse duration of approximately 10 ns. The LED was mounted externally and coupled into the dark box using a monomode fibre giving a spot size of 50 μm. The MAPMT and the fibre tip were both mounted on a motorised stage. The stages could be positioned with a resolution better than 5 μm which allowed precise scans over the MAPMT acceptance. A stepper motor driver, interfaced to a PC, was used to control the stages.

A.2.2 Fast readout

The tests involving individual MAPMTs were performed using a read-out chain of CAMAC amplifiers and ADCs [22]. The pipelined electronic read-out system is shown schematically in Fig. 75. The nine MAPMTs were mounted onto a bleeder board, which provided the mechanical support and dynode chain resistor network for up to 16 MAPMTs in a 4 × 4 array. The board also adapted the MAPMT anode feedthrough pitch of the 1024 data channels to the Pin Grid Array (PGA) pitch of the kapton cables which then coupled the output signal channels to the front-end boards. Each front-end board multiplexed the analogue signals from one or two MAPMTs and was the carrier for the front-end ASIC (Amplification-Specific Integrated Circuit), the APVm [78].

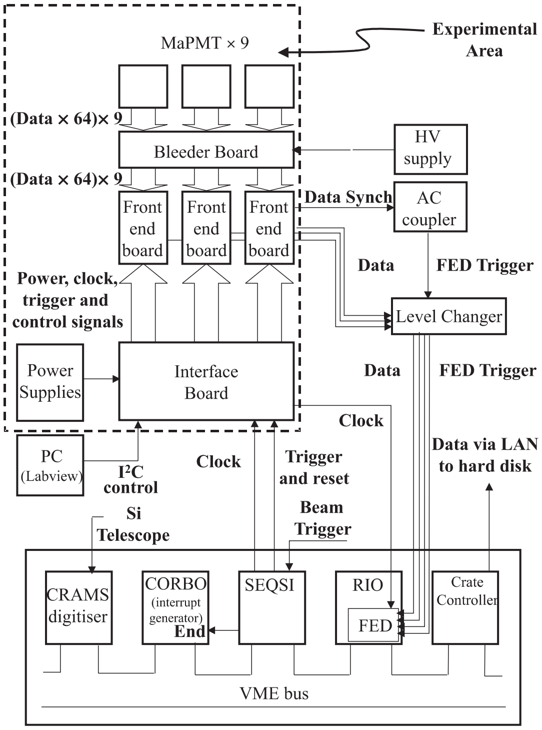

Figure 75: A block diagram of the electronic read-out and data acquisition systems. The components within the dashed box were in the experimental area.

The APVm shaped, amplified, buffered and multiplexed the input signals. The front-end boards included an AC-coupler fan-in made from a ceramic base. The large signals from the MAPMT have to be attenuated by about a factor of ten to be within the dynamic range of the APVm. The front-end boards were then coupled to a single interface board, which fanned-out the power, the trigger signals, the clock and the Philips I^2C control signals [79] for the APVm. The analogue pipeline signals from the APVm and the accompanying output data synch were routed directly to the Front-End Digitiser (FED) and the rest of data acquisition system. The control of the front-end ASIC was performed using the outputs of the SEQSI programmable front-end control module [80]. The six APVm ASICs each produced an analogue data output which was digitised using the Front-End Digitiser (FED). The FED is a PCI Mezzanine Card (PMC) which was fixed to a VME based mother-board and processor unit[21]. The FED PMC was a prototype module for the read-out of the CMS inner tracker [56]. The front-panel of the CMS FED PMC has 8 analogue input data channels, a trigger and a clock input. The data from the front-end boards were both level shifted and amplified, to fall within the dynamic range of the Flash ADCs (FADCs) on the FED PMC,

---

[21] CES RIO, model No. 8061.

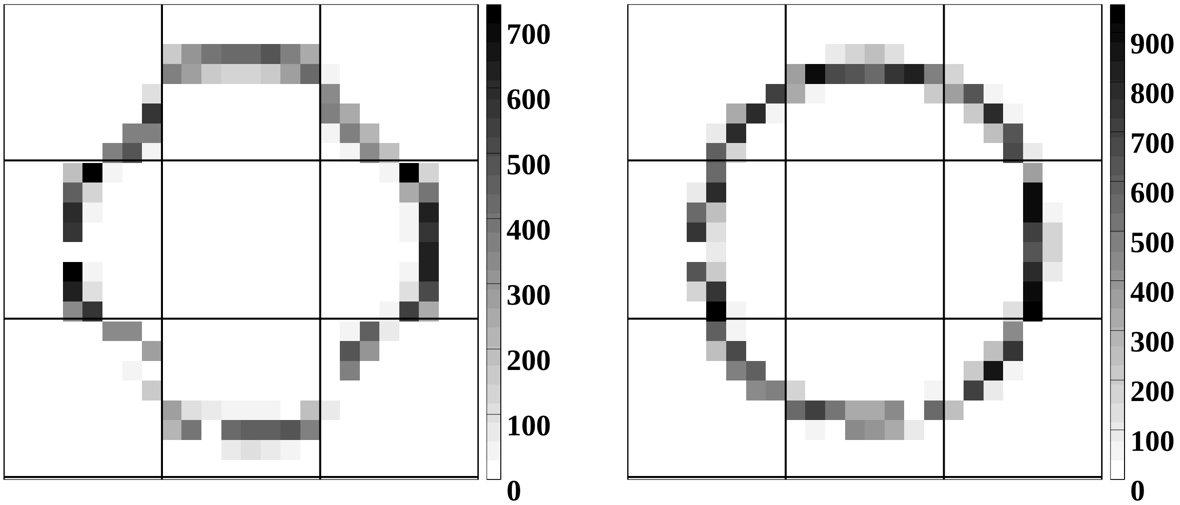

Figure 76: Cherenkov ring from a CF_4 gas radiator at a pressure of 700 mbar, using MAPMTs with (right-hand plot) and without (left-hand plot) quartz lenses mounted in front of the tubes. The common-mode noise has been subtracted, and cross-talk due to the electronics chain has been corrected for.

by a separate level-changing board.

A.2.3 Detection efficiency

The data taken with the array of 3 × 3 MAPMTs and the pipelined read-out electronics have been analysed as follows. A common-mode baseline variation in all pixels of a front-end board has been subtracted on an event-by-event basis. With the pipelined read-out electronics cross-talk was observed. Using LED runs this cross-talk has been investigated and several sources were identified. Within the APVm chip neighbouring sample channels have an asymmetric cross-talk. Pixel x induces a signal in pixel y but not vice-versa. This cross-talk is large (pulse-height ratio $r \sim 0.33$). It is present only in some channels, with repetitive patterns, and its occurence varies for the different front-end boards. A symmetric cross-talk was also observed ($r \sim 0.15$) in neighbouring channels at the APVm input which is attributed to the ceramic fan-in. No cross-talk has been observed when a tube is read out with the CAMAC based electronics thus confirming that the above effetcs are entirely generated in the electronic read-out.

To count the number of observed photo-electrons n_{pe} the pulse height of a signal is required to exceed the pedestal by 5σ where σ is the standard deviation of the pedestal peak. Cross-talk is removed by rejecting signals in a pixel if there is a larger signal in one of its cross-talk partner pixels. Genuine double hits are lost by this procedure and n_{pe} is corrected for it. The integrated signals of two runs (of 6000 events each) are shown in Fig. 76, one with and one without the lenses in front of the MAPMTs. The Cherenkov ring is clearly visible and the effect of the lenses is nicely demonstrated. The gain in n_{pe} by employing the lenses is 45%. The background is small and is estimated from the pixels away from the Cherenkov ring. A few dead pixels are visible. These are due to the electronics and do not occur when using CAMAC electronics. The number of observed signals is also corrected for multiple photo-electrons arriving in one pixel. The loss of the signal below the 5σ threshold cut is not corrected for. It is estimated by fitting the pulse height spectra to be about 9%.

The results for the photon counting are given in Table 21 and compared with a full Monte Carlo simulation. Checks have been

	With lens	Without lens
Total	6.78	4.69
background	0.26	0.21
n_{pe}	6.51	4.49
Simulation	6.21	3.94

Table 21: Photon counting.

made by changing the cross-talk subtraction method, and comparing different runs under the same conditions. The systematic error on n_{pe} is estimated to be about 5% of its value. The statistical error is negligible. By calculating n_{pe} for the individual tubes, the quantum efficiency is found to vary by about ±10% for the different tubes. The results from the single tube measurements with the CAMAC read-out are in agreement with these results. The Cherenkov angle resolution is in agreement with the expectations.

A pulse height spectrum for the MAPMT is shown in Fig. 77, measured with a light scanning facility. The pedestal peak and the broad signal containing mostly one photo-electron are clearly visible. Comparing the width of the single photon peak with its mean value yields a lower limit of 3.7 for the gain at the first dynode. This corresponds to a probability of 2.5% or less for no multiplication occurring at the first dynode. The signal to pedestal width ratio is 40:1. The loss of signal efficiency due to the requirement that the signals have to exceed a level 5 σ above the pedestal value has also been studied and is in agreement with the value measured with the pipelined read-out.

The gain variations for the 64 different dynode chains within a tube are about a factor of two with an RMS spread of about 30% about the mean value. A degradation of the gain is visible for the edge columns. This has been investigated in detail by scanning across the tubes in steps of 0.1 mm. The collection efficiency of the tube deteriorates towards the geometric edge of these pixels and the overall efficiency of the MAPMT is reduced by a few percent. The pixel size as defined by the 50% efficiency points of a pixel is 2.1 mm which is a little larger than the 2.0 mm opening of the dynodes reported from the manufacturer.

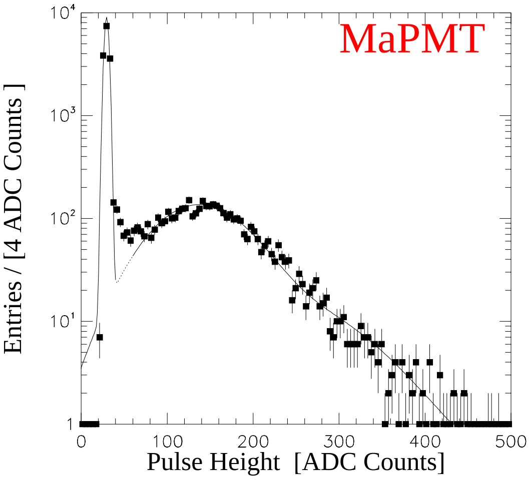

Figure 77:
Single photon spectrum of an MAPMT pixel.

A.2.4 Traversing particles

A few million events have been recorded using the CAMAC read-out where charged particles were traversing one MAPMT. Data were taken with and without a quartz lens in front of the tube and for different angles of the particle direction with respect to the axis normal to the photo cathode. For small incoming particle angles the Cherenkov photons emitted in the lens and in the photo cathode produce hits in only about 7 to 9 pixels. Most photons produced in the lens undergo total internal reflection. Only for angles around 45 degrees a charged particle produces signals in about 20 to 30 pixels. These results are in agreement with a simulation. Charged particles traversing the MAPMT are thus a small and manageable background.

A.2.5 Magnetic field tests

The sensitivity of the MAPMT to magnetic fields has been studied by placing a single tube into a Helmholtz coil which can provide axial magnetic fields of up to 3 mT. Using a

LED light source, the efficiency of the tubes has been measured for magnetic fields transverse and parallel to the photodetector axis. The MAPMT is measured to be insensitive to transverse magnetic fields up to 3 mT. For longitudinal fields larger than 1 mT, however, the efficiency of the MAPMT deteriorates. This loss occurs mostly in the two edge rows and at 3 mT the collection efficiency is reduced to 50 % with respect to no field. A square Mu-metal tube of wall thickness 0.9 mm effectively reduces this efficiency loss. Measurements have been made with a shielding tube extending along the z-axis beyond the entrance window of the tube by 13 mm and 32 mm, respectively. At 32 mm extension the efficiency is not affected by the magnetic field any more. An estimate of the field strength required to saturate this Mu-metal is around 30 mT. The MAPMT can thus be effectively shielded with a Mu-metal structure.

A.3 Implementation in RICH

A short summary of the implementation is given here for the MAPMT back-up solution, concentrating on the differences to the HPD design. For a detailed description see [6].

The basic unit, called a module, consists of an array of 4 × 4 MAPMTs and is shown in Fig. 78. The 16 tubes are mounted onto a mother-board which distributes the high voltage to the photocathode and the dynodes of each tube and connects the 1024 anode channels of a unit to the front-end electronics (hybrid) which are mounted on the back of the mother-board. The modules will be mounted onto a square metal or carbon-fibre support structure. The single quartz lenses in front of each tube and the grid of Mu-metal sheets will be made an integral part of the structure. The MAPMTs must point towards the incident light. Thus the support structure will be tilted and offset accordingly, and enclosed in an aluminium frame. The outermost modules only have to be partially equipped with tubes to cover the sensitive area. Table 22 summarizes the main geometrical parameters.

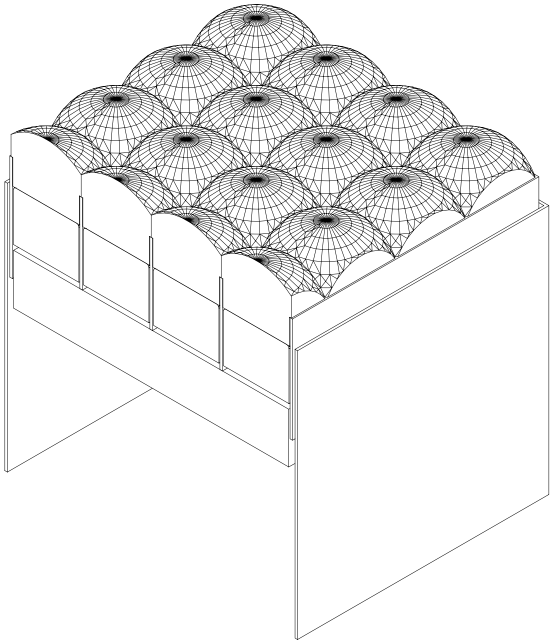

Figure 78: A 4 × 4 MAPMT module.

The front-end electronics of the MAPMT is located on the back of the mother-board (Level-0 interface board). This board also provides the mechanical support for the tubes and distributes the high voltages to the dynode chains of each tube. It feeds the 1024 signals lines from the 16 tubes mounted on the front to the back and connects these with wire bonds to the hybrids which contain the front-end chips. The F/E electronics of the MAPMT is analogue and based on the SCTA 128, or the BEETLE chip if it becomes available. Eight front-end chips will read out the all tubes of one module.

The gain of the MAPMT is 3×10^5 which has to be attenuated to match the dynamic range of the SCTA 128 or the BEETLE chip. An attenuation of about a factor of ten is necessary. Three solutions are pursued: an attenuator network integrated into the hybrid; a modification of the preamplifier stage of the F/E chip; or operating the MAPMT at lower gain [77]. An average single photo-electron signal over pedestal width of 40:1 can be achieved exploiting the low noise of the front-end chip. One difference to the HPD option is the lo-

MAPMT Modules:		
Module size [mm^2]	109 × 109	
Active/total area	0.79	
Quadrants/Halfplane:	RICH 1	RICH 2
Horizontal tilt [mrad]	± 440	± 240
Vertical tilt [mrad]	± 125	0
Modules per row	5	6
Modules per column	5	11
Totals:	RICH 1	RICH 2
Modules	100	132
Tubes	1480	2024
RICH totals:		
Modules	232	
Tubes	3504	
Channels	224256	

Table 22: MAPMT Geometry.

cation of the off-detector electronics (ODE). For analogue signals, copper links will be used between Level-0 F/E and Level-1 ODE. This limits the distance between these to a length of 12 m. The Level-1 electronics will require receivers and ADCs for the front-end and will need to be designed to tolerate problems due to radiation, particularly single event upsets. Access will be severely restricted.

A binary readout scheme for the MAPMT will also be studied. This has several potential benefits, including:

1. The use of fibre-optic links and the radiation-hard fibre driver technology for data transfer between Level-0 and Level-1, as proposed for the HPDs.
2. Level-1 electronics in the counting room facilitates access and commissioning.
3. Re-use of the expertise and designs developed for the HPD.
4. Simplified grounding.

In Table 24 a schedule for the MAPMT back-up project is presented. The front-end chip and the mother-board/hybrid are now the most time-critical parts of the project. A few working mother-boards and hybrids plus front-end chips are needed before the testing of large quantities of MAPMTs can start. Of these the mother-board/hybrid is the most serious as there is little possibility of saving time. The schedule of the front-end chip would be shortened if the MAPMT could be operated at lower gain without the need of a redesign or attenuator network (see Reference [77]). The test of a RICH 1 half-plane in the 2003 test beams at CERN is also critical since the production and testing of the final modules would not start before 1/2003. The ODE schedule would greatly benefit with the binary readout option (for reasons listed above).

Level-0 & Front-end chip	
Modules / chips	232 / 1856
Channels per module	1024
Readout channels	237568
Multiplexing	32-fold
Data links to Level-1	7424
Level 1	
Bandwidth (3% occupancy, without/with zero suppr.)	85 / 7.7 Gbits/s
VME modules	78
Multiplexers	5

Table 23: MAPMT Electronics.

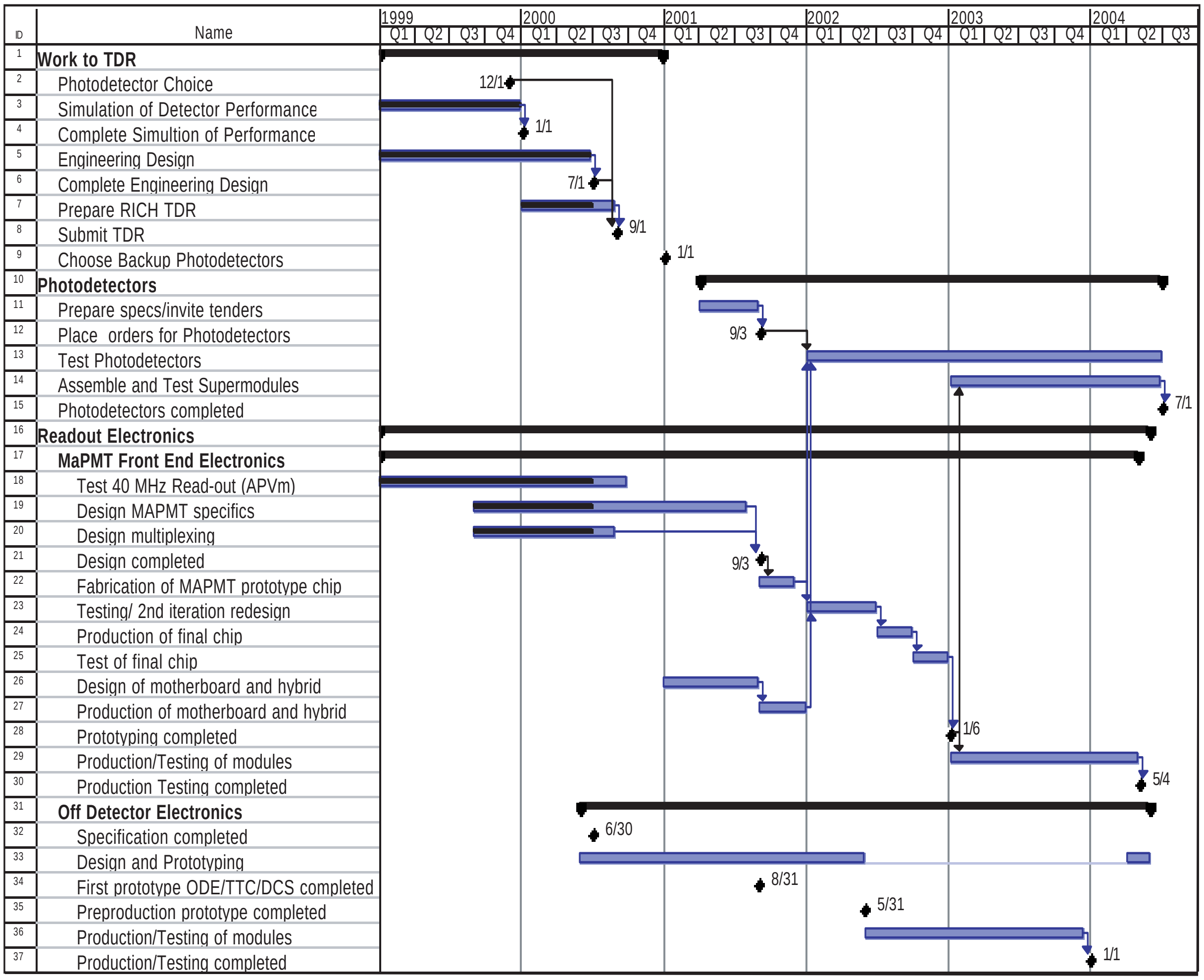

Table 24: Project schedule for the MAPMT if it were to become the base-line photodetector, up to July 2004 when assembly of the RICH detectors will start at CERN.

References

[1] LHCb Technical Proposal, CERN/LHCC 98-4.

[2] LHCb Magnet Technical Design Report, CERN/LHCC 2000-7.

[3] LHCb Calorimeters Technical Design Report, CERN/LHCC 2000-36.

[4] C.Joram *et al.*, "Proposal to use the Pad HPD as Photodetector of the LHCb RICH", LHCb 2000–63 RICH.

[5] T.Gys *et al.*, "The use of Pixel Hybrid Photon Detectors in the RICH counters of LHCb", LHCb 2000–64 RICH.

[6] F.Muheim *et al.*, "Proposal for Multi-Anode Photomultiplier tubes as Photodetectors for the LHCb RICH", LHCb 2000–65 RICH.

[7] T.Ypsilantis and J.Seguinot, Nucl. Instr. Meth. **A 343** (1994) 30.

[8] J.Christiansen, "Requirements for the L0 front-end electronics", LHCb 99–29.

[9] K.Wyllie, "Level 0 electronics for the LHCb RICH" LHCb 2000-75 RICH.

[10] G.Wilkinson *et al.*, "A simulation study of the LHCb RICH performance", LHCb 2000–66 RICH.

[11] T.Sjöstrand and M.Bengtsson, Comp. Phys. Comm. **43** (1987) 367.

[12] P.Bartalini *et al.*, "Tuning of multiple interactions generated by PYTHIA", LHCb 99–28.

[13] R.Forty and O.Schneider, "RICH pattern recognition", LHCb 98–40.

[14] M.Benayoun, "Search for trackless rings", presentation at LHCb RICH meeting, 30 November, 1999.

[15] A.Schöning, "Particle identification in the RICH detectors and study of impact parameters", LHCb 97–18.

[16] M.Tobar, "B flavour tagging with kaons", LHCb 98–18.

[17] GAUDI User Guide, http://lhcb.cern.ch/computing/Components/Gaudi_v5/gug.pdf

[18] I.Jacobson, G.Booch and G.Rumbaugh, "The Unified Software Development Process", Addison-Wesley, Reading MA, 1999.

[19] E.Gamma, R.Helm, R.Johnson and J.Vlissides, "Design Patterns", Addison-Wesley, Reading MA, 1995.

[20] D.Liko and N.Neufeld, "Design of the Object-Oriented RICH reconstruction", LHCb 2000–67.

[21] E.Albrecht *et al.*, Nucl. Instr. and Meth. **A 411** (1998) 249.

[22] E.Albrecht et. al., "A prototype RICH detector Using Multi-Anode Photo Multiplier Tubes and Hybrid Photo-Diodes", LHCb 2000–68 RICH, submitted to Nucl. Instr. and Meth. A.

[23] O.Toker *et al.*, Nucl. Instr. and Meth. **A 340** (1994) 572.

[24] E.Chesi *et al.*, "The 5-inch 2048-pad HPD development project", LHCb 98–37.

[25] T.Bellunato *et al.*, "Optical characterization of aerogel as Cherenkov radiator", LHCb 2000–73.

[26] T.Bellunato *et al.*, "Beam tests with aerogel RICH radiator", LHCb 2000–76.

[27] I.P.Csorba, "Image Tubes", Howard W. Sams & Co., 1985.

[28] T.Gys and D.Piedigrossi, "Performance of electrostatically-focused Image Intensifier Tubes in Low Magnetic Fields", LHCb 97–26.

[29] E.Heijne *et al.*, Nucl. Instr. and Meth. **A 383** (1996) 55.

[30] M.Alemi *et al.* “First operation of a hybrid photon detector prototype with electrostatic cross-focussing and integrated silicon pixel readout”, Nucl. Instr. and Meth. **A 449** (2000) 48.

[31] C.Iselin, “Solution of Poisson’s or Laplace’s equation in two-dimentional regions”, CERN Program Library long write-up T604, 1984.

[32] T.Seidel, “Calculation of Photoelectron Paths in Cylindrical Coordinates”, CERN EF/IN internal report, 1990, Program upgraded by T.Gys.

[33] M.Alemi em et al., IEEE Trans. Nucl. Sc. vol 46 no.6, (1999), 1901.

[34] E.Albrecht,*et al.*, Nucl. Instr. and Meth. **A 442** (2000) 164.

[35] S.Easo, *et al.*, “Tests of full-scale Pixel HPD prototype”. LHCb 2000–70.

[36] M.Alemi *et al.*, Nucl. Phys. **B** (Proc Suppl.) **78** (1999) 360.

[37] ALICE- Technical Proposal for A Large ION Collider Experiment at the CERN LHC, CERN/LHCC 95-71, December 1995.

[38] T.Gys and D.Piedigrossi, “Performance of full-scale pixel HPD tubes in low magnetic fields”, LHCb 2000–69 RICH.

[39] Technical Design Report for the Inner Tracking System(ITS), CERN/LHCC 99-12, June 1999.

[40] K.Wyllie et.al, “A pixel readout chip for tracking at ALICE and particle identification at LHCb”,Proceedings of the fifth workshop on Electronics for LHC Experiments, Snowmass, Colorado, September 1999, CERN/LHCC/99–33.

[41] M.Campbell et. al, IEEE Trans. Nucl. Sc. vol 45 no. 3 (1998) 751.

[42] W.Snoeys et.al. Nucl. Instr. and Meth. **A 439** (2000) 349.

[43] M.Campbell et. al, IEEE Trancs. Nucl. Sc. vol 46 no. 3 (1999)156.

[44] C.D’Ambrosio, L.Fernandez, M.Laub, D.Piedigrossi, “The optical systems of LHCb RICHes: a study on the mirror walls and mirror specifications”, LHCb 2000–71.

[45] C.D’Ambrosio, M.Laub, D.Piedigrossi, P.Wertelaers, P.Wicht, “An experimental set-up to measure the long-term stability of large-mirror supports”, LHCb 2000–20.

[46] C.D’Ambrosio, M.Laub, D.Piedigrossi, P.Wertelaers, P.Wicht, “Characterization of mirror mount prototypes for RICH detectors”, LHCb 2000–72.

[47] J.Christiansen, *et al.*, “TTCrx Reference Manual”, RD12 project. http://www.cern.ch/TTC/TTCrx_manual3.0.pdf

[48] “JTAG: IEEE Standard Test Access Port and Boundary Scan Architecture”, IEEE Std. 1149.1 (1990).

[49] “The LHCb Experimental Controls System”, http://lhcb.cern.ch/computing/controls/default.htm.

[50] J.Bibby, S.Wotton, “RICH Electronics: Requirements, Specifications and Implementation”, LHCb 2000–74 RICH.

[51] A.Kluge, “Status of PILOT Electronics”, Presentation at ALICE SPD meeting, May 15, 2000.

[52] P.Denes, “Digitisation and Data Transmission for the CMS ECAL”, Proceedings of the Fourth Workshop on Electronics for LHC Experiments, Rome, Italy, October 1998, CERN/LHCC/98–36.

[53] P.Moriera, *et al.*, “A 1.25 Gbit/s Serializer for LHC Data and Trigger Optical Links”, Proceedings of the Fifth Workshop on Electronics for LHC Experiments,

Snowmass, Colorado, September 1999, CERN/LHCC/99–33.

[54] H.Muller, "LHCb Readout Units", http://hmuller.home.cern.ch/hmuller/readout_unit.htm.

[55] O.Boyle *et al.*, "The S-LINK Interface Specification", http://www.cern.ch/HSI/s-link/spec, March 1997.

[56] J.Coughlan, "CMS Front-End Driver PMC", User Manual, Rutherford Appleton Laboratory, Unpublished.

[57] G.Barber, *et al.*, "The mechanical design of RICH-1" , LHCb 2000–77 RICH.

[58] G.Barber, A.Duane, J.Lidbury, "The installation of RICH 1 and the Beampipe". LHCb 2000–78 RICH.

[59] M.Bosteels, F.Hahn, S.Haider, R.Lindner, O.Ullaland, "LHCb RICH Gas system proposal" LHCb 2000–79 RICH.

[60] C.D'Ambrosio, *et al.*, "Monitoring, Alignment and Control of the RICH Detectors", LHCb 2000–80 RICH.

[61] O.Ullaland, *et al.*, "LHCb RICH 2 Mechanics" LHCb 2000–81 RICH.

[62] M.Alemi, "Passive magnetic shielding calculation for the photodetectors of RICH2", LHCb 98–17 RICH.

M.Alemi, Tecniche di rivelazione nei RICH di LHCb, PhD thesis, Milano 1999.

[63] S.Cuneo, M.Ameri, V.Gracco, P.Musico, A.Petrolini, M.Sannino, "A proposal for a supporting structure for the Hybrid Pixel Detector (HPD) of RICH 2". LHCb 2000–82 RICH.

[64] H.Kroha, Nucl. Phys. **B** (Proc. Suppl.) **54** (1997) 80.

[65] W.Blum et al., Nucl. Instr. and Meth. **A 377** (1996) 404.

[66] W.Blum et al., Nucl. Instr. and Meth. **A 367** (1995) 413.

[67] A.Gorišek et al., Nucl. Instr. and Meth. **A 433** (1999) 408.

[68] F.Filthaut, Presentation at LHCb RICH meeting, 19 March 1999. http://lhcb.cern.ch/rich/postscript/filthaut_190399.ps

[69] M.L.Andrieux et al., Nucl. Instr. and Meth. **A 371** (1996) 259.

[70] E.Fokitis et al., Nucl. Phys. **B** (Proc. Suppl.) **44** (1995) 246.

[71] A.Filippas et al., Nucl. Instr. and Meth. **A 371** (1996) 255.

[72] G.Lenzen et al., Nucl. Instr. and Meth. **A 343** (1994) 268.

[73] G.Barichello et al., Nucl. Instr. and Meth. **A 419** (1998) 1.

[74] C.Gaspar, LHCb Frontend Electronics Workshop, 16-19 May 2000. http://lhcb.cern.ch/computing/online/html/Workshop%20Agenda.htm

[75] R.Forty, "Use of lenses to increase the RICH photodetector coverage", LHCb 98–38.

[76] A.Albrecht, *et al.* "Test of a Multi-Anode PMT cluster equipped with lenses in the detection of Cherenkov rings". LHCb 2000–83 RICH.

[77] S.Eisenhardt, J.Libby, F.Muheim "Study of Multi Anode Photo Multiplier Tubes at Low Gains", LHCb 2000–88 RICH.

[78] L.L.Jones *et al.*, "Electronics for LHC Experiments", Rome 1998, CERN/LHCC/98–36 (1998) 185.

[79] Philips Semiconductors, "The I^{2}C-Bus specification", version 2.1, January 2000.

[80] M.Morrisey, "SEQSI Manual", Rutherford Appleton Laboratory, Unpublished.